Fermi National Accelerator Laboratory

**FERMILAB Pub-95/025-E**
**CDF**

# A Measurement of the Ratio $\sigma \bullet B(p\bar{p} \to W \to e\nu)/\sigma \bullet B(p\bar{p} \to Z^0 \to ee)$ in $p\bar{p}$ Collisions at $\sqrt{s} = 1800$ GeV

F. Abe et al.
The CDF Collaboration

*Fermi National Accelerator Laboratory*
*P.O. Box 500, Batavia, Illinois 60510*

March 1995

Submitted to *Physical Review D*

Operated by Universities Research Association Inc. under Contract No. DE-AC02-76CHO3000 with the United States Department of Energy

CDF/PUB/ELECTROWEAK/PUBLIC/2812
FERMILAB-PUB-95/025-E

# A Measurement of the Ratio $\sigma\cdot B(p\bar{p}\to W\to e\nu)\ /\ \sigma\cdot B(p\bar{p}\to Z^0\to ee)$ in $p\bar{p}$ Collisions at $\sqrt{s} = 1800$ GeV

F. Abe,[13] M. G. Albrow,[7] S.R. Amendolia,[23] D. Amidei,[16] J. Antos,[28] C. Anway-Wiese,[4]
G. Apollinari,[26] H. Areti,[7] M. Atac,[7] P. Auchincloss,[25] F. Azfar,[21] P. Azzi,[20] N. Bacchetta,[18]
W. Badgett,[16] M. W. Bailey,[18] J. Bao,[35] P. de Barbaro,[25] A. Barbaro-Galtieri,[14] V. E. Barnes,[24]
B. A. Barnett,[12] P. Bartalini,[23] G. Bauer,[15] T. Baumann,[9] F. Bedeschi,[23] S. Behrends,[3]
S. Belforte,[23] G. Bellettini,[23] J. Bellinger,[34] D. Benjamin,[33] J. Benlloch,[15] J. Bensinger,[3]
D. Benton,[21] A. Beretvas,[7] J. P. Berge,[7] S. Bertolucci,[8] A. Bhatti,[26] K. Biery,[11] M. Binkley,[7]
F. Bird,[29] D. Bisello,[20] R. E. Blair,[1] C. Blocker,[29] A. Bodek,[25] W. Bokhari,[15] V. Bolognesi,[23]
D. Bortoletto,[24] C. Boswell,[12] T. Boulos,[14] G. Brandenburg,[9] C. Bromberg,[17] E. Buckley-Geer,[7]
H. S. Budd,[25] K. Burkett,[16] G. Busetto,[20] A. Byon-Wagner,[7] K. L. Byrum,[1] J. Cammerata,[12]
C. Campagnari,[7] M. Campbell,[16] A. Caner,[7] W. Carithers,[14] D. Carlsmith,[34] A. Castro,[20]
Y. Cen,[21] F. Cervelli,[23] H.Y. Chao,[28] J. Chapman,[16] M.-T. Cheng,[28] G. Chiarelli,[8]
T. Chikamatsu,[32] C.N. Chiou,[28] S. Cihangir,[7] A. G. Clark,[23] M. Cobal,[23] M. Contreras,[5]
J. Conway,[27] J. Cooper,[7] M. Cordelli,[8] C. Couyoumtzelis,[23] D. Crane,[1] J. D. Cunningham,[3]
T. Daniels[15] F. DeJongh,[7] S. Delchamps,[7] S. Dell'Agnello,[23] M. Dell'Orso,[23] L. Demortier,[26]
B. Denby,[23] M. Deninno,[2] P. F. Derwent,[16] T. Devlin,[27] M. Dickson,[25] J. Dittman,[6] S. Donati,[23]
R. B. Drucker,[14] A. Dunn,[16] K. Einsweiler,[14] J. E. Elias,[7] R. Ely,[14] E. Engels, Jr.,[22] S. Eno,[5]
D. Errede,[10] S. Errede,[10] Q. Fan,[25] B. Farhat,[15] I. Fiori,[2] B. Flaugher,[7] G. W. Foster,[7]
M. Franklin,[9] M. Frautschi,[18] J. Freeman,[7] J. Friedman,[15] H. Frisch,[5] A. Fry,[29] T. A. Fuess,[1]
Y. Fukui,[13] S. Funaki,[32] G. Gagliardi,[23] S. Galeotti,[23] M. Gallinaro,[20] A. F. Garfinkel,[24]
S. Geer,[7] D. W. Gerdes,[16] P. Giannetti,[23] N. Giokaris,[26] P. Giromini,[8] L. Gladney,[21]
D. Glenzinski,[12] M. Gold,[18] J. Gonzalez,[21] A. Gordon,[9] A. T. Goshaw,[6] K. Goulianos,[26]
H. Grassmann,[6] A. Grewal,[21] L. Groer,[27] C. Grosso-Pilcher,[5] C. Haber,[14] S. R. Hahn,[7]
R. Hamilton,[9] R. Handler,[34] R. M. Hans,[35] K. Hara,[32] B. Harral,[21] R. M. Harris,[7] S. A. Hauger,[6]
J. Hauser,[4] C. Hawk,[27] J. Heinrich,[21] D. Cronin-Hennessy,[6] R. Hollebeek,[21] L. Holloway,[10]
A. Hölscher,[11] S. Hong,[16] G. Houk,[21] P. Hu,[22] B. T. Huffman,[22] R. Hughes,[25] P. Hurst,[9]
J. Huston,[17] J. Huth,[9] J. Hylen,[7] M. Incagli,[23] J. Incandela,[7] H. Iso,[32] H. Jensen,[7]
C. P. Jessop,[9] U. Joshi,[7] R. W. Kadel,[14] E. Kajfasz,[7a] T. Kamon,[30] T. Kaneko,[32]
D. A. Kardelis,[10] H. Kasha,[35] Y. Kato,[19] L. Keeble,[30] R. D. Kennedy,[27] R. Kephart,[7]
P. Kesten,[14] D. Kestenbaum,[9] R. M. Keup,[10] H. Keutelian,[7] F. Keyvan,[4] D. H. Kim,[7]
H. S. Kim,[11] S. B. Kim,[16] S. H. Kim,[32] Y. K. Kim,[14] L. Kirsch,[3] P. Koehn,[25] K. Kondo,[32]
J. Konigsberg,[9] S. Kopp,[5] K. Kordas,[11] W. Koska,[7] E. Kovacs,[7a] W. Kowald,[6] M. Krasberg,[16]
J. Kroll,[7] M. Kruse,[24] S. E. Kuhlmann,[1] E. Kuns,[27] A. T. Laasanen,[24] N. Labanca,[23]
S. Lammel,[4] J. I. Lamoureux,[3] T. LeCompte,[10] S. Leone,[23] J. D. Lewis,[7] P. Limon,[7]
M. Lindgren,[4] T. M. Liss,[10] N. Lockyer,[21] C. Loomis,[27] O. Long,[21] M. Loreti,[20] E. H. Low,[21]
J. Lu,[30] D. Lucchesi,[23] C. B. Luchini,[10] P. Lukens,[7] J. Lys,[14] P. Maas,[34] K. Maeshima,[7]
A. Maghakian,[26] P. Maksimovic,[15] M. Mangano,[23] J. Mansour,[17] M. Mariotti,[20] J. P. Marriner,[7]
A. Martin,[10] J. A. J. Matthews,[18] R. Mattingly,[15] P. McIntyre,[30] P. Melese,[26] A. Menzione,[23]
E. Meschi,[23] G. Michail,[9] S. Mikamo,[13] M. Miller,[5] R. Miller,[17] T. Mimashi,[32] S. Miscetti,[8]
M. Mishina,[13] H. Mitsushio,[32] S. Miyashita,[32] Y. Morita,[13] S. Moulding,[26] J. Mueller,[27]
A. Mukherjee,[7] T. Muller,[4] P. Musgrave,[11] L. F. Nakae,[29] I. Nakano,[32] C. Nelson,[7]
D. Neuberger,[4] C. Newman-Holmes,[7] L. Nodulman,[1] S. Ogawa,[32] S. H. Oh,[6] K. E. Ohl,[35]
R. Oishi,[32] T. Okusawa,[19] C. Pagliarone,[23] R. Paoletti,[23] V. Papadimitriou,[31] S. Park,[7]
J. Patrick,[7] G. Pauletta,[23] M. Paulini,[14] L. Pescara,[20] M. D. Peters,[14] T. J. Phillips,[6]
G. Piacentino,[2] M. Pillai,[25] R. Plunkett,[7] L. Pondrom,[34] N. Produit,[14] J. Proudfoot,[1] F. Ptohos,[9]
G. Punzi,[23] K. Ragan,[11] F. Rimondi,[2] L. Ristori,[23] M. Roach-Bellino,[33] W. J. Robertson,[6]
T. Rodrigo,[7] J. Romano,[5] L. Rosenson,[15] W. K. Sakumoto,[25] D. Saltzberg,[5] A. Sansoni,[8]
V. Scarpine,[30] A. Schindler,[14] P. Schlabach,[9] E. E. Schmidt,[7] M. P. Schmidt,[35] O. Schneider,[14]

Submitted to Physical Review D February 1, 1995

G. F. Sciacca,[23] A. Scribano,[23] S. Segler,[7] S. Seidel[18] Y. Seiya,[32] G. Sganos,[11] A. Sgolacchia,[2]
M. Shapiro,[14] N. M. Shaw,[24] Q. Shen,[24] P. F. Shepard,[22] M. Shimojima,[32] M. Shochet,[5]
J. Siegrist,[29] A. Sill,[31] P. Sinervo,[11] P. Singh,[22] J. Skarha,[12] K. Sliwa,[33] D. A. Smith,[23]
F. D. Snider,[12] L. Song,[7] T. Song,[16] J. Spalding,[7] L. Spiegel,[7] P. Sphicas,[15] A. Spies,[12]
L. Stanco,[20] J. Steele,[34] A. Stefanini,[23] K. Strahl,[11] J. Strait,[7] D. Stuart,[7] G. Sullivan,[5]
K. Sumorok,[15] R. L. Swartz, Jr.,[10] T. Takahashi,[19] K. Takikawa,[32] F. Tartarelli,[23] W. Taylor,[11]
Y. Teramoto,[19] S. Tether,[15] D. Theriot,[7] J. Thomas,[29] T. L. Thomas,[18] R. Thun,[16] M. Timko,[33]
P. Tipton,[25] A. Titov,[26] S. Tkaczyk,[7] K. Tollefson,[25] A. Tollestrup,[7] J. Tonnison,[24]
J. F. de Troconiz,[9] J. Tseng,[12] M. Turcotte,[29] N. Turini,[2] N. Uemura,[32] F. Ukegawa,[21]
G. Unal,[21] S. van den Brink,[22] S. Vejcik, III,[16] R. Vidal,[7] M. Vondracek,[10] R. G. Wagner,[1]
R. L. Wagner,[7] N. Wainer,[7] R. C. Walker,[25] C.H. Wang,[28] G. Wang,[23] J. Wang,[5] M. J. Wang,[28]
Q. F. Wang,[26] A. Warburton,[11] G. Watts,[25] T. Watts,[27] R. Webb,[30] C. Wendt,[34] H. Wenzel,[14]
W. C. Wester III,[14] T. Westhusing,[10] A. B. Wicklund,[1] E. Wicklund,[7] R. Wilkinson,[21]
H. H. Williams,[21] P. Wilson,[5] B. L. Winer,[25] J. Wolinski,[30] D. Y. Wu,[16] X. Wu,[23] J. Wyss,[20]
A. Yagil,[7] W. Yao,[14] K. Yasuoka,[32] Y. Ye,[11] G. P. Yeh,[7] P. Yeh,[28] M. Yin,[6] J. Yoh,[7] T. Yoshida,[19]
C. Yousef,[17] D. Yovanovitch,[7] I. Yu,[35] J. C. Yun,[7] A. Zanetti,[23] F. Zetti,[23] L. Zhang,[34]
S. Zhang,[16] W. Zhang,[21] and S. Zucchelli[2]

(CDF Collaboration)

[1]Argonne National Laboratory, Argonne, Illinois 60439
[2]Istituto Nazionale di Fisica Nucleare, University of Bologna, I-40126 Bologna, Italy
[3]Brandeis University, Waltham, Massachusetts 02254
[4]University of California at Los Angeles, Los Angeles, California 90024
[5]University of Chicago, Chicago, Illinois 60637
[6]Duke University, Durham, North Carolina 27708
[7]Fermi National Accelerator Laboratory, Batavia, Illinois 60510
[8]Laboratori Nazionali di Frascati, Istituto Nazionale di Fisica Nucleare, I-00044 Frascati, Italy
[9]Harvard University, Cambridge, Massachusetts 02138
[10] University of Illinois, Urbana, Illinois 61801
[11]Institute of Particle Physics, McGill University, Montreal H3A 2T8, and University of Toronto, Toronto M5S 1A7, Canada
[12]The Johns Hopkins University, Baltimore, Maryland 21218
[13]National Laboratory for High Energy Physics (KEK), Tsukuba, Ibaraki 305, Japan
[14]Lawrence Berkeley Laboratory, Berkeley, California 94720
[15]Massachusetts Institute of Technology, Cambridge, Massachusetts 02139
[16]University of Michigan, Ann Arbor, Michigan 48109
[17]Michigan State University, East Lansing, Michigan 48824
[18]University of New Mexico, Albuquerque, New Mexico 87131
[19]Osaka City University, Osaka 588, Japan
[20]Universita di Padova, Instituto Nazionale di Fisica Nucleare, Sezione di Padova, I-35131 Padova, Italy
[21]University of Pennsylvania, Philadelphia, Pennsylvania 19104
[22]University of Pittsburgh, Pittsburgh, Pennsylvania 15260
[23]Istituto Nazionale di Fisica Nucleare, University and Scuola Normale Superiore of Pisa, I-56100 Pisa, Italy
[24]Purdue University, West Lafayette, Indiana 47907
[25]University of Rochester, Rochester, New York 14627
[26]Rockefeller University, New York, New York 10021
[27]Rutgers University, Piscataway, New Jersey 08854
[28]Academia Sinica, Taiwan 11529, Republic of China
[29]Superconducting Super Collider Laboratory, Dallas, Texas 75237
[30]Texas A&M University, College Station, Texas 77843
[31]Texas Tech University, Lubbock, Texas 79409
[32]University of Tsukuba, Tsukuba, Ibaraki 305, Japan
[33]Tufts University, Medford, Massachusetts 02155
[34]University of Wisconsin, Madison, Wisconsin 53706
[35]Yale University, New Haven, Connecticut 06511
[a]Visitor

1 January 1994

## Abstract

We present an analysis of data from $p\overline{p}$ collisions at a center of mass energy of $\sqrt{s}$ = 1800 $GeV$. A measurement is made of the ratio $R \equiv \sigma \cdot B(p\overline{p} \rightarrow W \rightarrow e\nu) \;/\; \sigma \cdot B(p\overline{p} \rightarrow Z^0 \rightarrow ee)$. The data represent 19.6 $pb^{-1}$ collected by the Collider Detector at Fermilab (CDF) during the 1992-1993 collider run of the Fermilab Tevatron. We find $R$ = 10.90 ± 0.32 (*stat.*) ± 0.29 (*sys.*), and from this value we extract a measurement of the $W \rightarrow e\nu$ branching ratio $\Gamma(W \rightarrow e\nu)/\Gamma(W)$ = 0.1094 ± 0.0033(*stat.*) ± 0.0031(*sys.*). From this branching ratio we set a limit on the top quark mass of $m_{top} > 62$ $GeV/c^2$ at the 95% confidence level. In contrast to direct searches for the top quark, this limit makes no assumptions about the allowed decay modes of the top quark. In addition, we use a calculation of the leptonic width $\Gamma(W \rightarrow e\nu)$ to obtain a value for the $W$ total decay width: $\Gamma(W)$ = 2.064 ±0.060(*stat.*) ± 0.059(*sys.*) $GeV$.

PACS Numbers 13.38.+c, 12.15.Ff, 14.80.Dq, 14.50.Er.

# 1. Introduction

The $W$ boson width, $\Gamma(W)$, is a fundamental parameter that is well-predicted in the Standard Model. The $W$ decays with approximately equal probability to each of three lepton families and to the two quark families that are kinematically available. The quark families receive an additional factor of three in their decay probabilities due to their color charge. Hence, the branching ratio of the $W$ into $(\ell, \overline{\nu_\ell})$ is approximately $\frac{1}{9}$. By dividing a calculation of the $W$ leptonic partial width, $\Gamma(W \rightarrow \ell\nu)$, by the leptonic branching ratio, one may predict that the $W$ width is $\approx 2.1$ $GeV$. This article presents a measurement of $W$ boson decay width, $\Gamma(W)$, and of the leptonic branching ratio, $\Gamma(W \rightarrow e\nu)/\Gamma(W)$.

The $W$ width is altered if additional decay modes are available to the $W$. In particular, if the $W$ can decay to a light top quark ($m_t < M_W - m_b$) and a $b$ quark, the $W$

width changes to $\Gamma(W) \approx 2.8\ GeV$ and the leptonic branching ratio changes to $\Gamma(W\to\ell\nu)/\Gamma(W) \approx 1/12$. Direct searches[1] have set a limit of $m_t > 131\ GeV/c^2$ (95% C.L.), but these limits assume that the top always decays via the reaction $t\to Wb$. We have presented evidence[2] that suggests that the top quark mass is $m_t = 174 \pm 17\ GeV/c^2$. If, however, the top is light and has decays other than $t\to Wb$ that have been missed by the direct searches, or if other weak isodoublets exist that couple to the *W*, then the *W* width could see a contribution from these sources. The top could have non-Standard Model decays, for example, if a charged Higgs exists and $t\to H^+b$ were the dominant decay channel. Then the top could be missed by direct searches for $t\to Wb$.[3] These enhancements to the *W* width are independent of assumptions regarding the allowed decays of the daughters of the *W*.

The *W* decays with universal coupling to pairs of fermions within weak isodoublets. The partial width into fermion pairs is calculated to be:[4] $\Gamma_0(W\to f\overline{f}') = |V_{ff'}|^2 N_c\, g^2 M_W/48\pi$, where $V_{ff'}$ is the CKM matrix element for two quarks and is 1.0 for leptons. The color factor $N_c$ is 3 for quarks and is 1 for leptons. The variable $M_W$ is the *W* boson mass, and $g$ is the *W*'s coupling to fermions. In the Standard Model the *W*-fermion coupling is given by $g^2 = \frac{8}{\sqrt{2}} G_F M_W^2$, where $G_F$ is the Fermi coupling constant derived from the muon lifetime.

This simple calculation of the *W* width receives corrections at next-to-leading order in *QCD*. At lowest order, the *W* may decay with equal probability to each of three lepton families and to two quark families, assuming that the top quark is heavy (with a color factor of three on the quark decays). Quark decays receive an additional *QCD K*-factor enhancement at $O(\alpha_s)$ due to vertex graphs involving gluon exchange. Rosner *et al.*[5] have thus calculated:

$$\Gamma_0(W\to\ell\nu)/\Gamma_0(W) = [3 + 6(\ 1 + \alpha_s\ (M_W)/\pi)]^{-1} = 0.1084 \pm 0.0002.$$

$$\Gamma_0(W) = 2.075 \pm 0.021\ GeV,$$

The *W* width also receives electroweak corrections due to next-to-leading order graphs which alter the effective coupling $g$ at the *W*-fermion vertex for all fermions. Within the context of the Standard Model the *W* width receives vertex and

Bremsstrahlung corrections[4] that depend upon the top and Higgs masses. The corrections can be summarized in the equation:

$$\Gamma(W \rightarrow f\bar{f}')_{SM} = \Gamma_0(W \rightarrow f\bar{f}')\cdot\left[1+\delta_V+\delta_W(0)+\delta_\mu\right],$$

where $\delta_W(0)$ is the correction to the width from loops at the $W$-fermion vertex involving $Z^0$'s or a Standard Model Higgs, $\delta_V$ describes boson self-energies, and $\delta_\mu$ is a correction made necessary when $g$ is parameterized using the $W$ mass and the value of $G_F$ from muon decay.[6] The factor $\delta_W(0)$ also incorporates corrections to the $W$ propagator from the top quark that are not absorbed into the $W$ mass. The vertex corrections from the Standard Model Higgs cause $\Gamma(W)$ to change by approximately 1% as the Higgs mass varies from 50 $GeV/c^2$ to 1000 $GeV/c^2$, while the correction from $\overline{tb}$ loops changes $\Gamma(W)$ by approximately 4% as the top quark mass varies from 80 $GeV/c^2$ to 200 $GeV/c^2$.[4]

Because the electroweak vertex corrections to $g$ above are nearly identical for both leptons and quarks, these corrections affect only the $W$ width. In the case of the leptonic branching ratio, the coupling $g$ cancels out and hence the leptonic branching ratio is almost competely insensitive to these vertex corrections. Including the radiative corrections, and for the particular choice of $m_t$ = 140 $GeV/c^2$ and $M_{Higgs}$ = 100 $GeV/c^2$, Rosner, *et al.*, find:[5]

$$\Gamma(W)_{SM} = 0.996 \times \Gamma_0(W) = 2.067 \pm 0.021 \ GeV,$$

$$\Gamma(W \rightarrow \ell\nu)_{SM} \,/\, \Gamma(W)_{SM} = \Gamma_0(W \rightarrow \ell\nu) \,/\, \Gamma_0(W) = 0.1084 \pm 0.0002.$$

To test the Standard Model, it is desirable to measure both $\Gamma(W\rightarrow\ell\nu)/\Gamma(W)$ and $\Gamma(W)$. The branching ratio is the most sensitive quantity for new decay modes, since the uncertainty in the theoretical prediction of $\Gamma(W)$ due to the uncertainty in the measured $W$ mass cancels in the branching ratio. The total width, furthermore, may be used along with the leptonic branching ratio to obtain a measure of $\Gamma(W\rightarrow\ell\nu)$. The leptonic partial width is predicted to be $g^2M_W/48\pi$ , and deviations in the measured value indicate values of the $W$-fermion coupling $g^2$different from that given by the Standard Model.

## 1.1 Measurement of $\Gamma(W)$ from $W$ and $Z^0$ Cross Sections

The $W$ leptonic branching ratio may be extracted from a measurement of the ratio, $R$, of the cross sections times leptonic branching ratios of the $W$ and $Z^0$ in $p\overline{p}$ collisions.[7] The ratio $R$ may be expressed as:

$$R \equiv \frac{\sigma \cdot B(p\overline{p}\rightarrow W\rightarrow \ell\nu)}{\sigma \cdot B(p\overline{p}\rightarrow Z^0\rightarrow \ell\ell)} = \frac{\sigma(p\overline{p}\rightarrow W)}{\sigma(p\overline{p}\rightarrow Z^0)} \, \frac{\Gamma(W\rightarrow \ell\nu)}{\Gamma(Z^0\rightarrow \ell\ell)} \, \frac{\Gamma(Z^0)}{\Gamma(W)}$$

On the right hand side, the ratio $\sigma(p\overline{p}\rightarrow W) / \sigma(p\overline{p}\rightarrow Z^0)$ of the production cross sections may be calculated from the boson couplings and knowledge of the proton structure. The $Z^0$ total width, $\Gamma(Z^0)$, and the leptonic partial width, $\Gamma(Z^0\rightarrow \ell^+\ell^-)$, are well-measured by the LEP experiments.[8] Thus, a measurement of $R$ yields a precise measurement of the $W$ leptonic branching ratio $\Gamma(W\rightarrow \ell\nu)/\Gamma(W)$. If one then divides a calculation of the leptonic width $\Gamma(W\rightarrow \ell\nu)$ by the measured branching ratio, a value is extracted for the total decay width, $\Gamma(W)$, of the $W$. Note, however, that the width extracted from the branching ratio is not sensitive to electroweak vertex corrections to the coupling $g$, since it is normalized to the calculated $\Gamma(W\rightarrow \ell\nu)$. While in principle the corrections to the $W$-fermion coupling would also alter the production cross section $\sigma(p\overline{p}\rightarrow W)$, a direct measurement of $\Gamma(W)$, such as the one described in Section 1.2, is desirable as a check of these effects.

## 1.2 Previous Measurements of $\Gamma(W)$

The measurements of the $W$ width extracted from the ratio $R$ are given in Table 1.1. In Table 1.1, mode = "e" or "$\mu$" refers to the decay mode of the $W$ (or $Z^0$) used in the measurement. This long paper reports on a measurement of $R$ made by the CDF Collaboration[9] with a relative uncertainty of 4.1%. The best measurement of the $W$ width previous to the most recent CDF result has an error of 7.6%. The combination of all published measurements from $R$ yields a value for the $W$ total decay width, $\Gamma(W) = 2.07 \pm 0.07$ *GeV*, an accuracy of 3.5%. Prior to the most recent CDF measurement, the world average had an uncertainty of 5.2%.

The *W* width has also been measured directly from studies of the *W* transverse mass lineshape in $p\overline{p}$ collisions, where $M_T^2 \equiv (|\vec{p}_T^{\,e}| + |\vec{p}_T^{\,\nu}|)^2 - (\vec{p}_T^{\,e} + \vec{p}_T^{\,\nu})^2$ and $\vec{p}_T^{\,e}$ and $\vec{p}_T^{\,\nu}$ are components of the electron and neutrino momenta transverse to the *p* and $\overline{p}$ beams. These direct measurements complement the indirect value from the *W* and $Z^0$ cross sections because they have entirely different systematic uncertainties. More importantly, they are free of the theoretical assumptions regarding the *W* coupling to fermions. Direct measurements of $\Gamma(W)$ from the transverse mass distribution at hadron colliders will approach the 1% level with the 1 $fb^{-1}$ of data anticipated at Fermilab in 1998.[16]

**Table 1.1: Previous Measurements of $\Gamma(W)$.**

| Experiment | Method | Mode | $\sqrt{s}$ *(TeV)* | $\Gamma(W)$ *(GeV)* |
|---|---|---|---|---|
| CDF[9] | *R* | *e* | 1.8 | 2.064 ± 0.085 |
| CDF[10] | *R* | *e* | 1.8 | 2.14 ± 0.20 |
| CDF[11] | *R* | $\mu$ | 1.8 | 2.21 ± 0.27 |
| UA1[12] | *R* | $\mu$ | 0.63 | 2.19 ± 0.30 |
| UA2[13] | *R* | *e* | 0.63 | 2.10 ± 0.16 |
| UA1[14] | Direct | *e* | 0.63 | 2.8 ± 1.9 |
| CDF[15] | Direct | *e* | 1.8 | 2.11 ± 0.32 |

The *W* width will also be determined by the LEP-200 experiments at center of mass energy near $\sqrt{s} = 2M_W$ from an endpoint analysis of the *W* daughter lepton energy spectrum. This measurement of $\Gamma(W)$ is also direct one, like the lineshape measurements at $p\overline{p}$ colliders, and the LEP-200 experiments anticipate an accuracy on $\Gamma(W)$ of 200 *MeV*, or 10%.[17]

## 1.3 1992-1993 Run of CDF

The data presented in this paper were collected by the Collider Detector at Fermilab observing $p\overline{p}$ collisions at a center of mass energy of $\sqrt{s} = 1.8$ *TeV*. During the 1992-1993 collider run, the Fermilab Tevatron delivered a total integrated luminosity of $\int Ldt = 27.3\ pb^{-1}$, with typical instantaneous luminosities of $4.0 \times 10^{30}\ cm^{-2}sec^{-1}$ and a peak instantaneous luminosity of $9.7 \times 10^{30}\ cm^{-2}sec^{-1}$. The Collider Detector at Fermilab wrote 20.6 $pb^{-1}$ of data to tape, with the 30% loss dominated by operational problems. This compares to 4.0 $pb^{-1}$ of data collected in

CDF's previous 1988-1989 run. Approximately 1.0 $pb^{-1}$ of this year's data was discarded after the fact because of hardware difficulties during data taking. In the 19.6 $pb^{-1}$ of data remaining, approximately 20000 $W \to e\nu$ and 1600 $Z^0 \to e^+e^-$ decays were observed from all triggers, as were 7000 $W \to \mu\nu$ and 600 $Z^0 \to \mu^+\mu^-$ decays. Note that, while same data sample is being reported on as in reference [9], our measurement of the luminosity has changed by approximately 10%. This change is documented in reference [2]. Thus, while reference [9] quotes an integrated luminosity of 21.7 $pb^{-1}$, that same data sample is here estimated as 19.6 $pb^{-1}$. Note that $R$ is independent of the luminosity.

### 1.4 Strategy of This Measurement

The signature of high-$P_T$ leptons from $W$ and $Z^0$ decay is quite distinctive in the environment of hadron collisions. As such, the decay of $W$ and $Z^0$ bosons into leptons provides a clean experimental measurement of their production. Experimentally, the cross sections times branching ratios are found from:

$$\sigma \cdot B(p\overline{p} \to W \to \ell\nu) = \frac{N_W^{Candidates} - N_W^{Background}}{A_W \epsilon_W \int L dt}$$

$$\sigma \cdot B(p\overline{p} \to Z^0 \to \ell^+\ell^-) = \frac{N_Z^{Candidates} - N_Z^{Background}}{A_Z \epsilon_Z \int L dt}$$

where $N_W^{Candidates}$ and $N_Z^{Candidates}$ are the number of $W$ and $Z^0$ candidates observed; $A_W$ and $A_Z$ are the "acceptance" for the $W$ and $Z^0$ decays (which includes the efficiency for the kinematic cuts on the leptons and the geometric acceptance of the detector); $\varepsilon_W$ and $\varepsilon_Z$ are the efficiency for the $W$ and $Z^0$ to pass the lepton identification criteria, and $\int L dt$ is the integrated luminosity of the experiment. Measuring the ratio of the cross sections allows some of the quantities (as well as their uncertainties) on the right hand sides to cancel.

The strategy of this cross section ratio measurement will be to require at least one charged lepton passing tight selection criteria in both $W$ and $Z^0$ decays to fall in the central, barrel region of the detector, where magnetic tracking analysis augments the calorimeter measurements (See Section 2). For this measurement, only electrons will be considered.

The number of $Z^0$'s limits the statistical accuracy of the $R$ measurement of $\Gamma(W)$, and this tactic of requiring a central electron common to both $W$ and $Z^0$ decays decreases the available $Z^0$ statistics even further. From a simple Monte Carlo (described in Section 7), we learn that this requirement is approximately 80% efficient for $Z^0$'s. It is only ~ 60% efficient for $W$'s, but the $W$'s do not statistically limit the overall measurement. Requiring a common central electron for both $W$'s and $Z^0$'s will increase the statistical error on $R$ from 2.6% to 2.9%.

This method of requiring one central electron common to both $W$ and $Z^0$ decays, however, decreases the systematic error in the measurement. The selection criteria for the central electron (which appear in the factors $\varepsilon_W$ and $\varepsilon_Z$) will almost completely cancel in the ratio $R$ because they are common to $W$'s and $Z^0$'s. Imposing tight selection criteria on the central lepton allows loose selection criteria to be applied on the second lepton (either electron or neutrino). The systematic error in the ratio of acceptances is also smaller than for the individual acceptances when a common central electron is required. Furthermore, because of the magnetic analysis in the barrel region of the detector, systematic errors from $W$ and $Z^0$ backgrounds are much smaller in the barrel than in the end-cap regions. These smaller uncertainties offset the expected 0.3% increase in statistical error from requiring the common central electron.

### 1.5 Electrons in $p\ \overline{p}$ Collisions

In addition to presenting a measurement of the $W/Z^0$ cross section ratio in $p\overline{p}$ collisions, this paper attempts to describe the other sources of inclusive electrons. Electrons from $W$ and $Z^0$ decay account for only a fraction of the high-$P_T$ inclusive electrons observed in our detector, and the study of these other electrons is not only of interest in determining the backgrounds to the $W/Z^0$ samples, but of interest in its own right. We anticipate that electrons in $p\overline{p}$ collisions fall into three categories: 1) electrons which come in $e^+e^-$ pairs, either from photon conversions or Dalitz decays; 2) electrons from heavy quark decay; and 3) hadrons that fake electrons. We discuss techniques to diffentiate between these different sources of electrons and their relative contributions to the inclusive electrons observed.

### 1.6 Outline of Paper

The article will proceed as follows: Section 2 describes electron and neutrino identification in the CDF detector. Section 3 describes the selection of the inclusive electron sample and the separation of this sample into $W$ and $Z^0$ samples and a non-$W/Z^0$ control sample of electrons. Section 4 describes the physics sources of high-$P_T$ electrons in the non-$W/Z^0$ sample. This description is used in Section 5, where we discuss the make-up of the $W$ sample and estimate the backgrounds. Section 6 discusses the $Z^0$ candidate sample and its backgrounds. Section 7 describes the Monte Carlo program used to determine the acceptance ratio $A_W/A_Z$. Section 8 describes the the efficiencies $\varepsilon_W$ and $\varepsilon_Z$. Section 9 provides a cross check of the $R$ measurement, and Section 10 summarizes the extraction of $\Gamma(W)$ from the cross sections.

## 2. Electron and Neutrino Identification

Many previous publications[18] give detailed descriptions of the various components of the Collider Detector at Fermilab (CDF) detector. In this section, we summarize briefly the physical characteristics of those detector components relevant for electron and neutrino identification and describe their performance during the 1992-1993 run.

### 2.1 The CDF Detector

CDF is a cylindrical detector with a central barrel region, two end-cap (plug) regions closing the barrel, and two far-forward detector regions (see Figure 2.1). It features electromagnetic (EM) and hadronic (Had) shower counters arranged in projective tower geometry, as well as charged particle tracking chambers. The tracking chambers are immersed in a 1.4 T magnetic field oriented along the proton beam direction provided by a 3 m diameter, 5 m long superconducting solenoidal magnet coil. Although not used in this analysis, drift chambers outside the hadron calorimeters for muon detection cover the region $|\eta| < 1.0$.[19]

### *2.1.2 Calorimeters*

Table 2.1 summarizes the calorimeter subsystems at CDF. In the central barrel region covering the angular region $-1.1 < \eta < 1.1$, the electromagnetic (CEM) and hadron (CHA, WHA) calorimeters are made of absorber sheets interspersed with scintillator. Plastic light guides bring the light up to two phototubes per EM tower. The towers are constructed in 48 wedges, each consisting of 10 towers in $\eta$ by one tower in $\phi$ (see Figure 2.2). Proportional chambers are embedded near shower maximum, 6 radiation lengths ($X_0$) within the EM calorimeters. These chambers, called Central Electron Strip (CES) chambers, have wires in the $r$-$\phi$ view and cathode strips in the $z$ view. The CES is summarized in Table 2.2. A second set of proportional chambers, the Central Pre-Radiator (CPR), placed in between the front face of the EM calorimeters and the magnet coil, act as a shower pre-sampler. Both the CES and CPR are split into two separate readout segments in the $z$ direction, so that the wires do not run along the full length of the calorimeter, but are read out in two divisions.

In the plug end-cap and forward detector regions, the towers are made of absorber sheets sandwiched with conductive plastic proportional tube arrays. Cathode strips outside the plastic tubes are read out and provide tower segmentation. Near shower maximum in the plug EM (PEM) calorimeter, a layer with finer-spaced strips spacing provides shower profile and precise position determination.

Arrays of scintillator planes are mounted on the front face of each of the far-forward EM shower counters. These planes, called the Beam-Beam Counters (BBC's) are shown in Figure 2.1 and are used to signal an inelastic collision. At lower instantaneous luminosities, a coincidence of at least one hit in each plane of the BBC's is required to initiate the trigger system. Each BBC consists of an array of 16 scintillator planes and 16 photomultiplier tubes that encircle the 360° around beam pipe and cover the pseudorapidity range $3.24 < |\eta| < 5.90$. At higher instantaneous luminosities, the mean number of $p\overline{p}$ interactions per crossing of $p$ and $\overline{p}$ bunches is sufficiently high that the BBC coincidence was unnecessary to guarantee the presence of an inelastic collision.

**Table 2.1 Description of the CDF Calorimeter Subsystems**

| | CEM | CHA,WHA | PEM | PHA | FEM | FHA |
|---|---|---|---|---|---|---|
| Energy Resolution (% / $\sqrt{E}$) | 13.5 | 80 | 28 | 130 | 25 | 141 |
| Angular Coverage ( in $\lvert\eta\rvert$ ) | < 1.1 | < 1.3 | 1.1 - 2.4 | 1.3 - 2.4 | 2.2 - 4.2 | 2.3 - 4.2 |
| Segmentation ($\Delta\eta \times \Delta\phi$) | 0.1 × 15° | 0.1 × 15° | 0.1 × 5° | 0.1 × 5° | 0.1 × 5° | 0.1 × 5° |
| Active Medium | lead, scintillator | iron, scintillator | lead, proportional tube | iron, proportional tube | lead, proportional tube | iron, proportional tube |
| Position Resolution ($r$-$\phi$ × $z$) | 0.2 cm × 0.2 cm[a] | 10 cm × 5 cm | 0.2 cm × 0.2 cm | 2 cm × 2 cm | 0.2 cm × 0.2 cm | 3 cm × 3 cm |
| Longitudinal Depth | 18 $X_0$,[b]<br>1.0 $\Lambda_{abs}$ | 4.7 $\Lambda_{abs}$ | 19 $X_0$,<br>1.0 $\Lambda_{abs}$ | 5.7 $\Lambda_{abs}$ | 25 $X_0$,<br>0.8 $\Lambda_{abs}$ | 7.7 $\Lambda_{abs}$ |

a) Using the CES chambers b) Including the 1 $X_0$ solenoidal coil

**Table 2.2 Description of the Shower Max Detector (CES) and Pre-Shower Detector (CPR).**

| | CES Chamber | | CPR Chamber |
|---|---|---|---|
| | Wires ($r$-$\phi$ view) | Strips ($z$ view) | Wires ($r$-$\phi$ view) |
| Number of Channels | 32 | 69,[a] 59[b] | 16 |
| Spacing (cm) | 1.45 | 1.67,[a] 2.07[b] | 2.2 |
| Spatial Resolution (cm) | 0.2 | 0.2 | - |
| Saturation Energy ($GeV$) | 150 | 150 | >150 |
| Chamber length in $z$ (cm) | 234 | | 103 |
| Chamber Width in $\phi$ (°) | 14.0 | | 12.1 |

a) for CES segment between 6 cm $< z <$ 115 cm

b) for CES segment between 115 cm $< z <$ 240 cm

### *2.1.2 Charged Particle Tracking*

Within the 1.4 T axial magnetic field of the solenoidal magnet are three detectors for charged particle tracking. The Silicon Vertex Detector (SVX) is a four-layer silicon microvertex detector with single-sided readout to provide precise $r$-$\phi$ information for the reconstruction of track impact parameters. The Vertex Tracking Chamber (VTX) is a time projection chamber in 8 modules with a maximum drift distance of 10 *cm*. It provides reconstruction of the primary event vertex in the $z$ direction with $\sigma_z = 1$ *mm* accuracy. The Central Tracking Chamber (CTC) is a large drift chamber with 84 layers of sense wires organized into 9 superlayers. Four of the superlayers are tilted ± 3° with respect to the $z$ axis so as to provide stereo position measurement of charged particle tracks. The charge collected on its wires allow particle identification to be performed through *dE/dx* measurements with $1.5\sigma$ $e$-$\pi$ separation at 5 *GeV/c*. The three tracking chambers are summarized in Table 2.3.

**Table 2.3: Description of the Charged Particle Tracking Chambers**

| | Silicon Vertex Detector (SVX) | Vertex Tracking Chamber (VTX) | Central Tracking Chamber (CTC) |
|---|---|---|---|
| Polar Angle Coverage | $\lvert\eta\rvert < 1.0$ | $\lvert\eta\rvert < 3.25$ | $\lvert\eta\rvert < 1.5$ |
| Inner, Outer Tracking Radii (cm) | 2.7,<br>7.9 | 8, [a]<br>22 | 30.9,<br>132.0 |
| Length (cm) | 26 | 280 | 320 |
| Layers | 4 | 24 | 60 axial,<br>24 stereo |
| Strip or Wire Spacing | 60 $\mu m$ (inner 3 lay.)<br>55 $\mu m$ (outer layer) | 6.3 mm | 10 mm |
| Spatial Resolution | 15 $\mu m$ ($r$-$\phi$) | 200-500 $\mu m$ ($r$-$z$) | 200 $\mu m$ ($r$-$\phi$)<br>4 $mm$ ($r$-$z$) |
| Momentum Resolution | $\delta P_T/P_T = 0.001 \times P_T$[b] | - | $\delta P_T/P_T = 0.002 \times P_T$ |
| Thickness ($\theta = 90°$) | $\approx 0.035\ X_0$ | $\approx 0.045\ X_0$ | $\approx 0.015\ X_0$ |

[a] For inner 2 modules. Outer 6 modules are 3 cm inner radius.

[b] With both CTC and SVX hits incorporated into track fit.

### 2.2 Electron Cluster Candidates

Electron identification begins with a clustering algorithm to identify electron showers. An electron cluster consists of a seed tower (the tower in the cluster with the largest energy) and shoulder towers (adjacent towers incorporated into the cluster). Towers with electromagnetic (EM) transverse energy $E_T > 3\ GeV$ are eligible to be seed towers.[20] Towers with EM $E_T > 0.1\ GeV$ are eligible to be shoulder towers. Beginning with each seed tower, a cluster is formed by incorporating neighboring shoulder towers until either no further adjacent towers may be incorporated or until the maximum cluster size is reached. The maximum cluster size is restricted to three towers in pseudorapidity ($\Delta\eta \approx 0.3$) by one tower in azimuth ($\Delta\phi \approx 15°$) in the central region, five towers in pseudorapidity ($\Delta\eta \approx 0.5$) by five towers in azimuth ($\Delta\phi \approx 25°$) in the plug region, and seven towers in pseudorapidity ($\Delta\eta \approx 0.6$) by seven towers in azimuth ($\Delta\phi \approx 35°$) in the forward region. Finally, it is required that the EM $E_T$ of the cluster be greater than 5 $GeV$ and that the ratio of hadronic $E_T$ to electromagnetic $E_T$ be less than 0.125.[21]

### 2.3 Fiducial Volume for Electrons

Figure 2.3 shows schematically the fiducial volume of the detector for electrons used in this analysis. Of the central region defined by $|\eta| < 1.1$, 78.9% of the area in $\eta$-$\phi$ space is in the fiducial volume for electrons; 78.5% of the region $|\eta| < 3.6$ is in the fiducial volume for electrons.

In the central region, the electron position is determined using the CES shower position and is required to lie within 21 $cm$ of the tower center in the $r$-$\phi$ view so that the shower is fully contained in the active region. The region $|\eta| < 0.05$, where the two halves of the detector meet, is excluded. The region $0.77<\eta<1.0$, $75°<\phi<90°$ (the "chimney") is uninstrumented because it is the penetration for the cryogenic connections to the solenoidal magnet. In addition, the region $1.05 < |\eta| < 1.10$ is excluded because of the smaller depth of the electromagnetic calorimeter in this region.

In the plug and forward regions, the electron position is determined from the seed tower (see Section 2.1). The boundaries between detector regions, $1.1 < |\eta| < 1.2$

and 2.2 $< |\eta| <$ 2.4 are excluded because of the overlap between detectors. The region 3.6 $< |\eta| <$ 4.2 in the forward region is excluded. In both the plug and forward calorimeter, the electron seed tower is required not to be adjacent to the quadrant boundaries. This is ± 5° around each quadrant boundary.

## 2.4 Central Electron Identification

Electron identification in the central region is made more powerful by the presence of the Central Tracking Chamber, the Central Strip Chambers, and the Central Pre-Radiator. Using the electron identification variables described here and the cut values in Table 3.1 for tight central electron candidates, the fraction of hadron jets falsely identified as electrons is estimated to be $2 \times 10^{-5}$ for jets with $E_T > 20\ GeV$ (note at CDF that the dominant background to high-$P_T$ electron candidates is not isolated pions, but jets of hadrons). The CPR may be used to further reduce the misidentification rate by one order of magnitude. The purity of electron candidates with $E_T > 20\ GeV$ with the cuts of Table 3.1 is approximately 84%.

### *2.4.1 Calorimeter Transverse Profile*

The transverse profile, or "*Lshr*," of a central electron allows a comparison of the lateral sharing of energy in the calorimeter towers of an electron cluster to electron shower shapes from test beam data. The variable *Lshr* is defined as:

$$Lshr = 0.14 \cdot \sum_i \frac{E_i^{Adj} - E_i^{Prob}}{\sqrt{0.14^2 \cdot E + (\Delta E_i^{Prob})^2}}$$

where $E_i^{Adj}$ is the measured energy (in $GeV$) in a tower adjacent to the seed tower, $E_i^{Prob}$ is the expected energy (in $GeV$) in the adjacent tower, $0.14\sqrt{E}$ (in $GeV$) is the error on the energy measurement, and $\Delta E_i^{Prob}$ (in $GeV$) is the error on the energy estimate. $E_i^{Prob}$ is calculated using a parameterization from test beam data. The distribution of *Lshr* for inclusive and *W* electrons is shown in Figure 2.4(a).

### *2.4.2 Strip Chamber Pulse Height*

The CES chamber, embedded 6 radiation lengths into the central electromagnetic calorimeter, can be used to observe the longitudinal development of a shower. An electromagnetic shower in the calorimeters is generally initiated much earlier for an electron than for a hadron. Shown in Figure 2.5(a) is the variable $CES/p \equiv (\Sigma Q_i)/p$ for electrons and hadrons, where $Q_i$ is the charge on a strip (in ADC counts), $p$ is the track's momentum (in *GeV/c*), and the sum is over the 5 strips ($z$ view) around the track's position extrapolated to the strip chambers.

### *2.4.3 Strip Chamber Pulse Height Shape*

The pulse height shape in the CES is also used for electron identification. The pulse height shape is compared to test beam data using a $\chi^2$ test. The variable $\chi^2_{strip}$ is the $\chi^2$ of the fit of the energy deposited on the each of the 11 strips in $z$ in the CES shower compared to the test beam shape. A similar variable $\chi^2_{wire}$ tests the energy deposition on the wires in the $r$-$\phi$ view. The variable $\chi^2_{strip}$ for inclusive electron candidates and for electrons from $W$ decays is shown in Figure 2.4(b).

### *2.4.4 Charged Track Requirement*

Electromagnetic clusters in the calorimeters can arise from neutral particles, such as $\pi^0 \rightarrow \gamma\gamma$ decay. We require the presence of a charged track in the CTC for electron identification. We require the ratio of the electromagnetic energy, $E$, of the electron cluster measured in the calorimeter to the electron's momentum, $p$, measured in the central tracking chamber to lie in the range $0.5 < E/p < 2.0$. The distribution of the variable $E/p$ for inclusive electron candidates and for electrons from $W$ decays is shown in Figure 2.4(c). The tail above $E/p > 1$ in $W$ electrons is due to the radiation of photons by the electron as they pass through the material inside the CTC. The radiated photons generally land in the same calorimeter cell as the electron, so $E$ has the same value as the initial electron energy, but $p$ is smaller as it is measured in the CTC after the Bremsstrahlung radiation. This tail is larger in the inclusive electrons because of the presence of electrons from $\pi^0 \rightarrow \gamma\gamma \rightarrow \gamma e^+ e^-$, for which $p$ is the momentum of one electron, but $E$ is close to the energy of the pion.

### 2.4.5 *Track-Shower Matching Variables*

The CTC track pointing to the electron cluster is extrapolated to the CES, and the extrapolated position is compared to the shower position as measured in the CES. The variable $\delta x$ is the separation in the $r$-$\phi$ view between the extrapolated track position and the CES strip cluster position. The variable $\delta z$ is the corresponding separation in the $z$ view. Cutting on these variables reduces the background from overlaps of charged and neutral hadrons. The variables $\delta x$ and $\delta z$ for inclusive electron candidates and for electrons from $W$ decays are shown in Figure 2.4(d,e).

### 2.4.6 *CPR Pulse Height*

The CPR pulse height on the two wires around a track is used to discriminate electrons from hadrons. An electron may begin to shower in the solenoid, while a hadron will leave only a minimum-ionizing pulse. The solenoidal coil thickness is 0.85 $X_0$ at normal incidence. Figure 2.5(b) shows the pulse height shapes for electrons and hadrons.

### 2.4.7 *Electron Track Impact Parameter*

The impact parameter of the electron's track is used to discriminate electrons of long-lived parent particles from those originating from primary vertex of the $p\overline{p}$ collision. The lifetime of bottom quarks is $c\tau \sim 400\,\mu m$, while the impact parameter, $d_0$, resolution is $\sigma_d \sim 40\,\mu m$. The lifetime of the $W$ and $Z^0$ are negligible on this scale. For charged tracks with $P_T > 1\ GeV/c$, the dominant contribution to the impact parameter resolution is the uncertainty in the primary vertex position.

The "signed impact parameter," $D_{sign}$, is defined for a track in the CTC pointing to a jet in the calorimeters. It is defined as:

$$D_{sign} = d_0\left(\frac{\vec{d_0}\cdot\hat{n}_{jet}}{|\vec{d_0}\cdot\hat{n}_{jet}|}\right)$$

where $\vec{d_0}$ is the vector which points from the primary vertex to the point of closest approach of the track to the primary vertex. The unit vector $\hat{n}_{jet}$ points from the primary vertex to the energy centroid of the jet in the calorimeter. A track emanating from the decay vertex of a long-lived parent will have positive $D_{sign}$, whereas a track from the primary vertex will have, on average, zero $D_{sign}$.

The resolution effects which smear the observed $D_{sign}$ spectrum are: the position resolution of the individual hits in the SVX layers; scattering of the electron in the beampipe before reaching the SVX; radiation of photons by the electron as it passes through the material in the tracking volume; and the location uncertainty of the primary vertex. The $D_{sign}$ distribution for electrons from $Z^0 \rightarrow e^+e^-$ decays is shown in Figure 2.6. The observed $\sigma$ agrees well with the dominant contributions of the $\sigma = 32.5\ \mu m$ effect of the primary vertex spread (see Figure 2.7), and the $\sigma = 10.7\ \mu m$ effect of Bremsstrahlung radiation (estimated from a Monte Carlo simulation). The impact parameter significance, $D/\sigma \equiv D_{sign}/\sigma$ is shown for electrons from $Z^0 \rightarrow e^+e^-$ decays in Figure 2.8 (a). Figure 2.8 (b) shows that the events in the tails are, in fact, $Z^0$'s and not background. The non-gaussian $D/\sigma$ tails come from accidental hits in the SVX incorrectly incorporated into the track fit.

### *2.4.8 Event Vertex Measurement*

The position in $z$ of the primary event vertex is measured by the Vertex Tracking Chamber (VTX). The $z$ position of the event is distributed about the nominal interaction point by $\sigma = 26\ cm$ (see Figure 2.9). This spread is an average of many different $\sigma$'s from different physics runs. The spread of the interaction point in $z$ has implications for use of the SVX in physics analyses, since it is larger than the length of the SVX. From studying the tracks from $Z^0$ decays, 61.9 ± 1.3 % of primary vertices are contained within the SVX.

### *2.4.9 Leakage into the Hadronic Calorimeters*

The ratio Had/EM of the energy in the hadronic towers of the electron cluster (Had) to the energy in the electromagnetic towers in the electron cluster (EM) is used to further select good electrons. The electromagnetic calorimeters nearly contain electromagnetic showers, while hadron showers in general deposit energy in both the hadronic and electromagnetic compartments. This quantity is physics-dependent, however, since isolated electrons have less hadronic energy near by them than would electrons produced in association with hadrons (such as electrons from semileptonic $b$ decay, which in general are associated with a jet of hadrons from the decay of the charmed meson). The distribution of Had/EM for inclusive and $W$ electrons is shown in Figure 2.4(f). As expected, the $W$ electrons and the inclusive electrons have a different Had/EM shape.

### *2.4.10 Calorimeter Isolation*

This cut is not an electron identification cut but a topology cut. Electrons from $W$ and $Z^0$ decay are expected to be "isolated." That is, they are not expected to be produced in association with other particles. As mentioned above, electrons from other physics processes are produced associated with jets of other particles nearby in $\eta$-$\phi$ space. We use the "isolation" variable, *Iso*, in order to select electrons not associated with other hadronic activity. The *Iso* variable is defined as:

$$Iso = \frac{E_T^{Cone} - E_T^{Cluster}}{E_T^{Cluster}}$$

where $E_T^{Cone}$ is the sum of the EM and Had transverse energies in all of the towers (including the electron cluster) in a radius of $R = \sqrt{(\Delta\eta)^2 + (\Delta\phi)^2} = 0.4$ centered around the electron cluster, and $E_T^{Cluster}$ is the electromagnetic transverse energy in the electron cluster. The variable *Iso* for inclusive electron candidates and for electrons from $W$ decays is shown in Figure 2.4(g). Again, the shapes are different, the inclusive electrons being less isolated.

## 2.5 Plug Electron Identification

The track-finding efficiency for tracks in the Central Tracking Chamber falls rapidly in the range of $\eta$ covered by the plug calorimeters. Consequently, information from the CTC in the region covered by the plug calorimeters is not used in this analysis. To identify the presence of charged tracks pointing toward the cluster, the occupancy in the vertexing chamber (VTX) octant pointing towards the electron cluster is used (see Figure 2.10). This variable is the ratio of layers in the VTX on which the electron deposits charge divided by the expected number of layers in the VTX to be traversed by the electron, given the electron's trajectory. The ratio

Had/EM is used, as is the isolation variable, *Iso*. The variable $\chi^2_{3x3}$ is used. This variable is a fit of the lateral sharing of energy in the 3 towers in $\eta$ by the 3 towers in $\phi$ around the electron cluster's center to the shape expected from test beam data. The distributions of these variables for $Z^0 \to e^+e^-$ events with a central electron and a plug electron are shown in Figure 2.10.

## 2.6 Forward Electron Identification

Electrons in the regions covered by the forward calorimeters are identified solely by the Had/EM, *Iso*, and VTX Occupancy variables. No other tracking or lateral sharing variables are used. The distributions of these variables for $Z^0 \to e^+e^-$ events with a central electron and a forward electron are shown in Figure 2.11.

## 2.7 Central Electron Trigger

A three-level multipurpose trigger[22] is used to select $p\bar{p}$ events for analysis. The first two levels are programmable hardware triggers, while Level 3 is a software trigger. This section describes the trigger selection for central electrons.

In the Level 1 trigger, energies in physical calorimeter towers of 0.1 × 15° in $\eta$-$\phi$ space are first summed into 0.2 × 15° trigger towers. One trigger tower is required to satisfy $E_T > 7$ *GeV*. It also requires a coincidence of hits in the two BBC's. As shown in Figure 2.12, the efficiency of this trigger for fiducial electrons is 99.2 ± 0.1 % for electrons with $E_T > 10$ *GeV*.

Level 2 performs a cluster search and matches clusters to CTC tracks. EM trigger towers with $E_T > 9$ *GeV* are cluster seeds. Adjacent EM towers are then added to the cluster if they have $E_T > 7$ *GeV*. A cut of (EM+Had)/EM < 1.125 is imposed on electron candidate clusters. A hardware track processor[23] ("Central Fast Tracker," or CFT) searches for tracks in the $r$-$\phi$ plane in the CTC. For the electron trigger, a track of $P_T > 9.2$ *GeV/c* is required to point to the electromagnetic cluster. As shown in Figure 2.12, the Level 2 efficiency is flat vs. $E_T$ in the region of our concern (the threshold is at 9 *GeV*). The inefficiency of this trigger for $W$ and $Z^0$ electrons is dominated by the CFT track reconstruction. This efficiency decreases at large $|\eta|$, as shown in Figure 2.13. The overall efficiency of this trigger for $W$ and $Z^0$ electrons in the fiducial volume was 91.5 ± 0.3 % for this run.

In the Level 3 electron trigger, an electron cluster is required with $E_T > 18$ $GeV$. A three-dimensional track with $P_T > 13$ $GeV/c$ is required to point to the electron cluster. The cuts $Lshr < 0.2$, $|\delta x| < 3$ $cm$, and $|\delta z| < 5$ $cm$ are imposed. For this run, the average Level 3 trigger efficiency for electrons in the fiducial volume is 98.2 ± 0.1 %.

In addition to the electron triggers described above, a set of backup triggers were implemented which select $W \rightarrow e\nu$ events based not on the electron, but on the neutrino, or $\not{E}_T$ (see Section 2.8). These backup triggers require the presence of a neutrino, or $\not{E}_T$, greater than 25 $GeV$, and either a calorimeter cluster or a high-$P_T$ track. These triggers are used to study the efficiency of the electron identification cuts in the trigger.

## 2.8 Neutrino Identification

The calorimeter response to the total activity in the event determines the resolution on the measurement of neutrino $P_T$, which is inferred by invoking momentum conservation. A non-interacting neutrino in our detector is detected by the presence of a large transverse momentum imbalance ("missing $E_T$," or $\not{E}_T$). The missing $E_T$ is calculated from

$$\not{E}_T = |(-1) \times \Sigma \vec{E}_T^{\,i}|$$

where $\vec{E}_T^{\,i}$ is a vector whose magnitude is the transverse energy in a calorimeter tower and whose direction points from the event vertex to the center of the calorimeter tower. The sum is performed within the region $|\eta| < 3.6$.

Events with perfect momentum balance and no resolution effects would have $\not{E}_T = 0$. The smearing about 0 on each component ($x$ and $y$) of $\not{E}_T$ is gaussian and grows with the $\Sigma E_T$ in the calorimeter, as is shown in the minimum bias trigger sample of Figure 2.14. Minimum bias triggers require only a coincidence of hits in both the forward and backward BBC's to signal the presence of an inelastic event. No requirements of the calorimeters are made. The $\Sigma E_T$ is the scalar sum of $E_T$ over all towers in the calorimeter with $|\eta| < 3.6$. At the $\Sigma E_T$ typical of $W$ events, the resolution on $\not{E}_T$ is on the order of 3 $GeV$, while the neutrino $P_T$ is of order 20 - 40 $GeV$. The $\not{E}_T$ significance, $S \equiv \not{E}_T/\sqrt{\Sigma E_T}$, is a measure of how many standard deviations away from zero is the $\not{E}_T$ in a particular event. Figure 2.15 shows $S$ for minimum bias events and for the $W$ candidate events in our sample.

# 3. Inclusive Electron Sample

Inclusive high-$P_T$ electrons are produced in decays of the electroweak bosons, such as $W \to e\nu$, $Z^0 \to e^+e^-$, or $Z^0 \to \tau^+\tau^-$ and $W \to \tau\nu$, where one of the $\tau$'s decays to an electron. High-$P_T$ electrons are also produced in $QCD$ processes, where the electron is embedded in a high-$P_T$ jet of hadrons. The processes that can produce an electron cluster in hadronic jets are (1) electrons which come in $e^+e^-$ pairs, either from photon conversions or Dalitz decays; (2) semileptonic decays of heavy quarks, $b \to ce\nu$ or $c \to se\nu$, and (3) hadron showers ("fakes") that pass our electron identification cuts. The hadrons which pass our electron identification cuts are predominantly overlaps of $\pi^\pm$ and $\pi^0$ showers and pion charge exchange, $\pi^\pm + N \to \pi^0 + N$, which can occur in the calorimeters. This section describes the selection of a sample of inclusive electrons and of three sub-samples: a sample of electrons from $W$ decays, a sample from $Z^0$ decays, and a sample of non-$W/Z^0$ electrons. The non-$W/Z^0$ sample is used as a control sample to study the $W$ backgrounds from hadron jets. Sections 4, 5, and 6 will describe these samples further and discuss the cross-contamination between them.

Candidate events for $W \to e\nu$ and $Z^0 \to e^+e^-$ decays are selected from a common sample of inclusive high-$P_T$ electrons located in the central detector region which pass tight cuts. Requiring tight cuts on the central electron in $W$ and $Z^0$ decay serves three purposes. First, the well-understood central region has added information from the tracking and the strip chambers that can be used to suppress backgrounds from other physics processes. Second, the tight cuts on the central electron allow us to place loose, highly efficient cuts on the second lepton (the neutrino in the case of $W$ decays and the second electron in the case of $Z^0$ decays). Third, and perhaps most importantly, selecting both $W$ and $Z^0$ candidate events from a common sample of inclusive electrons cancels several systematic uncertainties in the ratio of the $W$ and $Z^0$ cross sections.

## 3.1 Central Electron Selection

The selection criteria for a high-$P_T$, central, tight electron are listed in Table 3.1. In addition, we define a tight, *isolated* central electron as one which passes the cuts listed in Table 3.1 and also has $Iso < 0.1$ (see Section 2.4.10). $Iso$ is not an identification variable, but an event topology cut. $W$ and $Z^0$ electrons are expected to be isolated, but electrons from other physics processes may not be. A total of 50861 events pass the tight electron event selection criteria in an exposure of 19.6 $pb^{-1}$. A total of 30349 of these electrons pass the tight, isolated electron event cuts. The $E_T$ spectra of the tight electrons and the isolated tight electrons are shown in Figure 3.1. A peak at 40 $GeV$ from $W$ and $Z^0$ decays is already apparent.

**Table 3.1: Inclusive Central Electron Cuts**

| | | |
|---|---|---|
| $E_T$ | $>$ | $20\ GeV$ |
| $0.5$ | $<$ | $E/p < 2.0$ |
| $Lshr$ | $<$ | $0.2$ |
| $\chi^2_{strip}$ | $<$ | $10.0$ |
| $\lvert\delta x\rvert$ | $<$ | $1.5\ cm$ |
| $\lvert\delta z\rvert$ | $<$ | $3.0\ cm$ |
| $\frac{\text{Had}}{\text{EM}}$ | $<$ | $0.045 + 0.055\left(\frac{E\ (GeV)}{100}\right)$ |
| $\lvert Z_{vertex}\rvert$ | $<$ | $60\ cm$ |
| Electron triggers the event | | |

## 3.2 $Z^0$ Sample Selection

$Z^0$ candidates are selected from the inclusive electron sample by requiring that the tight central electron be isolated and also requiring a second isolated electron which passes loose selection criteria. The loose cuts on the second electron are listed in Table 3.2.

Table 3.2: $Z^0$ Selection Cuts

| | | |
|---|---|---|
| -One tight, isolated central Electron | | |
| -Second Electron passing loose cuts: | | |
| Central: | Plug: | Forward: |
| $E_T > 20\ GeV$ | $E_T > 15\ GeV$ | |
| Had/EM < 0.1 | Had/EM < 0.1 | $E_T > 10\ GeV$ |
| *Iso* < 0.1 | *Iso* < 0.1 | Had/EM < 0.1 |
| Opposite sign charged track | $\chi^2_{3\times3} < 3.0$ | *Iso* < 0.1 |
| $E/p < 2.0$ | | |
| $66\ GeV/c^2 < M_{(ee)} < 116\ GeV/c^2$ | | |

Figure 3.2 shows the invariant mass distribution of electron pair candidates before and after the cuts of Table 3.2 are imposed. The electron pairs before the cuts of Table 3.2 are imposed consist of one tight isolated central electron (Table 3.1) and a second cluster as defined in Section 2.2. The dominant background suppression comes from the kinematic cuts on the second electron. We observe 1312 events which fall in the 66 - 116 $GeV/c^2$ mass range. Figure 3.3 shows the distribution in $\eta$ of the second lepton of the 1312 $Z^0$ candidates. Table 3.3 shows that the distribution in $\eta$ of the second lepton corresponds well to expectations from the Monte Carlo when the different total detector efficiencies and backgrounds are taken into account. The Monte Carlo is normalized to the $Z^0$ signal.

Table 3.3: $Z^0$ Yield in Different Detector Regions

| Detector in which 2nd Lepton Falls | $Z^0$ Candidate Yield | $Z^0$ Background (see Sect. 6) | $Z^0$ Signal (Yield - Background) | Monte Carlo Expectation (see Sect. 7) |
|---|---|---|---|---|
| Central | 529 | 1 ± 1 | 528 ± 23 | 535 ± 13 |
| Plug | 640 | 14 ± 14 | 626 ± 29 | 618 ± 13 |
| Forward | 143 | 6 ± 3 | 137 ± 12 | 138 ± 8 |

## 3.3 *W* Sample Selection

To select *W*'s from the inclusive electron sample, we (a) require a tight, isolated central electron in the event; (b) require $\not{E}_T > 20\ GeV$; (c) reject $Z^0$ decays by asking that the event does not posses a second, isolated, electromagnetic cluster which forms a mass with the first electron in the 66 - 116 $GeV/c^2$ range. Figure 3.4 shows the *Iso* of the electron in the event *vs.* the $\not{E}_T$ in the event. The *W*'s appear as a cluster at low *Iso*, high $\not{E}_T$. The $\not{E}_T$ spectrum of the isolated ($Iso < 0.1$) and non-isolated ($Iso > 0.3$) tight inclusive electrons is shown in Figure 3.5. A total of 13796 events have $\not{E}_T > 20$ *GeV* and pass our $Z^0$ rejection cuts. Figure 3.6 shows the distribution in $\eta$ of the electrons from the *W* candidates. The $Z^0$ removal cut removes only 41 events, because the missing $E_T$ requirement strongly suppresses the $Z^0$'s.

## 3.4 Non-*W*/$Z^0$ Electron Sample Selection

The *W* and $Z^0$ samples selected above are contaminated by electrons from other physics processes. The backgrounds of electrons from hadron jets are particularly important to understand. This section describes the selection of a control sample of those electrons from hadron jets. In Section 4 we examine the make-up of this sample and determine the fractions, $f_{conv}$, $f_b$, and $f_{fake}$ of electrons in jets that come from conversions, heavy quarks, and fake electron clusters. The techniques used in Section 4 are then employed in Section 5 to determine the contamination of the $\not{E}_T > 20$ *GeV* sample (*W* sample) from these hadronic processes.

From the inclusive electron sample of 50861 events, events which have a second cluster which passes cuts of Had/EM $< 0.1$ and $Iso < 0.1$ are removed in order to reject electrons from $Z^0 \to e^+e^-$ and Drell-Yan pair production. Approximately 4600 events are removed by this cut. Events which have $\not{E}_T > 10$ *GeV* are rejected in order to remove electrons from $W \to e\nu$ or $W \to \tau\nu \to e\nu\nu\nu$. 21637 events survive this cut. The contamination of this sample from $W \to e\nu$, $Z^0 \to e^+e^-$, $W \to \tau\nu$ or $Z^0 \to \tau^+\tau^-$ is estimated[24] to be 1.0 ± 0.2 %. Finally, we require a hadronic jet with $E_T > 10$ *GeV* and electromagnetic fraction less than 0.8, which reduces the fraction of electrons from weak boson decays to 0.4 ± 0.1 % of the sample. The 17805 electrons passing all of these cuts are used as our control sample of non-*W*/$Z^0$ electrons.

# 4. Non-$W/Z^0$ Electron Sample

Electrons from $W$ and $Z^0$ decay account for only a fraction of the high-$P_T$ inclusive electrons observed in our detector. In this section we investigate the sources of high-$P_T$ electrons from *QCD* processes that create electrons embedded in hadron jets. This discussion will be of particular use in Section 5, in which we discuss the backgrounds to the $W$ candidates. As mentioned in Section 3, we anticipate that electrons in hadron jets fall into three categories: 1) electrons which come in $e^+e^-$ pairs, either from photon conversions or Dalitz decays; 2) electrons from heavy quark decay; and 3) hadrons that fake electrons. Hereafter, electron pairs from photon conversions and from Dalitz decays will be referred to collectively as "conversions."

In this section we use the 17805 electrons in the non-$W/Z^0$ electron sample to estimate the fraction, $f_{conv}$, of electrons in hadron jets that originate from photon conversions. We also estimate the fraction, $f_b$, of non-$W/Z^0$ electrons from heavy quark decay, and the fraction, $f_{fake}$, of non-$W/Z^0$ electrons that are not electrons but clusters of hadrons. Finally, we estimate how many electrons in the inclusive electron sample (see Section 3.1) come from these three *QCD* processes.

## 4.1 Estimate of the Conversion Electron Fraction

Electrons from photon conversions are identified by searching for a second, oppositely-signed charged track near the electron track which extrapolates to a common tangent point. We flag as conversions the electrons which have a second track nearby in the CTC passing the following cuts: $|\delta(r\text{-}\phi)| < 0.2$ *cm*; $|\delta(\cot\theta)| < 0.06$. The first cut is on the separation in the $r$-$\phi$ view[19] between the two tracks at their tangent point. This variable is given a positive sign if the two circles of the tracks in the $r$-$\phi$ view do not overlap, and a negative sign otherwise. The second cut is on the difference in $\cot\theta$ between the two tracks.[19] Figure 4.1 shows these variables for track pair candidates in the non-$W/Z^0$ electron sample.

Some hadron tracks are falsely flagged as conversion partners by the $\delta(r\text{-}\phi)$ and $\delta(\cot\theta)$ cuts. In Figure 4.2 we show the pulse height left in the CES by the partner track to the electron track for those pairs in Figure 4.1 which pass the $\delta(\cot\theta)$ and $\delta(r\text{-}\phi)$ cuts. Also shown is the expected shape for electrons, which is derived from a pure sample of conversion pairs which was selected based on having a conversion radius consistent with the outer wall of the VTX, at $r \sim 27$ cm. We estimate that 89 ± 2 % of the track pairs selected with the $\delta(\cot\theta)$ and $\delta(r\text{-}\phi)$ cuts are truly conversion pairs. Correcting for the backgrounds and the conversion finding efficiency, we find that $f_{conv} = 41.5 \pm 2.2$ % is the fraction of the non-$W/Z^0$ electron sample that are conversion pairs or Dalitz decays. The conversion-finding efficiency has two-components: the efficiency to find the partner track, and the efficiency for the track pair, if found, to pass the $\delta(\cot\theta)$ and $\delta(r\text{-}\phi)$ cuts. Both of these efficiencies are estimated with a sample of conversions that occur at $R \sim 27$ $cm$ from the beamline.[16]

## 4.2 Estimate of the *b* Electron Fraction

One signature characteristic of a *b* quark is its long lifetime. Using the impact parameter significance, $D/\sigma$, of electrons in the Silicon Vertex Detector (SVX), an estimate is made of the number of electrons in the non-$W/Z^0$ sample from *b* decay. The impact parameter significance distribution of all electrons in the non-$W/Z^0$ sample is fit to a sum of shapes from *b*'s, conversions, and fake electrons. In this fit, the conversion fraction is set to $f_{conv} = 41.5\%$ from Section 4.1, so that the *b* and fake fractions are determined. The impact parameter shape for fake electrons is assumed to be the same as that of $Z^0$ electrons, since they are presumably from light quark jets and have zero lifetime. The impact parameter distribution for the conversions is derived from the conversion sample of Section 4.1, with the additional requirement that the partner track leave at least 2000 Counts / $(GeV/c)$ in the CES (see Figure 4.2). The additional requirement on the pulseheight is used to obtain a more pure conversion sample.

In order to obtain the $D/\sigma$ shape for *b* electrons, we exploit the fact that *b*'s in $p\bar{p}$ collisions are produced in $b\bar{b}$ pairs, so that we select a data sample of semileptonically-decaying $b$ ($\bar{b}$) quarks by tagging the $\bar{b}$ ($b$) jet in the event with a *b*-tagging algorithm.[25] Selecting *b* events using only the away jet to identify the *b* electron applies negligible bias to the signed impact parameter distribution for *b* electrons.

In the $b$-tagging algorithm, a probability is formed per jet that the jet comes from the primary vertex of the event. Jets with low probability are likely to come from heavy quarks. This probability utilizes the signed impact parameters of the tracks in the jet, and is the probability that the impact parameters of the tracks are consistent with zero within the SVX resolution. The probability distribution for all jets (besides the electron jet) in the non-$W/Z^0$ electron sample is shown in Figure 4.3. Heavy quark jets are identified as those jets with Jet Probability $< 0.02$. From the flat component under the probability peak in Figure 4.3 backgrounds in this sample from false tags of the away jet are expected to be ~ 10 %. The $b$ electron $D/\sigma$ shape is estimated from these tagged events.

Figure 4.4 shows the $D/\sigma$ distribution for the electrons in the non-$W/Z^0$ sample that go through the SVX. We fit the tails of the $D/\sigma$ distribution to the sum of $b$, fake, and conversion shapes, with the conversion fraction fixed. We find:

$$f_{conv} = 41.5 \pm 2.2 \ \%$$
$$f_b = 31.5 \pm 3.7 \ \%$$
$$f_{fake} = 27.0 \pm 4.4 \ \%$$

The dominant uncertainty on these fractions comes from the small statistics available to estimate the $b$ electron shape.

## 4.3 Estimate of Fake Electron Fraction

This section provides a second, independent estimate of the fraction of the non-$W/Z^0$ electrons that are fake electrons. The fraction $f_{fake}$ of Section 4.2 is the fraction of the electrons consistent with coming from the primary vertex, which we interpreted as misidentified hadrons from light quark jets. Hadrons may also be identfied using the Central Pre-Radiator, since in general they do not begin to shower in the solenoidal coil, while electrons do. Plotted in Figure 4.5 is the CPR charge for all electrons in the non-$W/Z^0$ sample. Also shown is the CPR shape for electrons (obtained from electrons in $Z^0 \to e^+e^-$ decay) and hadrons (obtained from jets in $W/Z^0$ + jet events). With the conversion electron fraction fixed (see Section 4.1) we fit the distribtution to the sum of the two shapes to find:

$$f_{conv} = 41.5 \pm 2.2 \ \%$$
$$f_b = 31.9 \pm 4.0 \ \%$$
$$f_{fake} = 26.6 \pm 4.1 \ \%$$

The agreement with Section 4.3 is good, since the two estimates are independent: in one method the zero lifetime of hadrons is used to differentiate them from heavy quark electrons, and in the other method the longitudinal shower development of electrons and hadrons is used.

### 4.4 Number of Inclusive Electrons from *QCD* Jets

The non-$W/Z^0$ electron sample is postulated to originate from *QCD* processes producing hadron jets. One can ask the simple question what fraction of events in the overall inclusive electron sample (see Section 3.1) come from such *QCD* processes? This question is not crucial to this analysis, but is interesting.

Noting that electrons with $Iso > 0.3$ are predominantly from *QCD* processes, we may use Figure 3.5(a) to estimate a 58% efficiency of the $\not{E}_T < 10$ *GeV* cut used to make the non-$W/Z^0$ sample for hadron jets. We then scale the 21637 hadron jet events of Section 3.4 up by this efficiency to obtain that approximately 37000 ± 4000, or (73 ± 7) %, of the 50861 inclusive electrons are from hadron jets. The number 21637, it was noted, has a ~ 1% background from $W/Z^0$ decay, but this can be neglected for our present purposes.

Figure 4.6 shows the $E_T$ spectrum of electrons in the inclusive electron sample, along with the spectrum from the non-$W/Z^0$ electron sample (scaled up to 37000 events), and the Monte Carlo expectation for electrons from $W/Z^0$ decays (normalized using the number of $W$ and $Z^0$ candidates). The events at the very highest $E_T$ are mostly dijets, with one $Z^0$ event. The apparent excess of events above 80 *GeV* is due to the truncation of the sample used to obtain the hadron dijet spectrum: the very highest $E_T$ dijets will have some $\not{E}_T$ due to mismeasurement, and the dijet shape comes from the $\not{E}_T < 10$ *GeV* sample. The conclusion from this study is that the inclusive electron data sample is adequately described by three sources: *QCD* hadron jets, $W$ decays, and $Z^0$ decays.

# 5. *W* Candidate Sample

*W* candidates are selected with a signature of an isolated electron and $\not{E}_T$. This signature, however, can also be mimicked by other physics processes. The physics processes described in Section 4 can lead to backgrounds to the *W* signal if the hadron jet containing the electron fluctuates so that the electron is isolated in the calorimeters and if the other jet is mismeasured or falls into an uninstrumented region of the detector, creating $\not{E}_T$. Similarly, $Z^0 \to e^+e^-$ or $Z^0 \to \tau^+\tau^- \to e^\pm \nu\nu X$ decays can be misidentified as *W*'s if one electron is detected and the other lepton falls in an uninstrumented region or the neutrinos from $\tau$ decays are sufficiently energetic. This section discusses the backgrounds to the *W* signal from these processes.

## 5.1 *W* Candidate Selection

The *W* candidate selection is described in Section 3.3, but is briefly summarized here. To select *W*'s we (a) require a tight, isolated central electron in the event; (b) require $\not{E}_T > 20$ *GeV*; (c) reject events with second, isolated, electromagnetic clusters which forms a mass with the first electron in the 66 - 116 $GeV/c^2$ range. A total of 13796 events have $\not{E}_T > 20$ *GeV* and fail our $Z^0$ cuts. As shown in Figure 3.5, the missing transverse energy of the isolated electrons shows the characteristic peak, while the non-isolated electrons pile up at threshold. The problem now is to calculate the background under the peak in Figure 3.5(b) with missing $E_T > 20$ *GeV*.

## 5.2 Background from Hadron Jets

The background from hadron jets is estimated by extrapolating the Isolation variable for the electron from a region away from the *W* signal into the *W* signal region. We identify four regions within the plot of *Iso vs.* missing $E_T$ in Figure 3.4:

1) Isolation < 0.1 and $\not{E}_T < 10$ *GeV*, at least one other jet
2) Isolation > 0.3 and $\not{E}_T < 10$ *GeV*, at least one other jet
3) Isolation > 0.3 and $\not{E}_T > 20$ *GeV*
4) Isolation < 0.1 and $\not{E}_T > 20$ *GeV*

(Region 4 is the $W$ signal region). The requirement of one other jet in Regions 1) and 2) is that one jet besides the jet containing the electron exists in the event. We find the $W$ background from the equation:

$$\frac{W\ \text{Background}}{\#\ \text{Events in Region 3}} = \frac{\#\ \text{Events in Region 1}}{\#\ \text{Events in Region 2}}$$

The motivation of the method is that electrons from hadron jets are generally produced embedded in a jet of other particles while electrons from $W$ and $Z^0$ decay are isolated. The equation above amounts to using the electrons with $\not\!\!E_T < 10\ GeV$ in Figure 5.1(a) to determine the *Iso* shape of electrons in hadron jets and then normalizing to the $Iso > 0.3$ tail at $\not\!\!E_T > 20\ GeV$ (Figure 5.1(b)).

The requirement of at least one jet besides the electron jet in Regions 1) and 2) is intended to account for the fact that the Isolation of the electron on the one side of the *QCD* jet events is correlated with the magnitude of the jet $E_T$ on the other side of the event, as is shown in Figure 5.2. In the case of the dijet events which fake a $W$, the mismeasured jet $E_T$ must be large in order to create a large $\not\!\!E_T$. Because the actual value of the mismeasured jet's $E_T$ is unknown, we average the the value of $r \equiv (Iso < 0.1)/(Iso > 0.3)$ from two different subsets of the *QCD* ($\not\!\!E_T < 10\ GeV$) sample which have different opposing jet $E_T$'s:

Control Sample 1: Events with a Jet $> 10\ GeV$ and EM fraction $< 0.8$
Control Sample 2: Events with a Jet $> 20\ GeV$ and EM fraction $< 0.8$
(both have $\not\!\!E_T < 10\ GeV$)

Control Sample 2 is a subset of Control Sample 1. The control samples give $r = 1.5$ (Control Sample 1) and $r = 2.0$ (Control Sample 2). We average the results, obtaining $\langle r \rangle = 1.8 \pm 0.3$, to account for any systematic difference between the samples.

The hadron jet background is calculated as follows. There are 499 events in Region 3, so multiplying by $\langle r \rangle$ gives: $W$ Background $= \langle r \rangle \cdot 499 = 898 \pm 155$ events. Given the 13796 $W$ candidates, this is a 6.5% background contribution from electrons from hadron jets. Note in Figure 3.5 the $\not\!\!E_T$ shape of the events in Region 3. Most of the $W$ background piles up at the threshold of our missing $E_T$ cut.

## 5.3 Cross-Check of Hadron Jet Background

We check the method described in Section 5.2 by estimating the background from individual jet contributions separately - photon conversions, *b* decays, and fake electrons from hadron showers - and then adding them up to find the total jet background to the *W*'s. This decomposition was applied to the non-$W/Z^0$ electron sample in Section 4. The non-$W/Z^0$ electron sample was selected from the total by requiring each event to have a jet with $E_T > 10$ *GeV*and$\not{E}_T < 10$ *GeV*. No isolation cut was applied to these data, because it would have greatly reduced the sample size, leaving too few events for further study. In order to compare the *W*'s to the background, the *Iso* cut is removed from the *W* sample, which adds 1433 events to the 13796 events with $\not{E}_T > 20$ *GeV* and *Iso* $< 0.1$, resulting in 15229 events with $\not{E}_T > 20$ *GeV* alone. About 2/3 of these extra events are background, and 1/3 is signal: Table 8.1 gives the efficiency of the *Iso* cut of 97%, hence one expects that of the addition 1433 events added to the *W* sample, $0.03 \times 14000 = 420$ are really *W*'s.

To estimate the conversion contamination of the $\not{E}_T > 20$ *GeV* region, we identify conversions by searching for the partner track to the electron using the $\delta(r\text{-}\phi)$ and $\delta(\cot\theta)$ cuts from Section 4.1. Using the efficiency and correcting for the overefficiency of the conversion-finding cuts, we estimate that there are 910 ± 90 events with $\not{E}_T > 20$ *GeV* that are conversion pairs. The $\not{E}_T$ of the flagged conversions is shown in Figure 5.3.

To estimate the contamination to the $\not{E}_T > 20$ *GeV* region from *b* electrons we employ the impact parameter method described in Section 4.2. In Figure 5.4(a) is plotted the signed impact parameter significance for the electrons with $\not{E}_T > 20$ *GeV*. In Figure 5.4(b), we show the $\not{E}_T$ distribution of the electrons with $|D/\sigma| > 2$. There is a bump at 40 *GeV*, which indicates that some *W* electrons have a large impact parameter significance, simply due to resolution effects. Using electrons from $Z^0 \to e^+e^-$ decays to estimate number of *W*'s in the $D/\sigma$ tails due to resolution effects, we superimpose the expected $\not{E}_T$ curve for *W* electrons. We find that 850 ± 360 events with $\not{E}_T > 20$ *GeV* are from heavy quarks.

To estimate the contamination to the $\not{E}_T > 20$ *GeV* region from misidentified hadrons, we use the charge deposited in the CPR, shown in Figure 5.5. Also shown is the expected shape for good electrons and for hadrons. We estimate that there are 580 ± 370 of the 15229 events with $\not{E}_T > 20$ *GeV* which are really hadron fakes.

Adding these numbers, there are 910 ± 90 conversions, 850 ± 360 *b* electrons, and 580 ± 370 hadron fakes for a grand total of 2340 ± 530 hadron jet background events obtained by application of the analyses described in Section 4 applied to the *W* sample itself. Within the quoted uncertainties, this number is consistent with the *Iso* < 0.1 number of 898 ± 155 background events quoted in Section 5.2, plus an extra 1433 - 420 ≈ 1000 events background from relaxing the *Iso* cut.

An independent method of estimating the total jet background in the $\not{E}_T > 20$ *GeV* sample with the *Iso* cut relaxed, that is to check that the extra 1000 added background events are reasonable, is to use the *Iso vs.* $\not{E}_T$ extrapolation technique of Section 5.2 again. First, we define $R \equiv$ (all *Iso* electrons)/(*Iso* > 0.3) for hadron jet electrons in the $\not{E}_T < 10$ *GeV* sample. This ratio, averaging over the two Control Samples 1 and 2, is $\langle R \rangle = 4.2 \pm 0.7$. Multiplying this ratio by the number of events in Region 3 obtained in Section 5.2 gives 2100 ± 350 events. Within the uncertainties, this direct extrapolation result and the 2340 ± 530 events obtained by adding up the three components are consistent. This analysis supports the 898 ± 155 background number with *Iso* < 0.1, which will be subtracted from the *W* sample to calculate the $W/Z^0$ cross section ratio.

## 5.4 Background from $Z^0 \rightarrow e^+e^-$

### 5.4.1 $Z^0 \rightarrow e^+e^-$ Background Estimate

We use the ISAJET Monte Carlo program and a detailed detector simulation to determine the background to the *W*'s from $Z^0 \rightarrow e^+e^-$ decays that mimic the *W* signature. We find that 18 ± 2 % of all $Z^0 \rightarrow e^+e^-$ decays where the first leg is reconstructed in the Central region will mimic *W*'s. We normalize this rate to the observed number of $Z^0$ candidates, which avoids the systematic uncertainties of normalizing to the measured[26] cross section times branching ratio $\sigma \cdot B(p\overline{p} \rightarrow Z^0 \rightarrow e^+e^-)$ at $\sqrt{s} = 1800$ *GeV*. The background to the *W*'s from $Z^0 \rightarrow e^+e^-$ decays is 281 ± 32 events.

### 5.4.2 $Z^0 \rightarrow e^+e^-$ *Background Cross-Check*

The ISAJET Monte Carlo program is used to determine several of the *W* backgrounds, so its performance is checked using $Z^0 \rightarrow e^+e^-$ decays. We can recover some of the 18% of $Z^0 \rightarrow e^+e^-$ decays by looking for the charged track of the second electron in the Central Tracking Chamber. In the central region, the second electron is typically not observed in the calorimeter because it goes through a $\phi$ crack or the $\theta = 90°$ crack or the chimney module. Its charged track is nonetheless detected with 99.7% efficiency in the CTC if it passes through all 8 superlayers. ISAJET studies indicate that $81 \pm 12$ events of the 281 $Z^0$'s that fake *W*'s should be detectable as having a track with $P_T > 10$ *GeV/c*, even though the calorimeter cluster is not observed.

In our *W* sample, we search for second, isolated tracks in the CTC which come from the same primary vertex as the "*W* electron" and which have $P_T > 10$ *GeV/c*. If the track extrapolates to a region in the calorimeter where energy is deposited, the electromagnetic fraction is required to be > 0.8. Approximately 3800 events in the *W* sample are observed to have a high-$P_T$ track, and 904 of these come from the same primary vertex, are isolated, and point to possible electromagnetic energy. Figure 5.6 shows the electron + track invariant mass of the 3800 and 904 events. Also shown is the expected shape from ISAJET. In 213 events, there is $\not{E}_T > 20$ *GeV*, and in 83 of the 213 events no second electron cluster (as defined in Section 2.2) is observed. This compares well to the $81 \pm 12$ events predicted by ISAJET. Figure 5.7 shows that when $\not{E}_T > 20$ *GeV*, the second track tends to point to a calorimeter $\phi$ crack.

## 5.5 Background from $Z^0 \rightarrow \tau^+\tau^-$

The process $Z^0 \rightarrow \tau^+\tau^-$ can mimic the *W* signature if one $\tau$ decays to an electron. Using ISAJET and a detector simulation and normalizing to the observed $Z^0 \rightarrow e^+e^-$ yield, we find the background from this process to be $48 \pm 7$ events.

## 5.6 Background from $W \rightarrow \tau\nu$

The process of *W* bosons decaying to $\tau\nu$, where the $\tau$ then decays leptonically to an electron, can also produce a high $P_T$ electron in the central region with large $\not{E}_T$.

We similarly use ISAJET to estimate the acceptance for this process but normalize instead to the ISAJET $W \to e\nu$ acceptance and the observed number of $W \to e\nu$ events. We find the background from $W \to \tau\nu$ to be 473 ± 29 events. This normalization avoids the uncertainties introduced by using the luminosity and the previously measured $W$ cross section.[26]

### 5.7 Background from Heavy Top Quark

The background of real $W$'s produced from a heavy top quark is considered. Direct searches[1] for the top quark have to date have given evidence for its existence, but we take this background to be 0, with an error given by the number of events expected for a 130 $GeV/c^2$ top, which is the 95% confidence level limit[1,2] on its mass. This prescription for the top quark background leads to the most conservative limit on new decay modes obtained with the $W$ leptonic branching ratio extracted from the $W/Z^0$ cross section ratio. Using the ISAJET Monte Carlo, we find the expected background from a heavy top quark is $0^{+40}_{-0}$ events. While a 130 $GeV/c^2$ top would contribute 40 events background, a 150 $GeV/c^2$ top quark would lead to an expected background of 19 events and a 175 $GeV/c^2$ top quark[2] would lead to 9 events background.

### 5.8 Summary of $W$ Signal, Backgrounds.

In Figures 5.8, 5.9, and 5.10 we plot the electron $E_T$, the $\not{E}_T$, and the transverse mass of the $W$ candidates, along with the background estimates and the expectations of the Monte Carlo described in Section 7. The agreement of the shapes of all of these distributions gives further confidence in the background estimates presented here. The measured $W$ $P_T$ distribution which is input to the Monte Carlo is not sufficiently accurate to provide a precise Monte Carlo prediction for the electron $E_T$ distribution, as reflected in Figure 5.8. The $\not{E}_T$ is in principle sensitive to the boson $P_T$ as well, but the neutrino resolution is poor enough so that the shape mismatch is less noticeable. The transverse mass distribution is insensitive to the boson $P_T$.

# 6. $Z^0$ Candidate Sample

The signature used to select $Z^0 \rightarrow e^+e^-$ candidates is an isolated, tight central electron plus a second, loosely-selected electromagnetic cluster. Very few processes mimic the signature of two high-$P_T$ electron clusters. Thus, while the $W \rightarrow e\nu$ candidate sample had backgrounds from other processes totaling approximately 12% of the observed candidates, the backgrounds to the $Z^0$ candidates are observed total less than 2%.

## 6.1 $Z^0$ Candidate Selection

$Z^0$ candidates are selected from the inclusive electron sample by requiring an isolated tight central electron and a second isolated electron which passes loose selection criteria. The cuts on the tight electron are summarized in Table 3.1 and for the second electron in Table 3.2. Figure 3.2 shows the invariant mass spectrum of electron pairs passing these cuts. We observe 1312 events which fall in the 66 - 116 $GeV/c^2$ mass range.

## 6.2 Background from Hadron Jets

Hadron jet events can fake the signature of a $Z^0$ decay into electrons if two of the jets fluctuate in such a way as to fake electrons. As with the hadron jet background to $W$'s, we attempt to measure the hadron jet background to $Z^0$'s from the data by extrapolating the Isolation distribution of the electrons. Figure 6.1 shows the electron-positron invariant mass *vs.* the Isolation of the second electron, where the isolation cut of Table 3.2 has been removed. While there is an unambiguous cluster at the $Z^0$ mass and low Isolation, some background events in the $Z^0$ mass window extend as far as $Iso$ = 1.4.

We posit that all events with $Iso > 0.3$ on either leg are background from hadron jets. This assumption is equivalent to assuming that an Isolation cut of 0.3 is 100% efficient for electrons from $Z^0$'s. This is quite reasonable, since in Figure 2.4(g) none of the 9000 $W$ electrons have $Iso > 0.14$. We divide the electron pairs into four regions:

1) Events with $Iso_1 < 0.1$ and $Iso_2 < 0.1$
2) Events with $Iso_1 < 0.1$ and $Iso_2 > 0.3$
3) Events with $Iso_1 > 0.3$ and $Iso_2 < 0.1$
4) Events with $Iso_1 > 0.3$ and $Iso_2 > 0.3$

None of samples 2) - 4) have a $Z^0$ peak. The $Z^0$ background calculated from the equation:

$$\frac{Z^0 \text{ Background}}{\#\text{ Events in Region 2}} = \frac{\#\text{ Events in Region 3}}{\#\text{ Events in Region 4}}$$

We find that there are 20 ± 9 events background to the $Z^0$ candidates due to hadron jets. We find that $0^{+1}_{-0}$ of these come from the central-central $Z^0$'s, whereas the plug region contributes 14 ± 14 events background and the forward region contributes 6 ± 3 events background.

In the central region, the same-sign electrons serve as a cross check of background estimated by the *Iso* extrapolation method. Background would likely have equal numbers of same- and opposite-sign events. This hypothesis is supported by the fact that most non-isolated same-sign pairs have $|\delta x| > 2$, indicating a poor match between the track and the EM shower, as characteristic of overlaps of $\pi^+$ and $\pi^0$ showers, and not *b* electron pairs (*b* electron pairs would have $|\delta x| < 2$, and would be mostly oppositely signed, with only ≈ 30% same-sign). There are 3 central-central same-sign $e^{\pm}e^{\pm}$ pairs in the mass window passing all our cuts, to be compared with the *Iso* estimate of $0^{+1}_{-0}$ central-central background events.

### 6.3 Background from $Z^0 \rightarrow \tau^+\tau^-$

The production of $Z^0 \rightarrow \tau^+\tau^-$ can fake $Z^0 \rightarrow e^+e^-$ decay if both taus decay via $\tau \rightarrow e\nu\nu$ and if the electrons form an invariant mass in the 66 - 116 $GeV/c^2$ invariant mass range. We use the ISAJET Monte Carlo program and a detector simulation to estimate that the background due to $Z^0 \rightarrow \tau^+\tau^-$ as 1 ± 1 event.

## 6.4 Background from the Drell-Yan Process

We apply a correction to the number of $Z^0$ candidates to account for the fact that some $e^+e^-$ pairs in the 66 - 116 $GeV/c^2$ mass range come from continuum $p\overline{p} \rightarrow \gamma^* \rightarrow e^+e^-$, and not resonant $Z^0$ production. The correction is applied so our result is consistent with theoretical calculations, which typically use only the $Z^0$ amplitude, and not the $\gamma^*$ term or the $Z^0$-$\gamma^*$ interference term. We include in our Monte Carlo described in Section 7 both the $Z^0$ and $\gamma^*$ amplitudes to determine the number of the events in our mass window from continuum Drell-Yan production. This correction also takes into account the effect of the mass window cut, since this is not accounted for in the Monte Carlo results of Section 7. We compute the integrals $I_1 \equiv \int_{66}^{116} |Z^0 + \gamma|^2 dM$ and $I_2 \equiv \int_0^\infty |Z^0|^2 dM$. The number of $Z^0$ candidates must be divided by the number $I_1/I_2$, which we find to be 1.005 ± 0.002.

## 6.5 Comparison of $Z^0$ Signal, Backgrounds:

Finally, in Figure 6.2 we show the invariant mass distribution for the $e^+e^-$ candidates, along with the shape for the $Z^0+\gamma^*$, and the expected hadron jet background shape. The $Z^0+\gamma^*$ signal shape is derived from the Monte Carlo described in Section 7). The background shape is derived from 'dielectrons' in Region 2 described in Section 6.2 above, and is normalized to have 20 events in the 66 - 116 $GeV/c^2$. The signal Monte Carlo is normalized to 1291 events in the 66 - 116 $GeV/c^2$ mass range.

# 7. Acceptances

We use a Monte Carlo program to determine the ratio, $A_W/A_Z$, of the kinematic and geometric acceptances $A_W$ and $A_Z$. The kinematic portion of the acceptance is the efficiency of $W$ and $Z^0$ events to pass our $P_T$ cuts on the leptons, and the geometric portion of the acceptances is the efficiency for the leptons to fall into the parts of the detector accepted as part of our fiducial volume. Note that, because of the requirement of at least one electron in the Central region common to both $W$ and $Z^0$ decays, the problem of determining $A_W/A_Z$ reduces to modeling the difference in the acceptance of the second lepton only, *viz.*, the electron or neutrino.

The Monte Carlo is also used to determine the relative acceptances of the central, plug, and forward detector regions for electrons from $Z^0 \to e^+e^-$ decays. For those $Z^0$'s with at least one electron that falls in the central detector region, we calculate the fractions $F_{cc}$, $F_{cp}$, and $F_{cf}$ of $Z^0$'s where the second electron falls in the central, plug, and forward regions. These fractions will be used in Section 8.

## 7.1 Description of the Monte Carlo

The Monte Carlo program generates $W$'s and $Z^0$'s using the lowest order diagram, $q\overline{q} \to W(Z^0)$. No quark-gluon diagrams or initial-state radiation are considered. The bosons masses are generated according to a relativistic Breit-Wigner distribution. In order to mimic the effects of higher-order diagrams, the bosons are given a $P_T$ according to the measured[27] $W$ $P_T$ distribution in $p\overline{p}$ collisions at $\sqrt{s} = 1.8$ $TeV$. The leptons are propagated to the calorimeter and their momenta are smeared according the nominal detector resolutions. The electrons in our Monte Carlo are required to propagate to a fiducial region of the detector.

The electron resolution in the simulation is $\left(\sigma/E\right)^2 = \frac{(13.5\%)^2}{E\ (GeV)} + \left(2\pm1\%\right)^2$, where the energy-independent term of $\left(2\pm1\right)\%$ represents tower-to-tower variations in the energy scale calibrations and is measured using the observed width of the $Z^0 \to e^+e^-$ resonance. A model is also made for the $\not{E}_T$ resolution. Since the neutrino transverse momentum is inferred from momentum conservation, the $\not{E}_T$

measurement is dominated by the electron, but is also sensitive to the calorimeter response to the hadrons which recoil against the *W*. In this model, we use a parameterization of the smearing on the component of the $\not{E}_T$ parallel and perpendicular to the $P_T$ of the boson as a function of the boson $P_T$ which is obtained from a detailed simulation of the detector. Using the parameters $M_W$= 80.21 $GeV/c^2$, $M_Z$ = 91.18 $GeV/c^2$, and the MRS D-' parton distribution functions,[28] we find $A_W$ = 0.3416 ± 0.0008 and $A_Z$ = 0.4120 ± 0.0008, where the errors are statistical only. Note that, because central-central $Z^0$'s have two chances of having one electron in the central detector region, the $Z^0$ acceptance is higher. The fractions $F_{cc}$, $F_{cp}$, and $F_{cf}$ are found to be 0.372, 0.509, and 0.120, respectively.

## 7.2 Systematic Uncertainties in $A_W/A_Z$

In this section, we investigate the systematic uncertainties due the choice of parton distribution functions (PDF's), the underlying event model, the boson masses, the calorimeter energy scales, the $P_T$ distribution input to the Monte Carlo, and higher order diagrams. For each possible source of systematic uncertainty, we repeat the Monte Carlo calculation with different values for these parameters and take the error to be one half of the spread in the results. As is discussed below, while the individual acceptances are sensitive to variations in these parameters, the ratio is more stable. In the tables which follow, all of the values for *W* and $Z^0$ acceptances have a statistical error of ± 0.0008.

In order to estimate the systematic uncertainty due to the parton distribution functions, we employ different sets of PDF's not excluded by current experimental data. We find a 0.9% uncertainty in $A_W/A_Z$ due to PDF's, as shown in Table 7.1.

**Table 7.1: Acceptances Calculated With Different Parton Distribution Functions**

| PDF | $A_W$ | $A_Z$ | $A_W/A_Z$ |
|---|---|---|---|
| MRS D-' | 0.3416 | 0.4102 | 0.833 |
| MRS D0' | 0.3458 | 0.4133 | 0.837 |
| MRS S0' | 0.3486 | 0.4118 | 0.847 |
| CTEQ 1M | 0.3522 | 0.4137 | 0.851 |
| CTEQ 1MS | 0.3517 | 0.4152 | 0.847 |
| CTEQ 1L | 0.3422 | 0.4096 | 0.835 |
| CTEQ 1ML | 0.3533 | 0.4159 | 0.849 |
| Uncertainty: | 0.0059 | 0.0029 | 0.009 |

The acceptances depend upon the $W$ mass through the lepton $P_T$'s. Using $M_Z$ = 91.18 $GeV/c^2$, and MRS D-' PDF's we find a 0.1% uncertainty in $A_W/A_Z$ when $M_W$ = 80.2 ±0.2 $GeV/c^2$ is varied wihin its uncertainty, as shown in Table 7.2.

The measurement of the $W$ boson $P_T$ spectrum[27] has sufficiently large uncertainties that the variations in its shape allowed by the measurement lead to variations in the boson acceptances. To estimate the systematic uncertainty due to the input boson $P_T$ distribution, we take the 'nominal' $P_T$ distribution to be the measured spectrum, the 'soft' $P_T$ distribution to be the distribution one gets when varying the nominal by one sigma in each bin so as to give a more steeply falling spectrum (deforming about the point $P_T$ = 16 $GeV/c$), and the 'hard' distribution to be the shape that one gets by varying by one sigma so as to get a more slowly falling spectrum. Trying these three shapes for the $P_T$ choice, we find a 0.2% variation in $A_W/A_Z$,, as shown in Table 7.2.

It has been assumed that the $W$ and $Z^0$ have the same $P_T$ spectra. Experimental measurements of these spectra are consistent with this assumption.[29] Theoretical calculations[30] indicate that the differences are expected to be less than 2%. If we assume that the spectra are different, and use calculations[31] of their individual $P_T$ spectra, we introduce an extra uncertainty from this effect of ±0.0005, which is negligible compared to the ±0.0020 uncertainty from our knowledge of the $W$ $P_T$ spectrum.

The electron energy scale in the data is set for this analysis using $Z^0 \rightarrow e^+e^-$ decays to an accuracy of approximately 0.2%. We vary the energy scale of the central calorimeters in the simulation by 0.2% and summarize the variations in $A_W/A_Z$ in Table 7.2. Variations in the plug detector energy scale cause similar variations in $A_W/A_Z$, while variations in the forward detector energy scale result in 0.2 times this variation in $A_W/A_Z$ because the forward detector has 0.2 times the acceptance of the central and plug. The uncertainty in $A_W/A_Z$ due to the energy scale is estimated to be 0.3%.

We also estimate the systematic uncertainty on $A_W$ due to the model of the $\not{E}_T$ resolution. We have, in addition to the simulation-based model, estimated the acceptances with two other models of the resolution. One model[32] utilizes parameterizations of the calorimeter response to hadrons obtained from a sample of minimum bias triggers, where $\not{E}_T$ is dominated by calorimeter response, not neutrinos. The other model[33] uses $Z^0 \rightarrow e^+e^-$ data to measure the calorimeter response as a function of boson $P_T$. Again, in $Z^0$ events, observed $\not{E}_T$ is dominated by the response to hadrons which recoil against the $Z^0$. This new method would in principle be the best model to use, but we lack adequate statistics in the $Z^0$'s at high $P_T$, where the $\not{E}_T$ smearing is the largest. We find a 0.5% uncertainty in $A_W/A_Z$ due to the choice of the $\not{E}_T$ resolution model, as shown in Table 7.2.

Finally, we investigate the assumption that $A_W/A_Z$ is insensitive to higher-order diagrams. It is likely that the ratio of acceptances is insensitive to *QCD* corrections, since one chooses a common leg in the central region and then the only thing that can change the ratio is a difference in the $\eta$ distribution of the second lepton for *W*'s and $Z^0$'s. With the LO Monte Carlo the $\eta$ distribution of leptons seems well-modeled (see Figures 3.3 and 3.6). We have employed a Monte Carlo program which incorporates a next-to-leading order (NLO) calculation by Giele *et al.*[34]. The events from this generator are fed through the same detector simulation as with the LO Monte Carlo so as to minimize differences in the comparison. The results are shown in Table 7.2. The difference in results is taken as the systematic uncertainty.

**Table 7.2: Systematic Uncertainties in the Boson Acceptances**

| Effect | $\delta A_W$ | $\delta A_Z$ | $\delta(A_W/A_Z)$ |
|---|---|---|---|
| PDF's | 0.0059 | 0.0029 | 0.009 |
| $M_W$ | 0.0004 | - | 0.001 |
| Boson $P_T$ | 0.0019 | 0.0013 | 0.002 |
| Energy Scale | 0.0004 | 0.0030 | 0.003 |
| Neutrino Model | 0.0020 | - | 0.005 |
| NLO Diagrams | 0.0010 | 0.0030 | 0.006 |
| Total Uncertainty: | 0.008 | 0.005 | 0.013 |

## 7.3 Effects of Radiative Corrections

The effects of radiative decay, $Z^0 \rightarrow e^+e^-\gamma$ or $W \rightarrow e\nu\gamma$, are largely accounted for in our calculations of the *E/p* and *Iso* efficiencies for electrons (See Section 8), since most radiated photons tend to be collinear with one of the electrons in *W* or $Z^0$ decay. In addition, the radiated photons tend to shift the lepton $P_T$'s downward, but this shift is largely common to both *W*'s and $Z^0$'s, and hence cancel in the ratio of cross sections. A residual effect to the cross section ratio due to photons radiated at wide angles to the electrons is that the observed $e^+e^-$ pair mass from $Z^0$ decays is shifted downward. We use a Monte Carlo program[35] with the full matrix elements for radiative decay, to find that 0.3 ± 0.2 % of $Z^0$'s fall outside of the 66-116 $GeV/c^2$ mass window after the kinematic cuts are applied. Correcting for this loss of acceptance shifts the result for $A_Z$ from 0.4102 to 0.4090 and $A_W/A_Z$ from 0.833 to 0.835.

## 7.4 Summary of Acceptance Results

Incorporating all the systematic shifts and uncertainties quoted above, we find for the acceptances:

$$A_W = 0.342 \pm 0.001 \text{ (stat.)} \pm 0.008 \text{ (sys.)}$$
$$A_Z = 0.409 \pm 0.001 \text{ (stat.)} \pm 0.005 \text{ (sys.)}$$
$$A_W/A_Z = 0.835 \pm 0.001 \text{ (stat.)} \pm 0.013 \text{ (sys.)}$$

Using the Monte Carlo to calculate the fractions $F_{cc}$, $F_{cp}$, and $F_{cf}$ of $Z^0$'s with one leg in the central that have the second leg in the central, plug, or forward, respectively, we find:

$$F_{cc} = 0.372 \pm 0.001 \text{ (stat.)} \pm 0.007 \text{ (sys.)}$$
$$F_{cp} = 0.509 \pm 0.001 \text{ (stat.)} \pm 0.007 \text{ (sys.)}$$
$$F_{cf} = 0.120 \pm 0.001 \text{ (stat.)} \pm 0.004 \text{ (sys.)}$$

It is important to note that the uncertainty in the ratio of acceptances is smaller than the sum in quadrature of the uncertainties in the individual $W$ and $Z^0$ acceptances. This smaller uncertainty is partially the result of the method of requiring a common central electron for $W$ and $Z^0$ decays which decreases our sensitivity to many of the systematic effects discussed in this section.

# 8. Efficiencies

This section concerns the efficiencies of the leptons from $W$ and $Z^0$ decays to pass the electron selection criteria described in Section 3 and to pass the electron trigger. To estimate these efficiencies, we select a sample of high $P_T$ electrons unbiased by the cuts whose efficiencies we wish to estimate. The high $P_T$ electrons we use come from $W$ and $Z^0$ decay, but are selected with criteria different from those used in Section 3.

We identify 5 efficiencies which must be measured: (1) the efficiency, which we call "$c_1$," for a central electron in the fiducial region from $W$ or $Z^0$ decay to pass the tight cuts; (2) the efficiency, "$c_2$," for the second leg of a $Z^0$ in the fiducial central region to pass the loose central cuts; (3) the efficiency, "$p$," for the second leg of a $Z^0$ in the plug region to pass the loose plug cuts; (4) the efficiency, "$f$," for the second leg of a $Z^0$ in the forward region to pass the loose forward cuts; and finally (5) the efficiency, "$\varepsilon_T$" of a central electron from $W$ or $Z^0$ decay which passes the tight $c_1$ cuts to pass the electron trigger.

The electron identification efficiencies are measured using the second leg of $Z^0$ events. The $Z^0$ events are selected with tight cuts on the first central leg and then requiring for a second electromagnetic cluster that has an invariant mass with the first in a tight window around the $Z^0$ mass. No further identification cuts are used on the second leg. Efficiencies are then measured by observing what fraction of the $Z^0$ second electrons pass the identification cuts.

## 8.1 Tight Central Identification Efficiency, $c_1$

We select a sample of central-central $Z^0$'s which satisfy the following requirements on the event:

One leg passes tight cuts
Second electromagnetic cluster in central with $E_T > 20\ GeV$
CTC (opposite sign) track pointing at 2nd cluster, $P_T > 5\ GeV$
$Iso < 0.05$ on first electron

Had/EM $< 0.05$ on first electron
$81 < M_{e+e-} < 101\ GeV/c^2$

There are 514 central-central $Z^0$'s satisfying these cuts. The efficiency of each of the tight central cuts $c_1$ obtained from this sample is summarized in Table 8.1. The net $c_1$ efficiency, which, because of correlations between the cuts is not simply the product of the cut efficiencies, is 85.1 ± 1.1 %.

**Table 8.1: Efficiency of the Tight Central Cuts**

| Cut | Efficiency (%) |
|---|---|
| Had/EM | $100.0\ ^{+0.0}_{-0.5}$ |
| *Iso* | $97.3 \pm 0.5$ |
| Lshr | $98.0 \pm 0.4$ |
| *E/p* | $95.0 \pm 0.7$ |
| $\delta x$ | $94.1 \pm 0.8$ |
| $\delta z$ | $98.2 \pm 0.4$ |
| $\chi^2 strip$ | $95.0 \pm 0.7$ |
| All Cuts | $85.1 \pm 1.1$ |
| Tracking, *E/p* Corrections | $99.2 \pm 0.4$ |
| $c_1$ Efficiency | $84.5 \pm 1.2$ |

There are two corrections to apply to the result for $c_1$. There is first an efficiency for the offline track reconstruction algorithm to reconstruct a track. This efficiency has been estimated by examining *W*'s which pass $\not{E}_T$ triggers in Level 2 and Level 3. *W* candidates were selected by requiring $E_T > 25\ GeV$, $\not{E}_T > 25\ GeV$, $Lshr < 0.2$, $Iso < 0.1$, $\sqrt{(\chi^2_{strip})^2+(\chi^2_{wire})^2} < 20$. Events with no 3-dimensional track pointing at the cluster were counted as tracking failures. The tracking efficiency was found to be 99.7 ± 0.2 %

We also correct for a small *E/p* bias in our $Z^0$ efficiency sample. In our $Z^0$ efficiency sample, we require a track with $P_T > 5\ GeV$ to point at the second cluster. This cut throws away real $Z^0$'s with $E/p > 4$ from our efficiency sample. To estimate the magnitude of this effect, we scanned the $Z^0$ events which failed the $P_T > 5\ GeV$ cut on the second electron. We factor in an additional efficiency of 99.5 ± 0.3 % as an estimate of this bias.

### 8.2 Loose Central Identification Efficiency, $c_2$

Using the same sample of Section 8.1, we find $c_2$ = 91.7 ± 0.8 %, as summarized in Table 8.2.

**Table 8.2: Efficiency of the Loose Central Cuts**

| Cut | Efficiency (%) |
|---|---|
| Had/EM | $100.0\ ^{+0.0}_{-0.5}$ |
| *Iso* | 97.3 ± 0.5 |
| *E/p* | 95.0 ± 0.7 |
| All Cuts | 92.4 ± 0.7 |
| Tracking, *E/p* Corrections | 99.2 ± 0.4 |
| $c_2$ Efficiency | 91.7 ± 0.8 |

### 8.3 Loose Plug Identification Efficiency, *p*

To measure the efficiency of the plug electron identification efficiencies, we select central-plug $Z^0$ events which pass the following cuts:

One central leg that passes tight cuts
Second electromagnetic cluster in plug with $E_T > 15$ *GeV*
No other jets with $E_T > 10$ *GeV* in the event
$81 < M_{e+e-} < 101$ $GeV/c^2$
Had/EM < 0.05, *Iso* < 0.05 on central electron
VTX Occupancy > 0.5 in octant pointing to plug cluster

There are 418 events passing these cuts. We find a 90.9 ± 1.4% efficiency (see Table 8.3).

**Table 8.3: Efficiency of the Loose Plug Cuts**

| Cut | Efficiency (%) |
|---|---|
| Had/EM | $100.0\ ^{+0.0}_{-0.3}$ |
| *Iso* | 96.4 ± 0.9 |
| $\chi^2_{3\times3}$ | 95.2 ± 1.1 |
| *p* Efficiency | 90.9 ± 1.4 |

## 8.4 Loose Forward Identification Efficiency, $f$

To measure the efficiency of the forward electron identification, we select a sample of central-forward $Z^0$ events identical to the plug sample above, but this time with a forward electron with $E_T > 10$ *GeV* and VTX Occupancy > 0.25. There are 64 events passing these cuts. We find an efficiency of 85.9 ± 4.4%.

Table 8.4: Efficiency of the Loose Forward Cuts

| Cut | Efficiency (%) |
|---|---|
| Had/EM | $100.0\ ^{+0.0}_{-1.8}$ |
| *Iso* | 85.9 ± 4.4 |
| $f$ Efficiency | 85.9 ± 4.4 |

## 8.5 Central Electron Trigger Efficiency, $\varepsilon_T$

The efficiency of the inclusive electron trigger in Level 2 and Level 3 is measured with *W*'s that pass the independent backup trigger that selects events based on $\not{E}_T$ (see Section 2.7). A total of 10813 of our *W* candidates come in on the $\not{E}_T$ triggers. Table 8.5 shows the efficiency results for Level 2 and Level 3.

The Level 1 calorimeter trigger efficiency is estimated using a sample of muon + jet events that trigger the Level 1 and Level 2 muon triggers. The Level 1 calorimeter trigger efficiency is determined from the fraction of jet(s) in these events that satisfy the calorimeter trigger. The Level 1 Calorimeter Trigger is 99.18 ± 0.08% efficient for $E_T > 12$ *GeV* (see Figure 2.12).

Table 8.5: Efficiency of the Central Electron Trigger

| Trigger | Efficiency (%) |
|---|---|
| Level 1 Trigger | 99.2 ± 0.1 |
| Level 2 Trigger | 91.5 ± 0.3 |
| Level 3 Trigger | 98.2 ± 0.1 |
| Total Trigger Eff., $\varepsilon_T$ | 89.2 ± 0.3 |

### 8.6 Combined Efficiencies $\varepsilon_W$ and $\varepsilon_Z$:

Combining the results above, we compute the efficiencies $\varepsilon_W$ and $\varepsilon_Z$ for $W$ and $Z^0$ events to pass our electron selection. The $W$ selection efficiency for electrons in the fiducial region is

$$\varepsilon_W = \varepsilon_T \cdot c_1$$

The $Z^0$ efficiency is more complicated because the central-central $Z^0$'s have two chances for passing the inclusive electron trigger and because the selection criteria have slightly different efficiencies in the three detector regions. Considering only the central region, each leg has three possible outcomes: (a) it can pass tight cuts (see Table 3.1) with probability $\varepsilon_1 = \varepsilon_T c_1$, (b) it can pass loose cuts (see Table 3.2) but not the tight cuts, with probability $\varepsilon_2 = c_2 - \varepsilon_1$, or (c) it can fail the loose cuts as well, with probability $1 - c_2$. Given that 'tight'-'tight' and 'tight'-'loose' combinations are accepted as candidates, the efficiency for central central $Z^0$'s is $(\varepsilon_1)^2 + 2(\varepsilon_1\varepsilon_2)$, or $\varepsilon_T c_1(2c_2 - \varepsilon_T c_1)$. Thus, the $Z^0$ efficiency is:

$$\varepsilon_Z = \varepsilon_T \cdot c_1 \; [\; F_{cc}(2c_2 - \varepsilon_T \cdot c_1) + F_{cp}p + F_{cf}f\,]$$

where the fractions $F_{cc}$, $F_{cp}$, and $F_{cf}$ are the fractions of the $Z^0$'s in our acceptance which have one leg in the central region and the second in the central, plug, and forward, respectively. These fractions are determined with the Monte Carlo described in Section 7. We find for the $W$ and $Z^0$ efficiencies:

$$\varepsilon_W = 75.4 \pm 1.0 \;\%$$
$$\varepsilon_Z = 72.9 \pm 1.6 \;\%$$
$$\varepsilon_W \,/\, \varepsilon_Z = 1.035 \pm 0.016$$

It is important to note that the factor $\varepsilon_T \cdot c_1$ nearly cancels in the ratio $\varepsilon_W / \varepsilon_Z$, and thus the systematic error in $\varepsilon_W / \varepsilon_Z$ is smaller than one gets adding the errors of $\varepsilon_W$ and $\varepsilon_Z$ in quadrature. This lower systematic uncertainty is one of the motivations for selecting a common tight central electron in measuring the ratio of the two cross sections.

# 9. Check of the Results

The analysis for $R$, the $W/Z^0$ cross section ratio, have been presented in Sections 2-8, and the results are presented in Section 10. In this analysis, it has been stressed that many systematic effects tend to cancel in the ratio. These effects include the requirement of a common Central electron, the kinematic criteria, and the lepton identification selection. It has also been stressed that the $W$'s require a larger background subtraction than do the $Z^0$'s. An important check of all these aspects of the result is provided by performing the entire analysis using an $E_T$ cut on the first leg of $E_T > 25$ $GeV$ (for both $W$'s and $Z^0$'s), and a cut of $\not{E}_T > 25$ $GeV$ (for $W$'s). With these cuts, the number of background events to the $W$'s decreases, but Monte Carlo correction for the detector acceptances for $W$'s and $Z^0$'s increases. The comparison is shown below:

$$\frac{\sigma B(W \rightarrow e\nu) \ (20 \ GeV \text{ cuts})}{\sigma B(W \rightarrow e\nu) \ (25 \ GeV \text{ cuts})} = 0.992 \pm 0.003 \ (stat.) \pm 0.008 \ (sys.)$$

$$\frac{\sigma B(Z^0 \rightarrow e^+e^-) \ (20 \ GeV \text{ cuts})}{\sigma B(Z^0 \rightarrow e^+e^-) \ (25 \ GeV \text{ cuts})} = 0.995 \pm 0.007 \ (stat.) \pm 0.008 \ (sys.)$$

$$\frac{R \ (20 \ GeV \text{ cuts})}{R \ (25 \ GeV \text{ cuts})} = 0.995 \pm 0.008 \ (stat.) \pm 0.011 \ (sys.)$$

where the statistical uncertainty in the ratios reflects only the statistically independent part of the two samples and the systematic uncertainty is only the additional uncertainty in the Monte Carlo that results from making higher kinematic cuts. The two measurements are complementary, since both the background and acceptance calculations are thus checked. The analysis with the 20 $GeV$ cuts, however, has a smaller statistical uncertainty and an overall smaller systematic uncertainty, since the systematic uncertainty of determining the efficiency for the higher $\not{E}_T$ cut offsets the smaller background uncertainties.

# 10. Conclusions

Recall that the ratio of $W$ and $Z^0$ cross sections is given by the formula

$$R \equiv \frac{\sigma \cdot B(p\bar{p} \to W \to e\nu)}{\sigma \cdot B(p\bar{p} \to Z^0 \to ee)} = \frac{\sigma(p\bar{p} \to W)}{\sigma(p\bar{p} \to Z^0)} \frac{\Gamma(W \to e\nu)}{\Gamma(Z^0 \to ee)} \frac{\Gamma(Z^0)}{\Gamma(W)}$$

The background, efficiency, and acceptance results from the previous sections are summarized in Table 10.1. We find for the ratio, $R$:

$$R = 10.90 \pm 0.32\,(stat.) \pm 0.29\,(sys.).$$

In order to extract a value for the leptonic branching ratio of the $W$ from the measurement of $R$, we use a theoretical calculation[36] of the ratio of production cross sections $\sigma(p\bar{p} \to W)/\sigma(p\bar{p} \to Z^0) = 3.35 \pm 0.03$, together with the LEP[8] measurements of $\Gamma(Z^0) = 2.4969 \pm 0.0038\ GeV$ and $\Gamma(Z^0 \to e^+e^-) = 83.98 \pm 0.18\ MeV$. We find for the branching ratio:

$$\Gamma(W \to e\nu)/\Gamma(W) = 0.1094 \pm 0.0033(stat.) \pm 0.0031(sys.).$$

The Standard Model Prediction,[5] assuming $m_{top} > M_W - m_b$, is 0.1084 ± 0.0002.

In order to set a model-independent limit on the top mass, we use the 'inverse' branching ratio since its uncertainty is more nearly gaussian: $\Gamma(W)/\Gamma(W \to e\nu) = 9.14 \pm 0.28(stat.) \pm 0.26(sys.)$. As the mass of the top quark increases toward the $W$ mass, the partial width $\Gamma(W \to tb)$ goes to zero, and the ratio $\Gamma(W)/\Gamma(W \to e\nu)$ approaches the Standard Model value of 9.225. In Figure 9.1 we plot our value for $\Gamma(W)/\Gamma(W \to e\nu)$ along with the expected curve as a function of top mass. We establish the limit[37]

$$m_{top} > 62\ GeV/c^2 \text{ (95\% confidence level)}$$

We emphasize again that this limit is independent of models of the top quark's allowed decay modes, providing the $W$ can decay with normal coupling to $t\bar{b}$. Previous direct searches for the top have either assumed that the top must decay only via $Wb$,[1,2] or assumed particular Higgs decay modes, which can depend upon the parameter $\tan\beta$ .[3]

With the present measurement of the $W$ leptonic branching ratio and the previous direct measurement[15] by CDF of the total width, $\Gamma(W)$ = 2.11 ± 0.32 $GeV$, we may extract a measurement of the $W$-fermion coupling, $g$, at $Q^2 = M_W^2$ (see Section 1). We combine the two to obtain $\Gamma(W \rightarrow e\nu)$ = 231 ± 36 $MeV$, and assuming $\Gamma(W \rightarrow \ell\nu) = \frac{g^2 M_W}{48\pi}$ and using the world average[38] for the $W$ mass, $M_W$ = 80.23 ±0.18 $GeV^2$, we find:

$$g = 0.659 \pm 0.052.$$

Note that the Standard Model expectation is $g^2 = \frac{8}{\sqrt{2}} G_F M_W^2$ = 0.425 ± 0.002, or $g$ = 0.652 ± 0.001. The leptonic partial width $\Gamma(W \rightarrow e\nu)$ is preferable to quark widths for extracting a value of $g$, since it does not receive any $QCD$ corrections and it is not sensitive to uncertainties in Cabbibo-Kobayashi-Miskawa matrix elements.

If we assume the Standard Model value of $g$, we can calculate the $W$ leptonic partial width $\Gamma(W \rightarrow e\nu)$ = 225.9 ± 0.9 $MeV$ and obtain a value for $\Gamma(W)$ from the branching ratio measurement:

$$\Gamma(W) = 2.064 \pm 0.060\ (stat.) \pm 0.059 (sys.)\ GeV.$$

It must be emphasized, however, that this value for $\Gamma(W)$ is not sensitive to $g$. The Standard Model prediction,[5] assuming $m_{top} > M_W - m_b$, is $\Gamma(W)$ = 2.067 ± 0.021 $GeV$. Figure 9.2 shows this measurement of $\Gamma(W)$ in comparison to previous measurements.

We thank the Fermilab staff and the technical staffs of the participating institutions for their vital contributions. We thank James Stirling and Jonathan Rosner for important discussions. This work was supported by the U.S. Department of Energy and National Science Foundation; the Italian Istituto Nazionale di Fisica Nucleare; the Ministry of Education, Science and Culture of Japan; the Natural Sciences and Engineering Research Council of Canada; the National Science Council of the Republic of China; the A. P. Sloan Foundation; and the Alexander von Humboldt-Stiftung.

**Table 10.1: Summary of Results for $R$**

| | $W$'s | $Z^0$'s |
|---|---|---|
| Candidates: | 13796 | 1312 |
| Background: | | |
| *hadron jets* | 898 ± 155 | 20 ± 9 |
| $W^{\pm}\to\tau^{\pm}\nu$ | 473 ± 29 | - |
| $Z^0\to\tau^+\tau^-$ | 48 ± 7 | 1 ± 1 |
| $Z^0\to e^+e^-$ | 281 ± 32 | - |
| heavy top | $0^{+40}_{-0}$ | - |
| Total Background: | $1700^{+167}_{-163}$ | 21 ± 9 |
| Signal: | $12096 \pm 117 ^{+163}_{-167}$ | 1291 ± 36 ± 9 |
| Acceptance: | | |
| $A_{W,Z}$ | 0.342 ± 0.008 | 0.409 ± 0.005 |
| $A_W \;/\; A_Z$ | 0.835 ± 0.013 | |
| $F_{cc}$ | - | 0.372 ± 0.007 |
| $F_{cp}$ | - | 0.509 ± 0.007 |
| $F_{cf}$ | - | 0.120 ± 0.004 |
| Efficiencies: | | |
| $\varepsilon_T \cdot c_1$ | 0.754 ± 0.011 | 0.754 ± 0.011 |
| $c_2$ | - | 0.917 ± 0.008 |
| $p$ | - | 0.909 ± 0.014 |
| $f$ | - | 0.859 ± 0.044 |
| $\varepsilon_{W,Z}$ | 0.754 ± 0.011 | 0.729 ± 0.016 |
| $\varepsilon_W \;/\; \varepsilon_Z$ | 1.035 ± 0.016 | |
| Drell-Yan Correction | - | 1.005 ± 0.002 |
| $\sigma(W\to e\nu)\,/\,\sigma(Z\to ee)$ | 10.90 ± 0.32 (*stat.*) ± 0.29 (*sys.*) | |

# References

[1] S. Abachi *et al.*, Phys. Rev. Lett. **72**, 2138 (1994).

[2] F. Abe *et al.*, Phys. Rev. Lett. **73**, 225 (1994); Phys. Rev. **D 50**, 2966(1994).

[3] A direct search for the decay *t→Hb* has also been carried out (F. Abe *et al.*, Phys. Rev. Lett. **72**, 1977 (1994), and F. Abe *et al.*, Phys. Rev. Lett. **73**, 2667 (1994)), but this limit is dependent upon the parameter $\tan\beta = v_1/v_2$, where $v_1$ and $v_2$ are the vacuum expectation values for the two charged Higgs fields.

[4] A. Denner and T. Sack, Zeit. Phys. **C46**, 653 (1990); A. Denner, Fortschr. Phys. **41**, 307 (1993).

[5] J. Rosner, M. Worah, and T. Takeuchi, Phys. Rev. **D 49**, 1363 (1994).

[6] A. Sirlin, Phys. Rev. **D22**, 971 (1980); W. Hollik, Fortschr. Phys. **38**, 165 (1990).

[7] N. Cabbibo, III Topical Conference on Proton-Antiproton Collider Physics, Rome, Jan. 1983; F. Halzen and M. Marsula, Phys. Rev. Lett. **51**, 857 (1983); K. Hikasa, Phys. Rev. **D29**, 1939 (1984); N.G. Deshpande *et al*, Phys. Rev. Lett. **54**, 1757 (1985); A.D. Martin, R.G. Roberts, and W.J. Stirling, Phys. Lett. **B189**, 220 (1987); E.L. Berger, F. Halzen, C.S. Kim, and S. Willenbrock, Phys. Rev. **D40**, 83 (1989).

[8] D. Schaille, talk presented at the XXVII International Conference of High Energy Physics, Glasgow, Scotland (1994).

[9] F. Abe *et al.*, Phys. Rev. Lett. **73**, 220 (1994).

[10] F. Abe *et. al.*, Phys. Rev. Lett. **64**, 152 (1990). The value of $\Gamma(W)/\Gamma(Z)$ from this paper has been multiplied by the most recent measurement[8] of $\Gamma(Z)$.

[11] F. Abe *et. al.*, Phys. Rev. Lett. **69**, 28 (1992).

[12] C. Albajar *et al.*, Phys. Lett. **B253**, 503 (1991)

[13] J. Alitti *et al.*, Phys. Lett. **B276**, 365 (1991).

[14] C. Albajar *et al.*, Z. Phys. **C 44**, 15 (1989).

[15] F. Abe *et al.*, submitted to Phys. Rev. Lett.

[16] S. Kopp, Ph.D. Thesis, The University of Chicago, unpublished, (1994).

[17] P. Roudeau *et. al.*, in CERN-87-08, edited by A. Böhm and W. Hoogland, p. 62.

[18] F. Abe *et al*, Nucl. Instrum. Methods Phys. Res., Sect. **A 271**, 387 (1988); W. Carithers *et. al.*, Nucl. Instrum. Methods Phys. Res., Sect. **A 289**, 388 (1990).

[19] At CDF, the polar angle, $\theta$, in spherical coordinates is measured from the proton beam axis ($z$ axis) and the azimuthal angle $\phi$ is measured from the plane of the Tevatron. The pseudo-rapidity, $\eta$, is defined as $\eta \equiv -\ln(\tan(\theta/2))$.

[20] Hereafter, when the magnitude of the transverse momentum is measured using the calorimeter, we refer to this quantity as the particle's "transverse energy," or $E_T$. When the transverse momentum is measured using the tracking chamber, we denote this quantity as the particle's $P_T$.

[21] For clusters with $E_T > 100\ GeV$, this latter cut is not imposed.

[22] F. Abe *et al*, Nucl. Instr. and Meth. Phys. Res., Sect. **A 269**, 51 (1988); J.T. Carrol *et al*., Nucl. Instr. and Meth. Phys. Res., Sect. **A 300**, 552 (1991).

[23] G.W. Foster *et. al*., Nucl. Instr. Meth. Phys. Res., Sect. **A 269**, 93 (1988).

[24] We have used the ISAJET Monte Carlo program and a detector simulation of these processes, normalized to the number of $W$ and $Z^0$ signal events observed: F. Paige and S. Protopopescu, ISAJET Monte Carlo program, BNL Report No. BNL38034, unpublished, (1986).

[25] D. Buskulic *et al*., Phys. Lett. **B 313**, 535 (1993), and F. Abe *et al*., Phys. Rev. **D 50**, 2966 (1994).

[26] F. Abe *et. al*., Phys. Rev. **D44**, 29 (1991).

[27] F. Abe *et. al*., Phys. Rev. Lett. **66**, 2951 (1991).

[28] A.D. Martin, R. G. Roberts, and W. J. Stirling, Phys. Lett. **B 306**, 145 (1992); *Erratum* Phys. Lett. **B 309**, 492 (1993).

[29] F. Abe *et. al*., Phys. Rev. **D67**, 2937 (1991).

[30] M. H. Reno, University of Iowa report UIOWA-94-01 (1994); H. Baer and M.H. Reno, Forida State report FSU-HEP-901030 (1990); P. Arnold and M.H. Reno, Nucl. Phys. **B319**, 37 (1989).

[31] P. Arnold and R. Kauffman, Nucl. Phys. **B349**, 381 (1991).

[32] F. Abe et. *al*., Phys. Rev. **D43**, 2070 (1991).

[33] F Abe *et al*., "Measurement of the *W* Boson Mass," submitted to Phys. Rev. **▯D**.

[34] W.Giele, D.Glover, and D. Kosower, Fermilab Pub. 92/230-T.

[35] R. G. Wagner, Comput. Phys. Commun. **70**, 15 (1992), based on calculations by F. Berends *et al*., Z. Phys. **C27**, 155 (1985) and F. Berends and R. Kleiss, Z. Phys. **C27**, 365 (1985).

[36] A.D. Martin, W. J. Stirling, and R.G. Roberts, Phys. Lett. **B 228**, 149 (1989) and W.J. Stirling, private communication.

[37] We use the method of M. Aguilar *et. al*., (Particle Data Group), Phys. Lett. **B 204**, 1 (1988), for extracting a limit in the case of a bounded physical region.

[38] C.K. Jung, talk presented at the XXVII International Conference of High Energy Physics, Glasgow, Scotland (1994).

# Figure Captions

Figure 2.1: View of one half of the CDF Detector.

Figure 2.2: View of one wedge of the central calorimeters. Each wedge covers 1 tower in the azimuthal direction ($\Delta\phi$ = 15°) and 10 towers in the $\eta$ direction ($0 < |\eta| < 1.1$). One proportional chamber (CES chamber) is embedded at shower maximum in the range $0 < |\eta| < 0.613$ and another in the range $0.623 < |\eta| < 1.1$. Both edges (1° on either side of the 15° wedge) are uninstrumented in order to leave space for light guides that connect the scintillator to the photomultiplier tubes.

Figure 2.3: Map in $\eta$-$\phi$ space of fiducial volume for electrons.

Figure 2.4: Central identification variables for inclusive electrons (solid histograms) and electrons from $W \to e\nu$ decays (dashed histograms), as described in text.

Figure 2.5: (a) Strip chamber (CES) pulse height for electrons and hadrons; (b) CPR pulse height for electrons and hadrons. The relative normalizations between the two shapes is arbitrary.

Figure 2.6: Signed impact parameter for electrons from $Z^0 \to e^+e^-$ decays observed in the SVX detector.

Figure 2.7: Size in (a) the $x$ and (b) the $y$ view of the overlapping region of proton and antiproton beams for several physics runs (proton stores).

Figure 2.8: (a) The normalized impact parameter distribution, $D/\sigma$, for electrons from $Z^0 \to e^+e^-$ decays. The $\sigma$ agrees well with the sum of the estimated effects of beam spot size and multiple scattering; (b) Invariant mass for $Z^0$'s with $|D/\sigma| > 2$.

Figure 2.9: The distribution, $z_0$, of the position in $z$ of event vertex for inclusive electron events.

Figure 2.10: Plug electron identification variables (see text) for events with one electron in the Central region and a second cluster in the Plug for which the pair has an invariant mass within the 81 - 101 $GeV/c^2$ mass range.

Figure 2.11: Forward electron identification (see text) variables for events in which one electron in the Central region and a second cluster in the Forward for which the pair has an invariant mass within the 81 - 101 $GeV/c^2$ mass range.

Figure 2.12: Electron trigger efficiency in (a) Level 1, (b) Level 2, and (c) Level 3 *vs.* the electron $E_T$. The measurement of the electron trigger efficiency is described in Section 8.5.

Figure 2.13: Efficiency of the electron trigger *vs.* $\eta$ (a) in Level 2 and (b) in Level 3. The measurement of the electron trigger efficiency is described in Section 8.5.

Figure 2.14: Fitted $\sigma(\not{E}_X)$ *vs* $\Sigma(E_T)$ in minimum bias trigger events. The curve is a best fit of a square root function to the data. The curve does not pass through the origin because run-by-run offsets and out-of-time accidental energy were not corrected for.

Figure 2.15: The missing $E_T$ significance for the $W$ candidate events and for a sample of minimum-bias-triggered events.

Figure 3.1: The $E_T$ distribution of inclusive electrons, isolated inclusive electrons, and electrons from $W \rightarrow e\nu$ decays.

Figure 3.2: Invariant mass spectrum of $e^+e^-$ pairs with one tight central electron and a second cluster, with and without the cuts of Table 3.2 imposed on the second cluster.

Figure 3.3: Distribution in $\eta$ of the second electron in $Z^0 \rightarrow e^+e^-$ decays for the data and the Monte Carlo described in Section 7.

Figure 3.4: Isolation of the electron *vs.* the $\not{E}_T$ in the event. Events with a second electromagnetic cluster have been explicitly removed from this plot.

Figure 3.5: $\not{E}_T$ spectrum of inclusive electrons with (a) $Iso > 0.3$; (b) $Iso < 0.1$. The peak at approximately 8 *GeV* is due to resolution effects and the peak at 40 *GeV* is due to neutrinos from *W* decays. Events with a second electromagnetic cluster have been explicitly removed from these plots.

Figure 3.6: Distribution in $\eta$ of electrons from $W \rightarrow e\nu$ decays in the data and the Monte Carlo described in Section 7. The Monte Carlo has been also folded in with the trigger efficiency from Figure 2.13.

Figure 4.1: Distributions in the variables for track pairs used to identify photon conversions: (a) $\delta\ (r\text{-}\phi)$; (b) $\delta\ (\cot\theta)$.

Figure 4.2: CES pulse height for partner tracks tagged as conversion pairs and the expected shape for real electrons. Note the excess of track partners at low pulse height beyond that expected for real electrons, indicating the presence of minimum-ionizing hadrons in the coversion pair sample.

Figure 4.3: Probability that the jet comes from the primary vertex for jets in inclusive electron events with $\not{E}_T < 10$ *GeV*. The distributions are shown for jets in which all tracks and only negatively-signed impact parameter tracks are incorporated into the jet probability. The negatives' jet probability shape is indicative of the resolution, and, hence, the shape for light quark jets.

Figure 4.4: $D/\sigma$ of all the electrons in the non-$W/Z^0$ electron sample, along with the expected shape from electrons from *b* decay and conversions + fake electrons (pions or multihadrons).

Figure 4.5: CPR charge for all electron clusters in the non-$W/Z^0$ sample, along with the expected shape for electrons and for hadrons.

Figure 4.6: $E_T$ spectrum of inclusive electrons, along with the expected shape for electrons from hadron jets and the expected shape for electrons from $W/Z^0$ decays. The shapes are absolutely normalized (see text).

Figure 5.1: *Iso* of the central electron in (a) the $\not{E}_T <$ 10 *GeV* sample (b) the $\not{E}_T >$ 20 *GeV* sample. In (a) are also shown the isolation of the electron for the two subsets of the $\not{E}_T <$ 10 *GeV* sample with an additional jet besides the electron jet with $E_T <$ 10 and 20 *GeV*.

Figure 5.2: Mean electron *Iso vs.* the $E_T$ of the opposing jet in the $\not{E}_T <$ 10 *GeV* region. As the jet opposing the electron jet stiffens, momentum balance requires the particles in the electron jet to stiffen, and they are thus less likely to be bent out of the *Iso* cone by the magnetic field.

Figure 5.3: $\not{E}_T$ for events with electrons tagged as conversions with $\not{E}_T >$ 20 *GeV*, along with the expected $\not{E}_T$ shape for *W* events, where the *W* electron event is falsely tagged as a conversion.

Figure 5.4: (a) $D/\sigma$ of electrons in the $\not{E}_T >$ 20 *GeV* sample; (b) $\not{E}_T$ of events with $\not{E}_T$ >20 *GeV* in which the electron has $|D/\sigma| > 2$, along with the $\not{E}_T$ shape for *W*'s where the impact parameter has been mismeasured.

Figure 5.5: CPR charge of $\not{E}_T >$ 20 *GeV* electrons, along with the expected shape of electrons and the shape for hadrons.

Figure 5.6: Invariant mass of the tight central electron and the second high-$P_T$ track, both with and without the cuts on the second track (see text). The long tail below the $Z^0$ mass is due to the photons radiated away by the second electron track.

Figure 5.7: Local calorimeter position of the second track in $Z^0 \rightarrow e^+e^-$ candidates within the *W* sample when no second calorimeter cluster is observed.

Figure 5.8: Electron $E_T$ in $W \rightarrow e\nu$ decays. The background contributions are described in Section 5 and the *W* shape is determined using the Monte Carlo described in Section 7. The uncertainty in the Monte Carlo is the spread resulting from the uncertainty on the *W* boson $P_T$ shape that is input to the Monte Carlo.

Figure 5.9: $\not{E}_T$ of $W \rightarrow e\nu$ decays. The background contributions are described in Section 5 and the *W* shape is determined using the Monte Carlo described in Section 7.

The uncertainty in the Monte Carlo is the spread resulting from the uncertainty on the $W$ boson $P_T$ shape that is input to the Monte Carlo.

Figure 5.10: Transverse mass of $W \rightarrow e\nu$ decays. The background contributions are described in Section 5 and the $W$ shape is determined using the Monte Carlo described in Section 7.

Figure 6.1: Invariant mass of the two electrons *vs.* the *Iso* of the second electron.

Figure 6.2: Invariant mass of $Z^0 \rightarrow e^+e^-$ decays. The background contributions are described in Section 6 and the $Z^0$ shape is determined using the Monte Carlo described in Section 7. Both $Z^0$ and Drell-Yan photon terms are included.

Figure 10.1: $BR(W \rightarrow e\nu)^{-1}$ *vs.* $M_{top}$. As the top mass increases toward the $W$ mass, the phase space for the decay $W \rightarrow tb$ is reduced.

Figure 10.2: Previous measurements of $\Gamma(W)$, along with the present measurement.

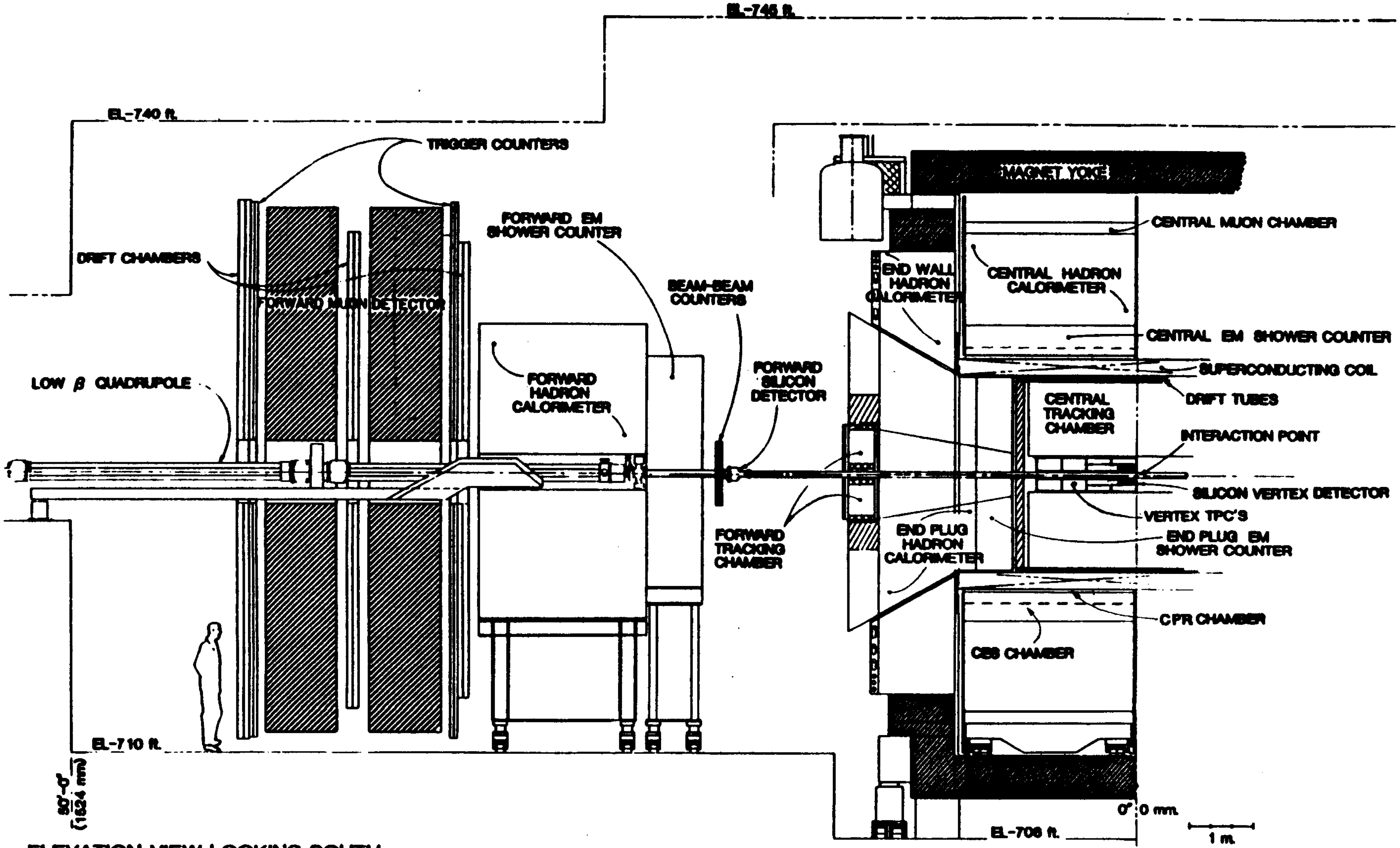

ELEVATION VIEW LOOKING SOUTH

2.1

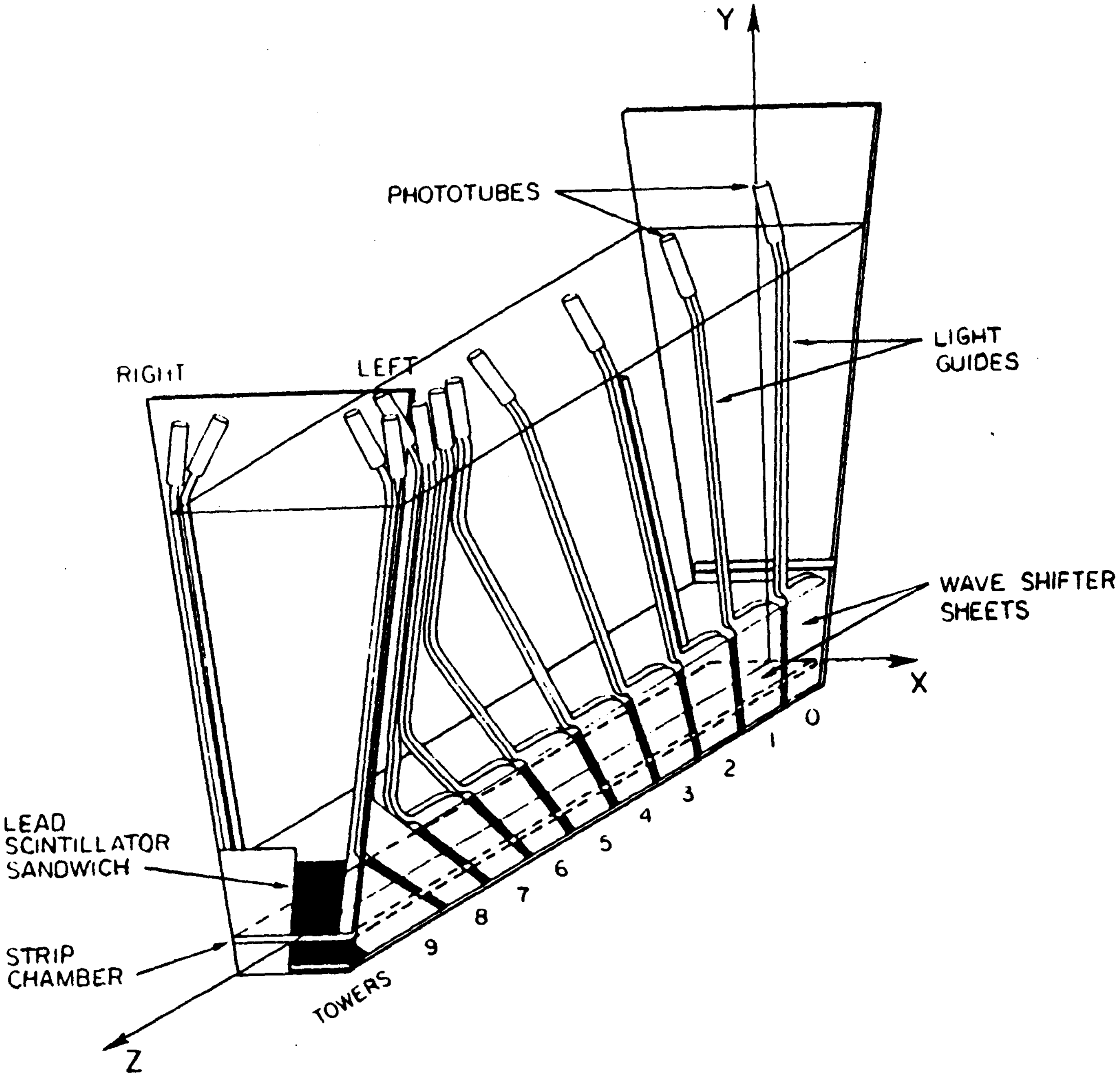
Y
PHOTOTUBES
LIGHT GUIDES
RIGHT
LEFT
WAVE SHIFTER SHEETS
X
0
1
2
3
4
5
6
7
8
9
TOWERS
LEAD SCINTILLATOR SANDWICH
STRIP CHAMBER
Z

Figure 2.3

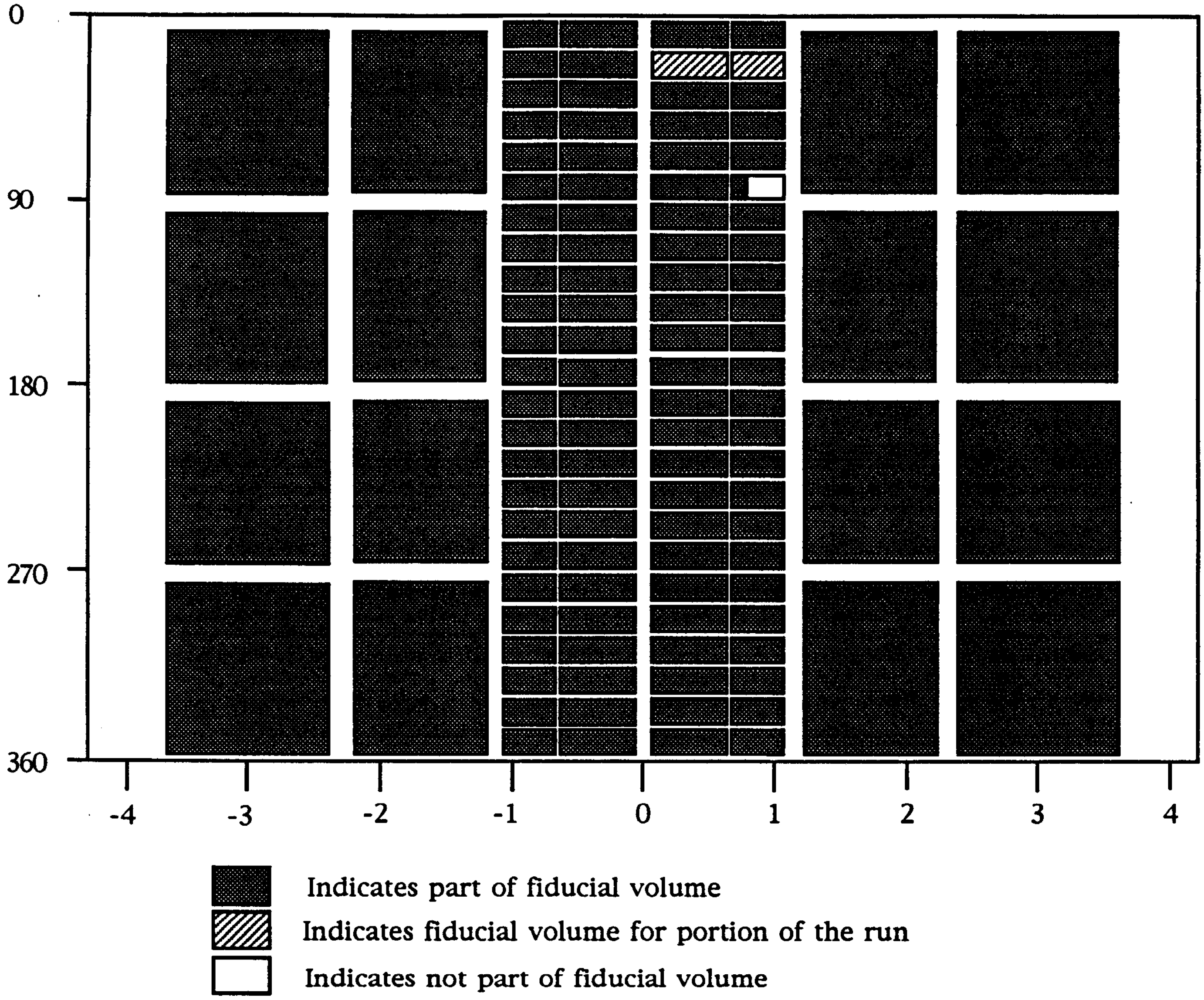
0
90
180
270
360
-4
-3
-2
-1
0
1
2
3
4
Indicates part of fiducial volume
Indicates fiducial volume for portion of the run
Indicates not part of fiducial volume

Figure 2.4 (a – d)

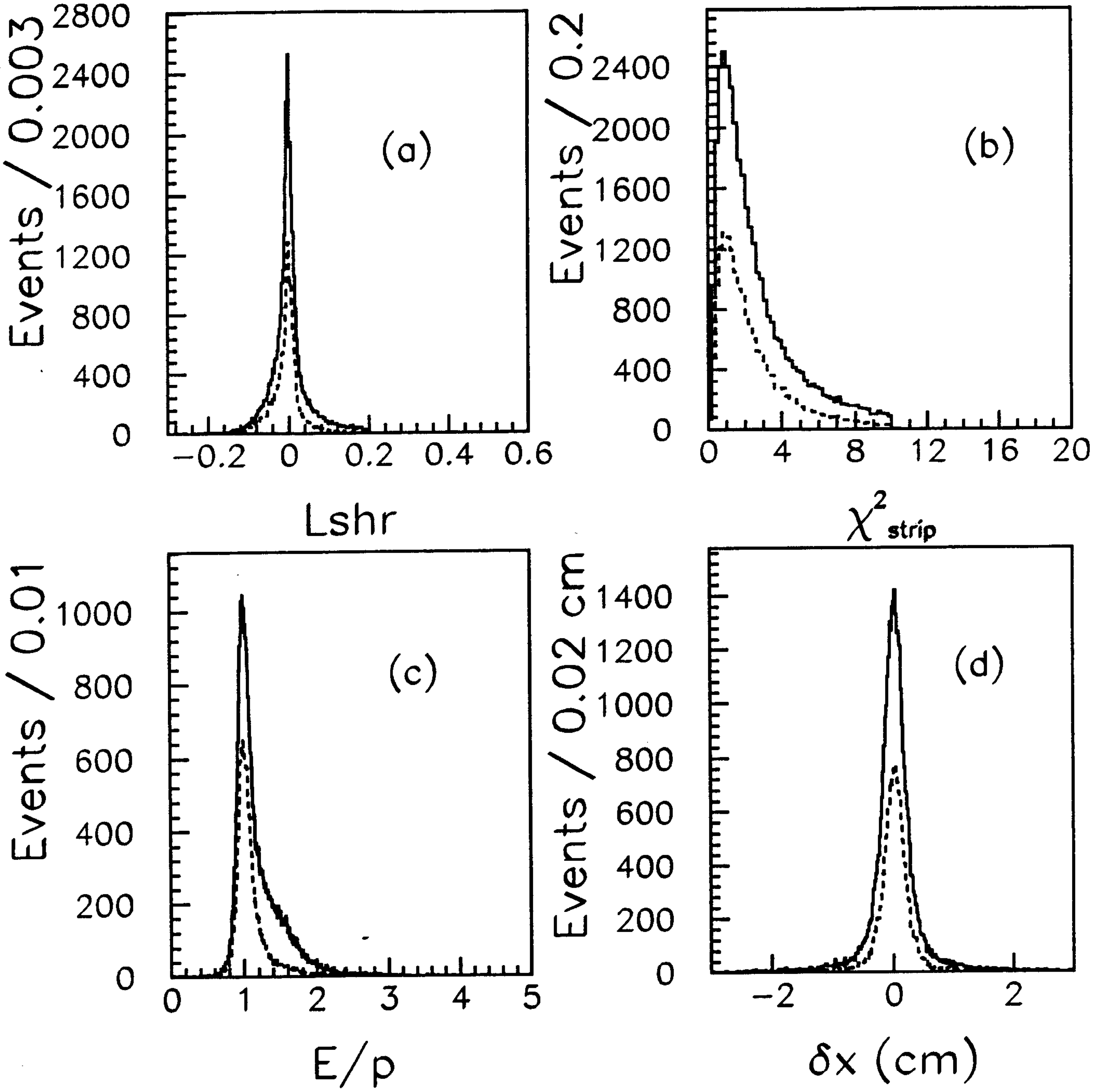

Events / 0.003
2800
2400
2000
1600
1200
800
400
0
(a)
−0.2
0
0.2
0.4
0.6
Lshr
Events / 0.2
2400
2000
1600
1200
800
400
0
(b)
0
4
8
12
16
20
$\chi^2_{strip}$
Events / 0.01
1000
800
600
400
200
0
(c)
0
1
2
3
4
5
E/p
Events / 0.02 cm
1400
1200
1000
800
600
400
200
0
(d)
−2
0
2
δx (cm)

Figure 2.4 (e – g)

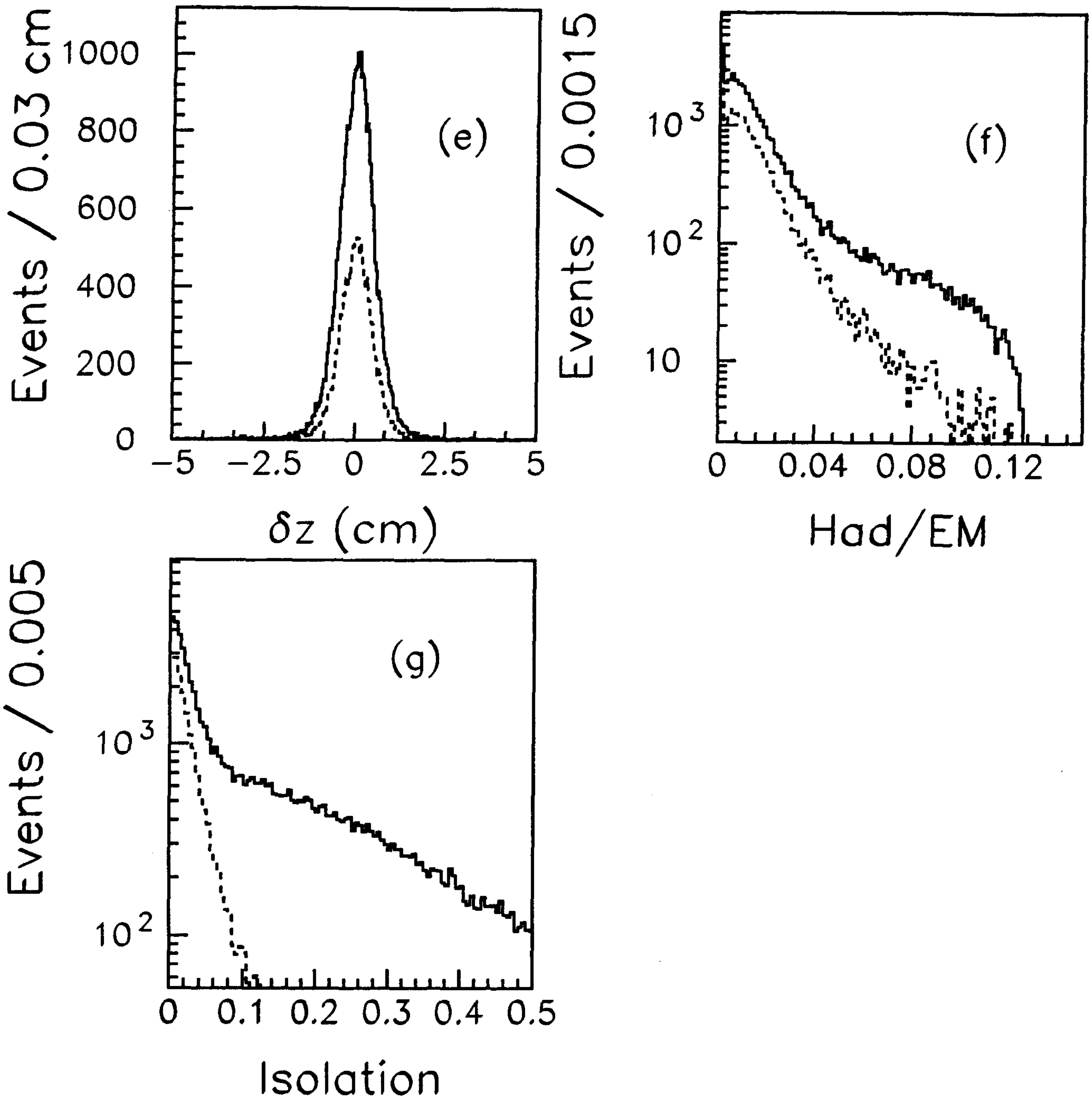

(e)
Events / 0.03 cm
0
200
400
600
800
1000
−5
−2.5
0
2.5
5
δz (cm)
(f)
Events / 0.0015
10
$10^2$
$10^3$
0
0.04
0.08
0.12
Had/EM
(g)
Events / 0.005
$10^2$
$10^3$
0
0.1
0.2
0.3
0.4
0.5
Isolation

Figure 2.5

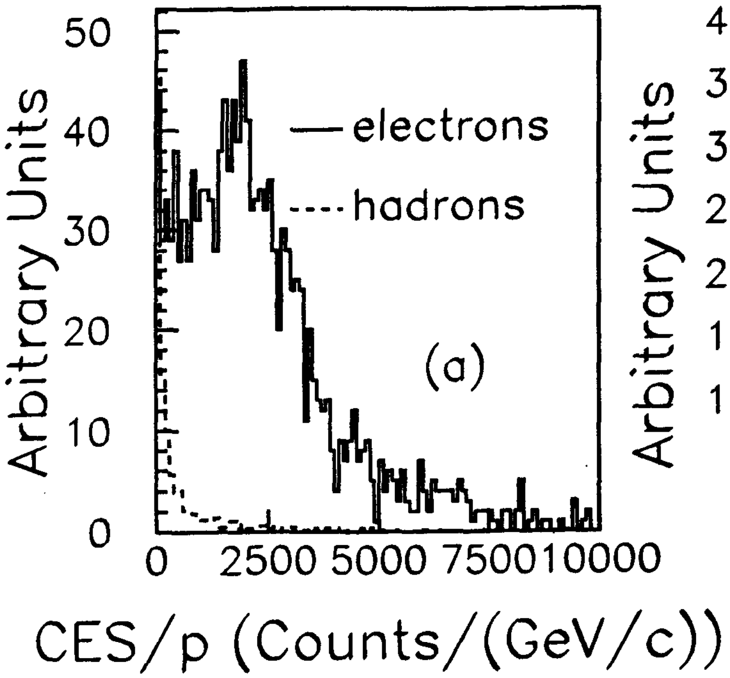
Arbitrary Units
50
40
30
20
10
0
0
2500
5000
7500
10000
—electrons
----hadrons
(a)
CES/p (Counts/(GeV/c))
Arbitrary Units
400
350
300
250
200
150
100
50
0
0
20000
40000
—electrons
----hadrons
(b)
CPR Charge (fC)

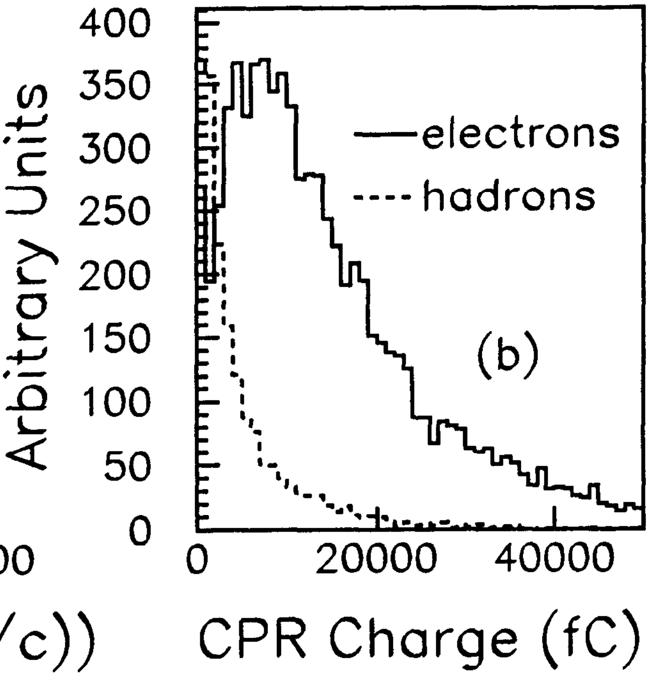

## Figure 2.6

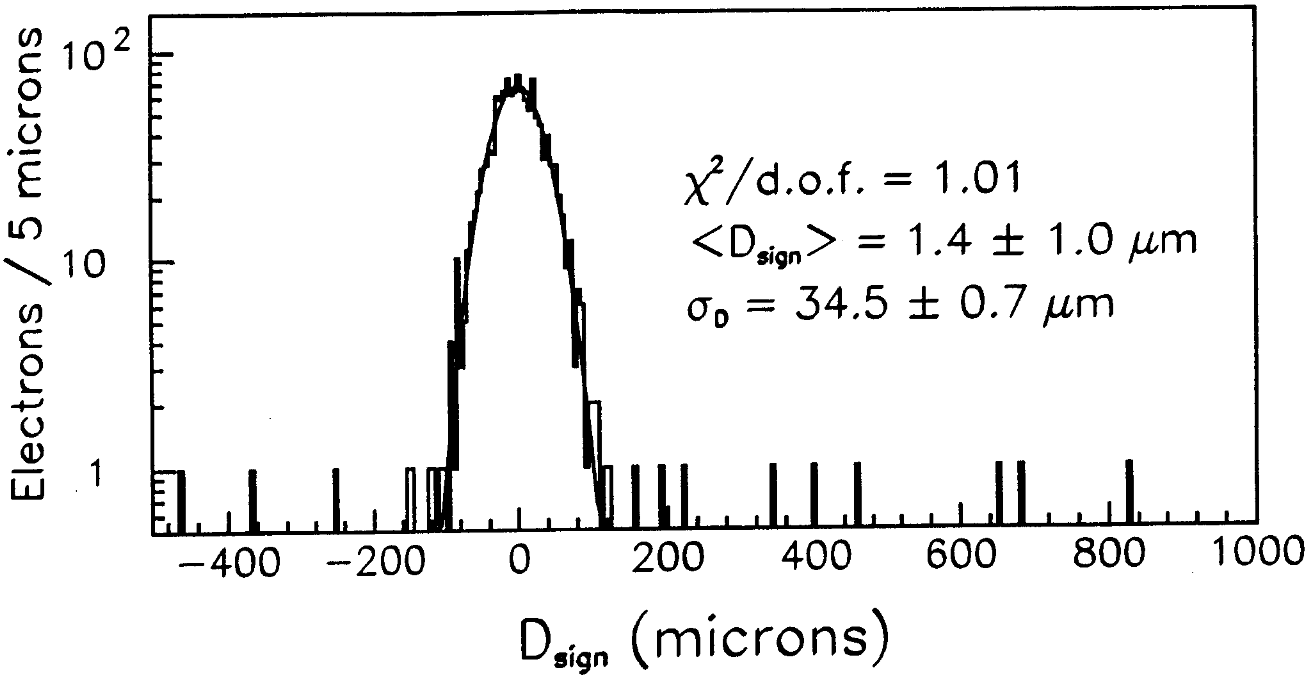
Electrons / 5 microns
$10^2$
10
1
−400
−200
0
200
400
600
800
1000
$D_{sign}$ (microns)
$\chi^2$/d.o.f. = 1.01
$\langle D_{sign} \rangle = 1.4 \pm 1.0\ \mu m$
$\sigma_D = 34.5 \pm 0.7\ \mu m$

Figure 2.7

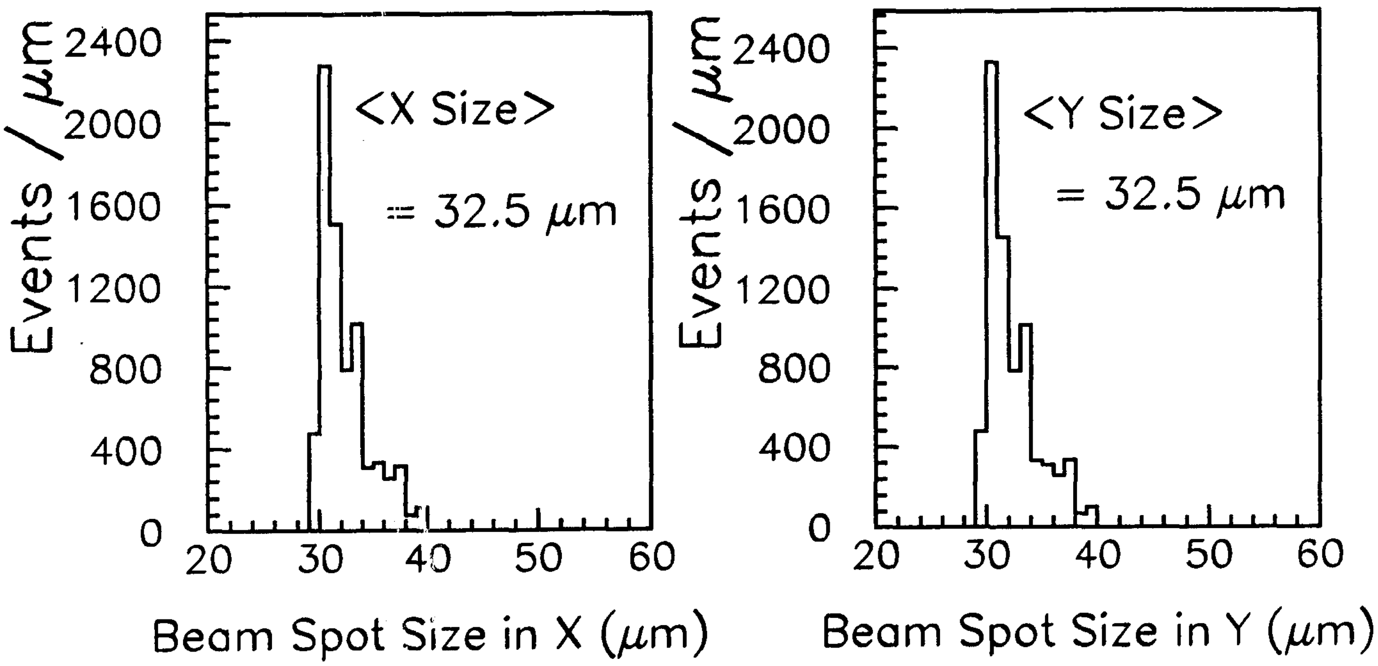
Events / μm
2400
2000
1600
1200
800
400
0
20
30
40
50
60
<X Size>
= 32.5 μm
Beam Spot Size in X (μm)
Events / μm
2400
2000
1600
1200
800
400
0
20
30
40
50
60
<Y Size>
= 32.5 μm
Beam Spot Size in Y (μm)

Figure 2.8

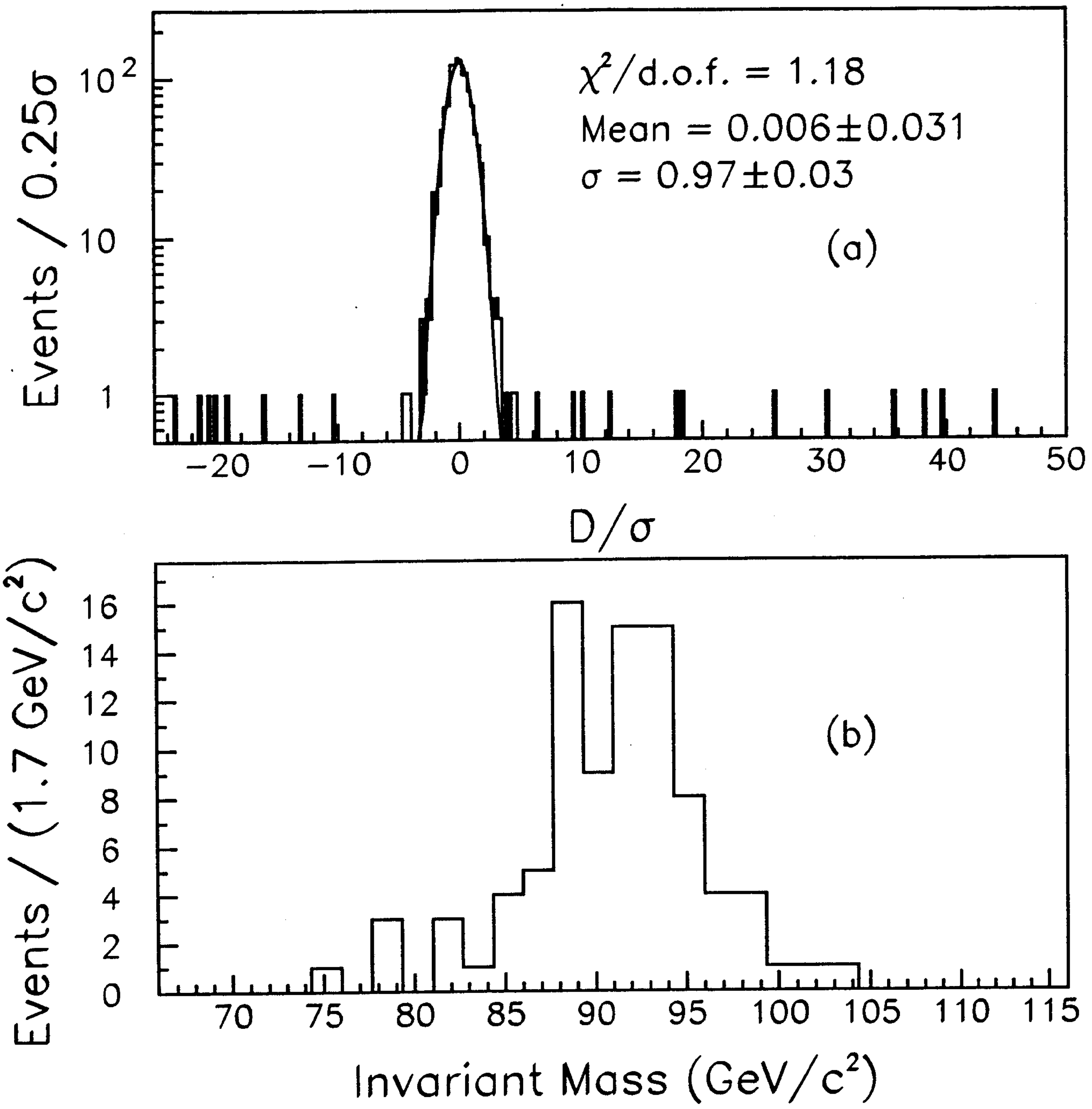
Events / 0.25σ
$10^2$
10
1
$\chi^2$/d.o.f. = 1.18
Mean = 0.006±0.031
σ = 0.97±0.03
(a)
−20
−10
0
10
20
30
40
50
D/σ
Events / (1.7 GeV/$c^2$)
16
14
12
10
8
6
4
2
0
(b)
70
75
80
85
90
95
100
105
110
115
Invariant Mass (GeV/$c^2$)

Figure 2.9

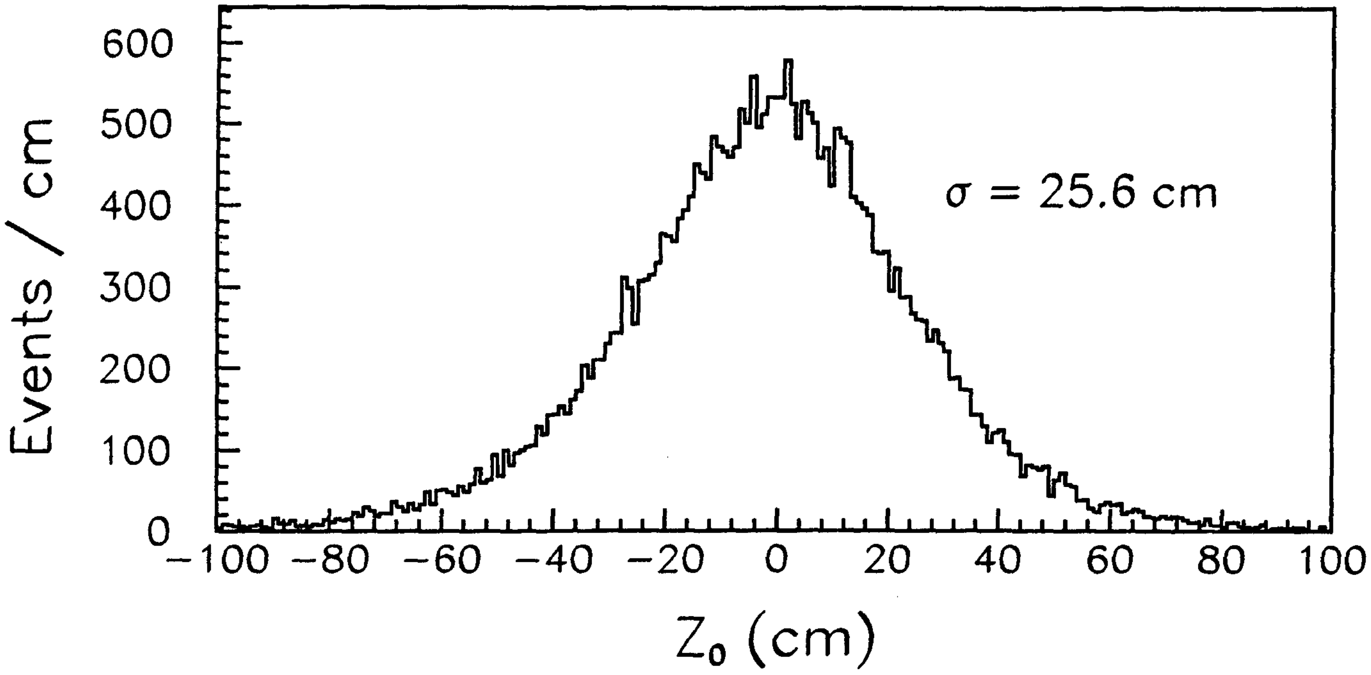
Events / cm
600
500
400
300
200
100
0
−100
−80
−60
−40
−20
0
20
40
60
80
100
Z₀ (cm)
σ = 25.6 cm

Figure 2.10

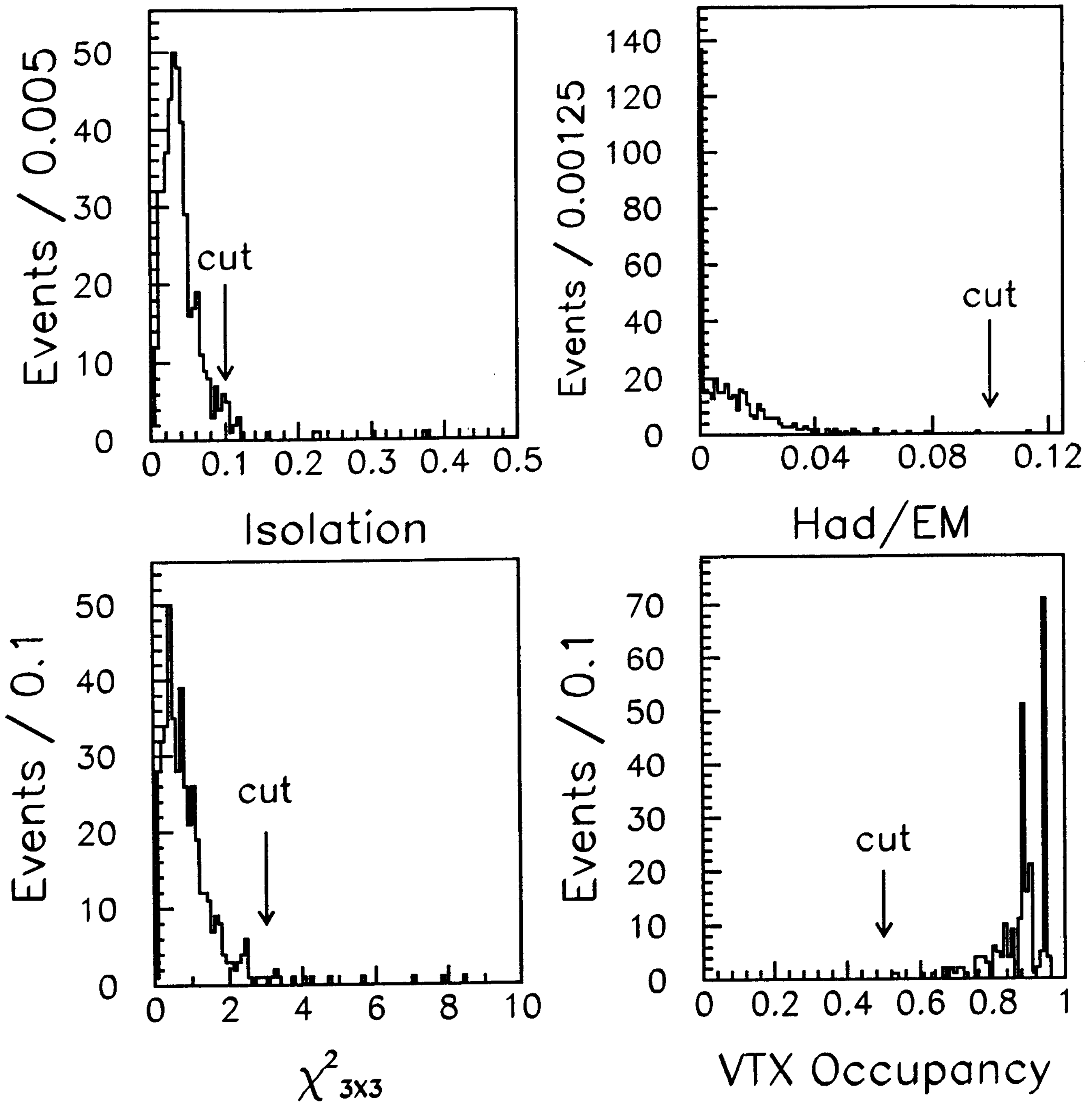
Events / 0.005
0
10
20
30
40
50
0
0.1
0.2
0.3
0.4
0.5
cut
Isolation
Events / 0.00125
0
20
40
60
80
100
120
140
0
0.04
0.08
0.12
cut
Had/EM
Events / 0.1
0
10
20
30
40
50
0
2
4
6
8
10
cut
$\chi^2_{3X3}$
Events / 0.1
0
10
20
30
40
50
60
70
0
0.2
0.4
0.6
0.8
1
cut
VTX Occupancy

Figure 2.11

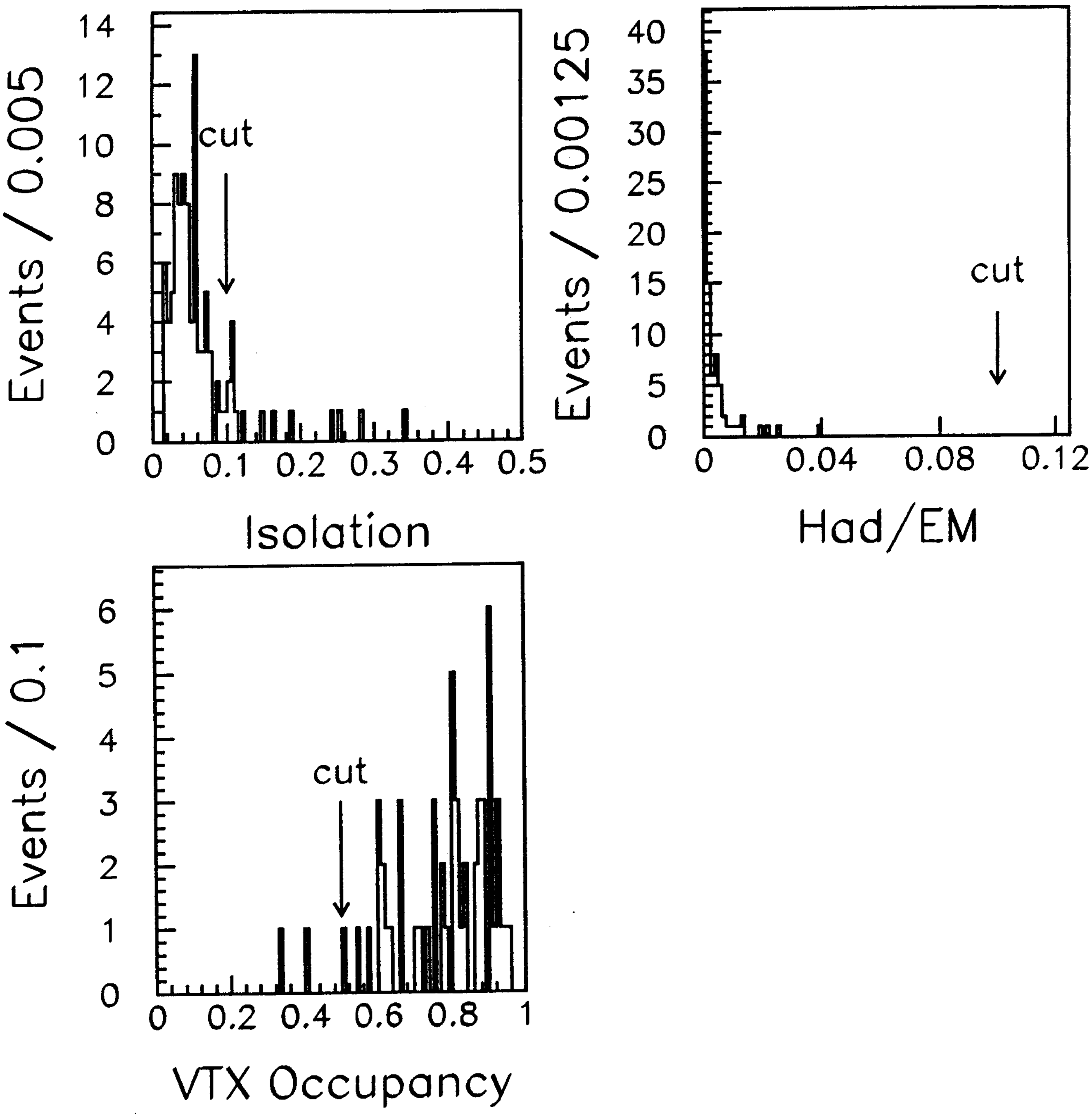
Events / 0.005
14
12
10
8
6
4
2
0
0
0.1
0.2
0.3
0.4
0.5
Isolation
cut
Events / 0.00125
40
35
30
25
20
15
10
5
0
0
0.04
0.08
0.12
Had/EM
cut
Events / 0.1
6
5
4
3
2
1
0
0
0.2
0.4
0.6
0.8
1
VTX Occupancy
cut

Figure 2.12

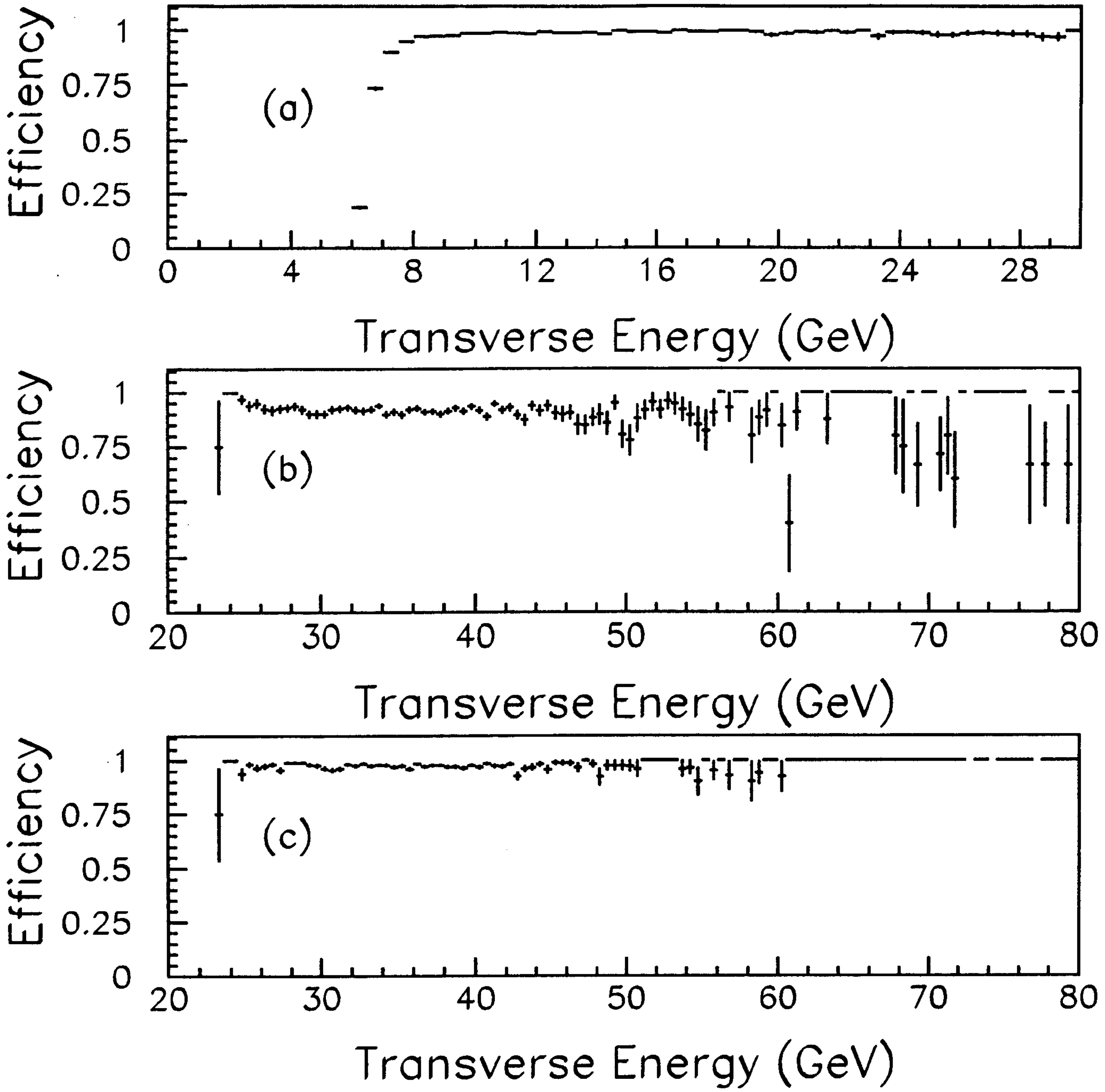
Efficiency
1
0.75
0.5
0.25
0
(a)
0
4
8
12
16
20
24
28
Transverse Energy (GeV)
Efficiency
1
0.75
0.5
0.25
0
(b)
20
30
40
50
60
70
80
Transverse Energy (GeV)
Efficiency
1
0.75
0.5
0.25
0
(c)
20
30
40
50
60
70
80
Transverse Energy (GeV)

Figure 2.13

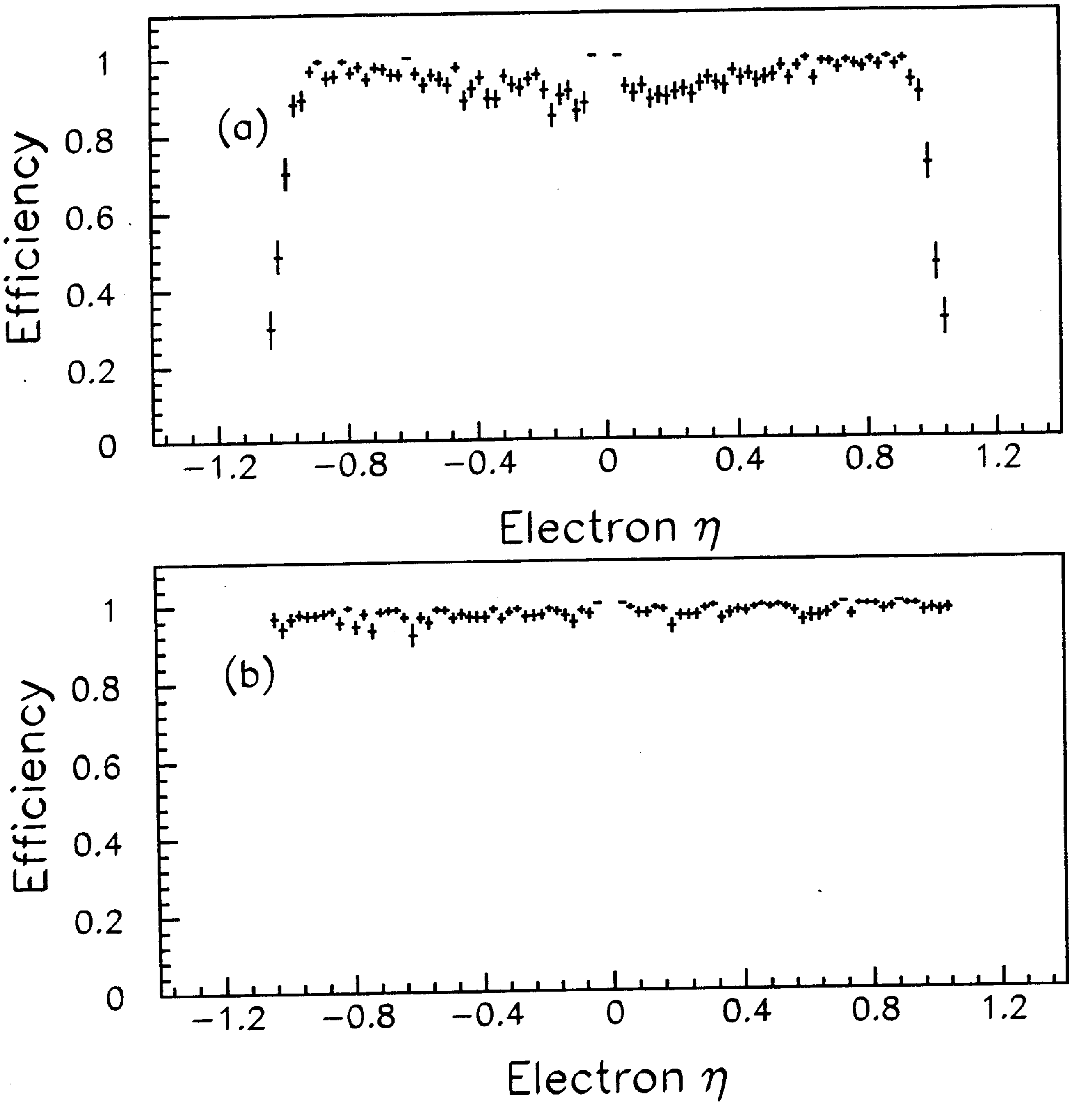
(a)
(b)
Efficiency
Efficiency
0
0.2
0.4
0.6
0.8
1
−1.2
−0.8
−0.4
0
0.4
0.8
1.2
Electron $\eta$
Electron $\eta$

Figure 2.14

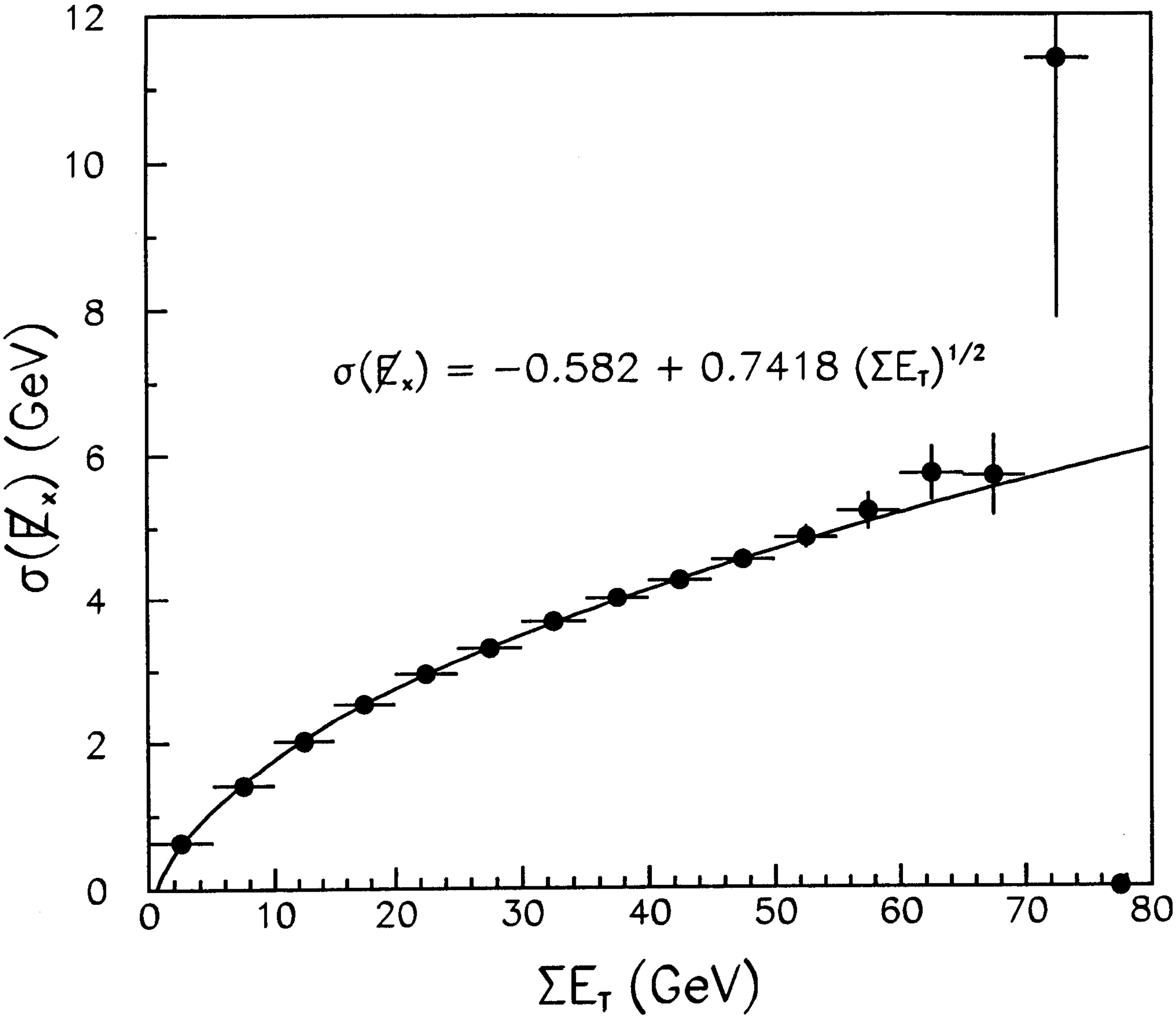
$\sigma(\not{E}_x) = -0.582 + 0.7418\,(\Sigma E_T)^{1/2}$
$\sigma(\not{E}_x)$ (GeV)
$\Sigma E_T$ (GeV)
0
2
4
6
8
10
12
0
10
20
30
40
50
60
70
80

Figure 2.15

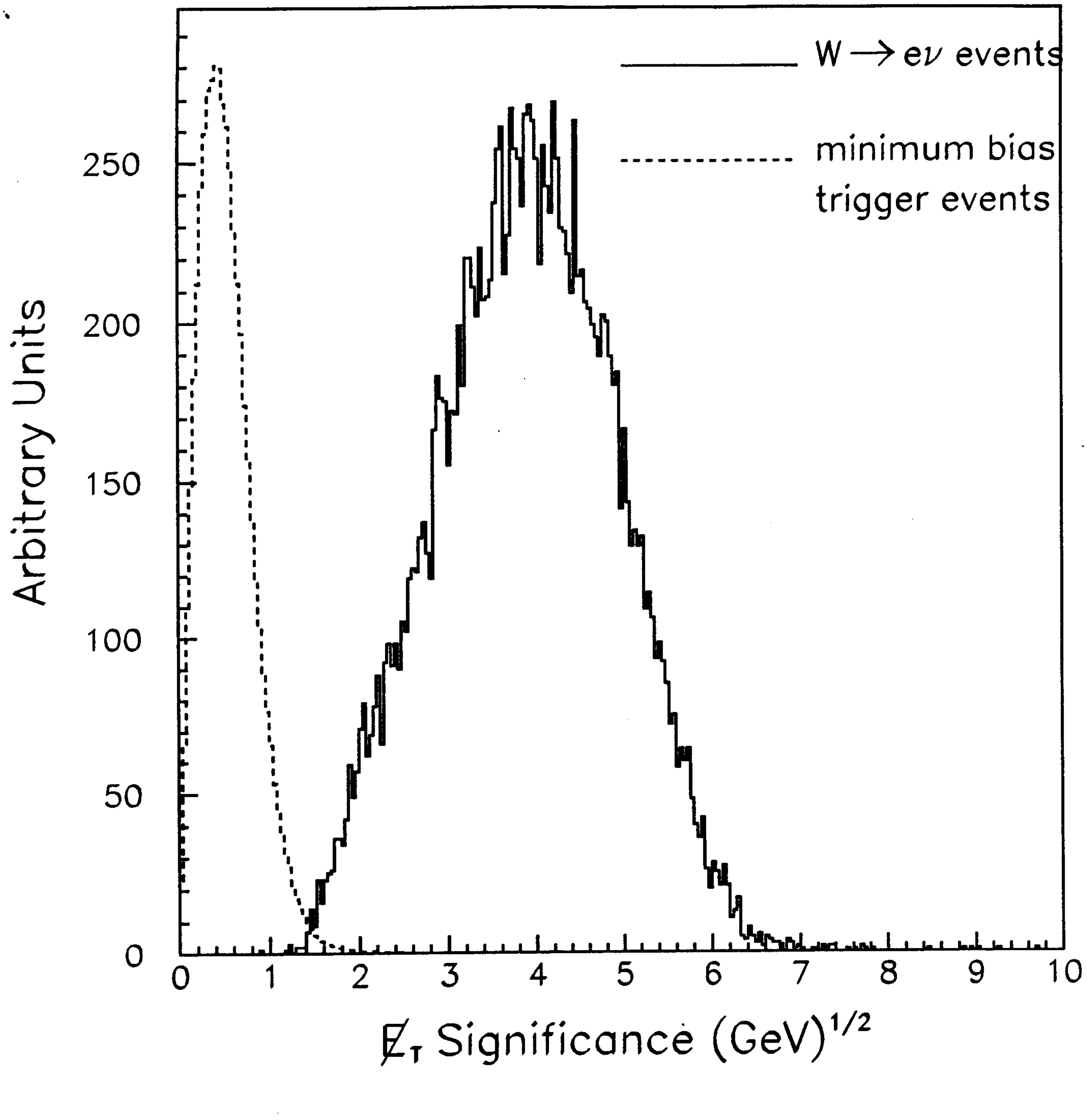
W → eν events
minimum bias
trigger events
Arbitrary Units
0
50
100
150
200
250
0
1
2
3
4
5
6
7
8
9
10
$\not{E}_T$ Significance (GeV)$^{1/2}$

Figure 3.1

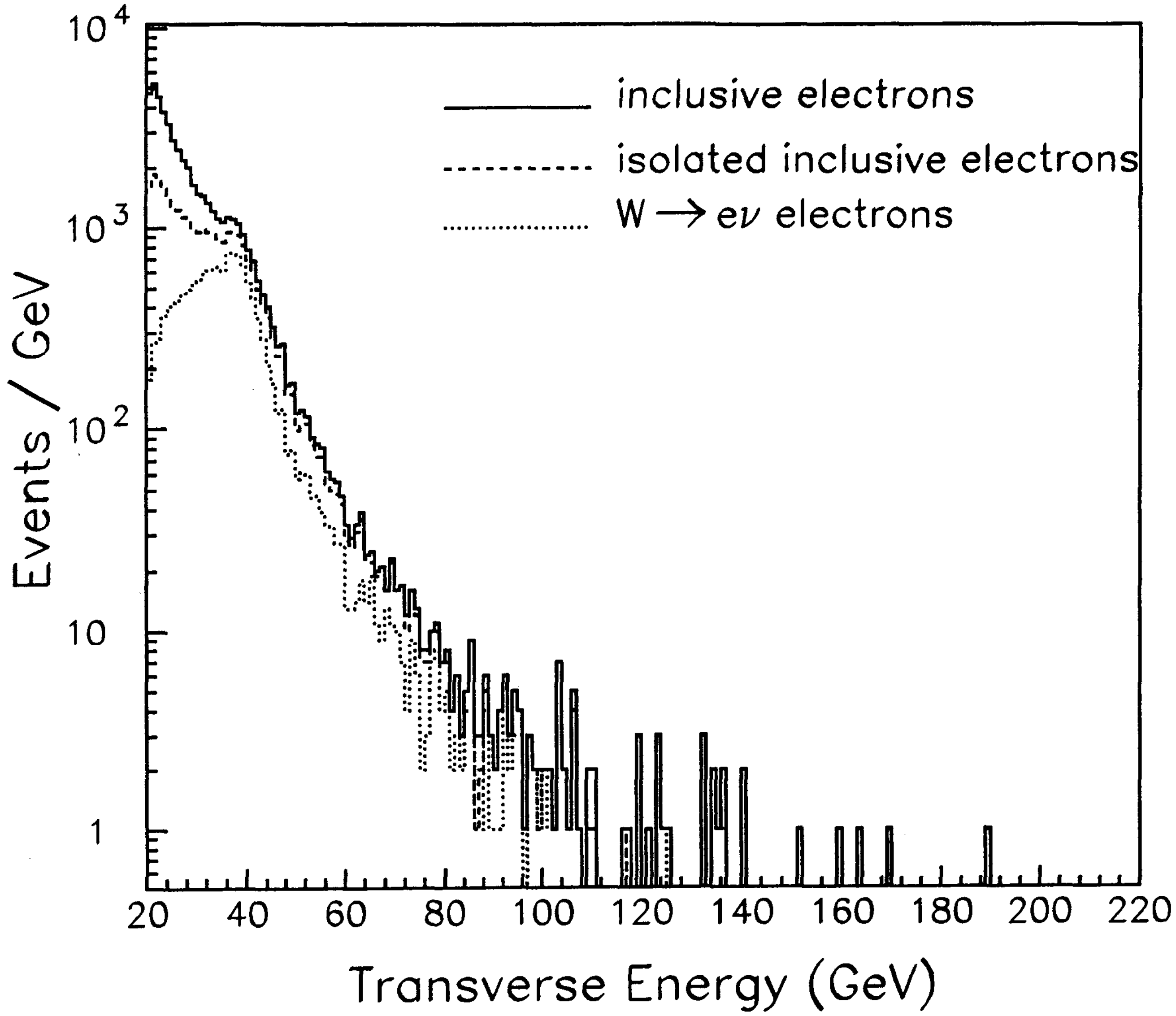
inclusive electrons
isolated inclusive electrons
W ⟶ eν electrons
Events / GeV
10⁴
10³
10²
10
1
20
40
60
80
100
120
140
160
180
200
220
Transverse Energy (GeV)

Figure 3.2

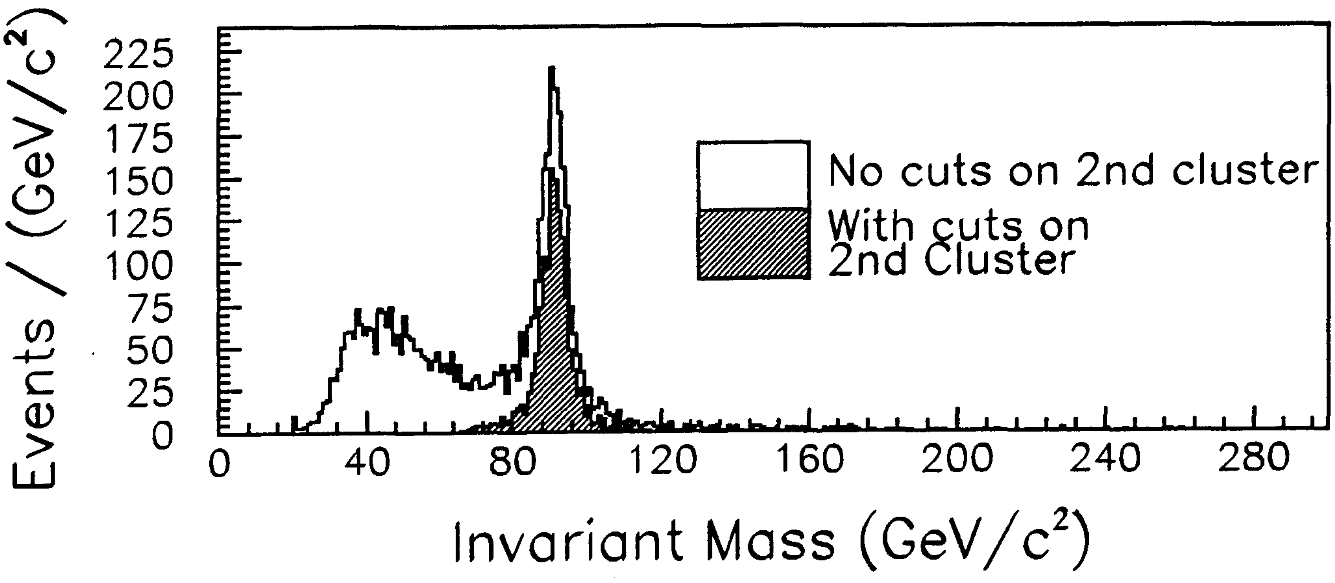
Events / (GeV/c²)
225
200
175
150
125
100
75
50
25
0
0
40
80
120
160
200
240
280
Invariant Mass (GeV/c²)
No cuts on 2nd cluster
With cuts on 2nd Cluster

Figure 3.3

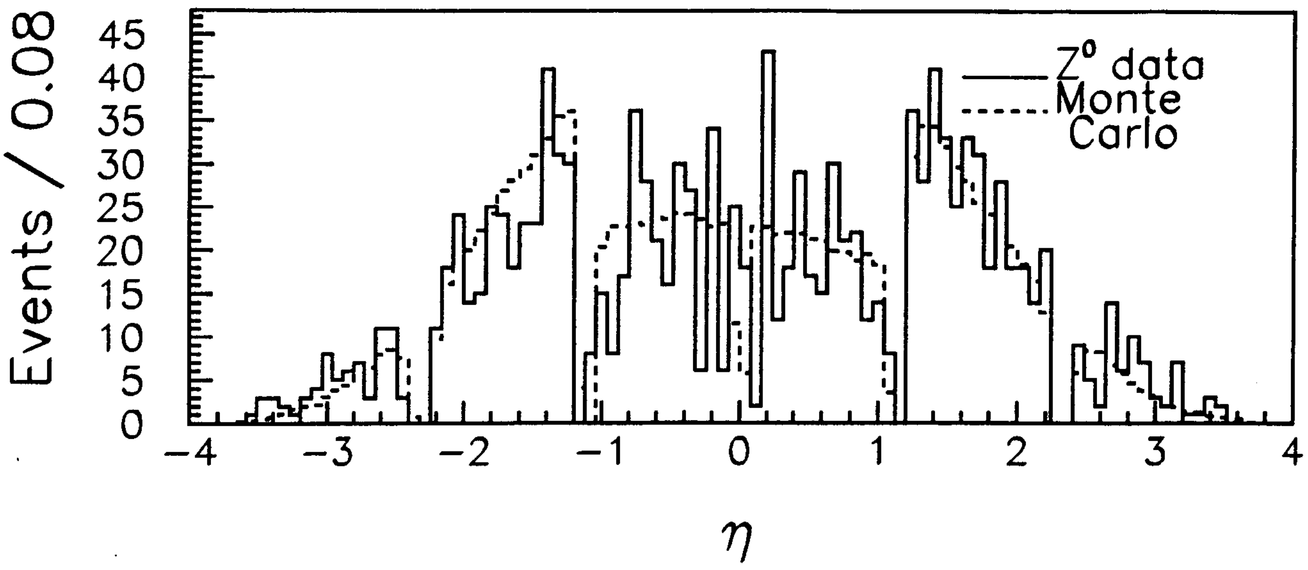
Events / 0.08
0
5
10
15
20
25
30
35
40
45
−4
−3
−2
−1
0
1
2
3
4
η
Z⁰ data
Monte Carlo

Figure 3.4

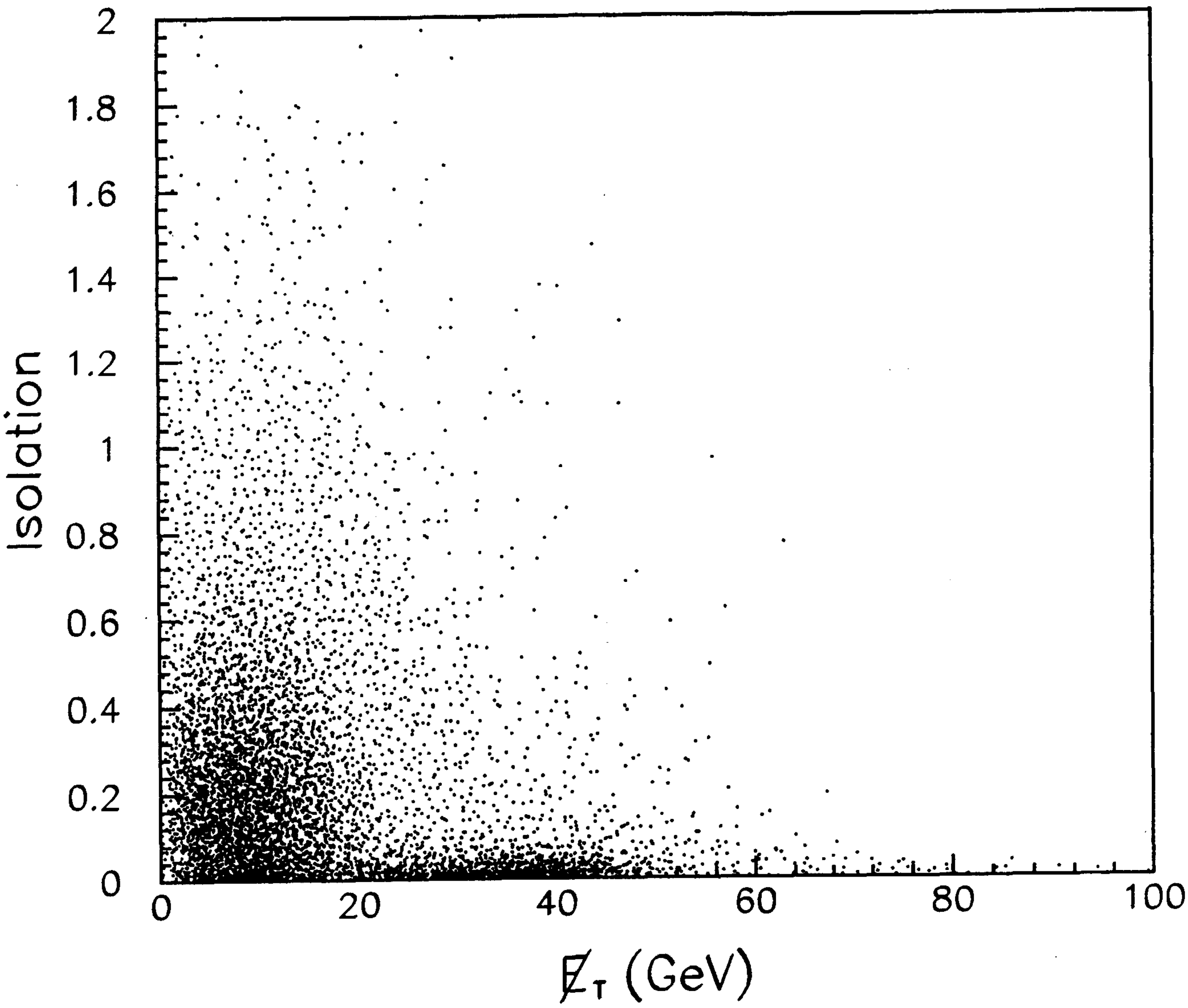

Figure 3.5

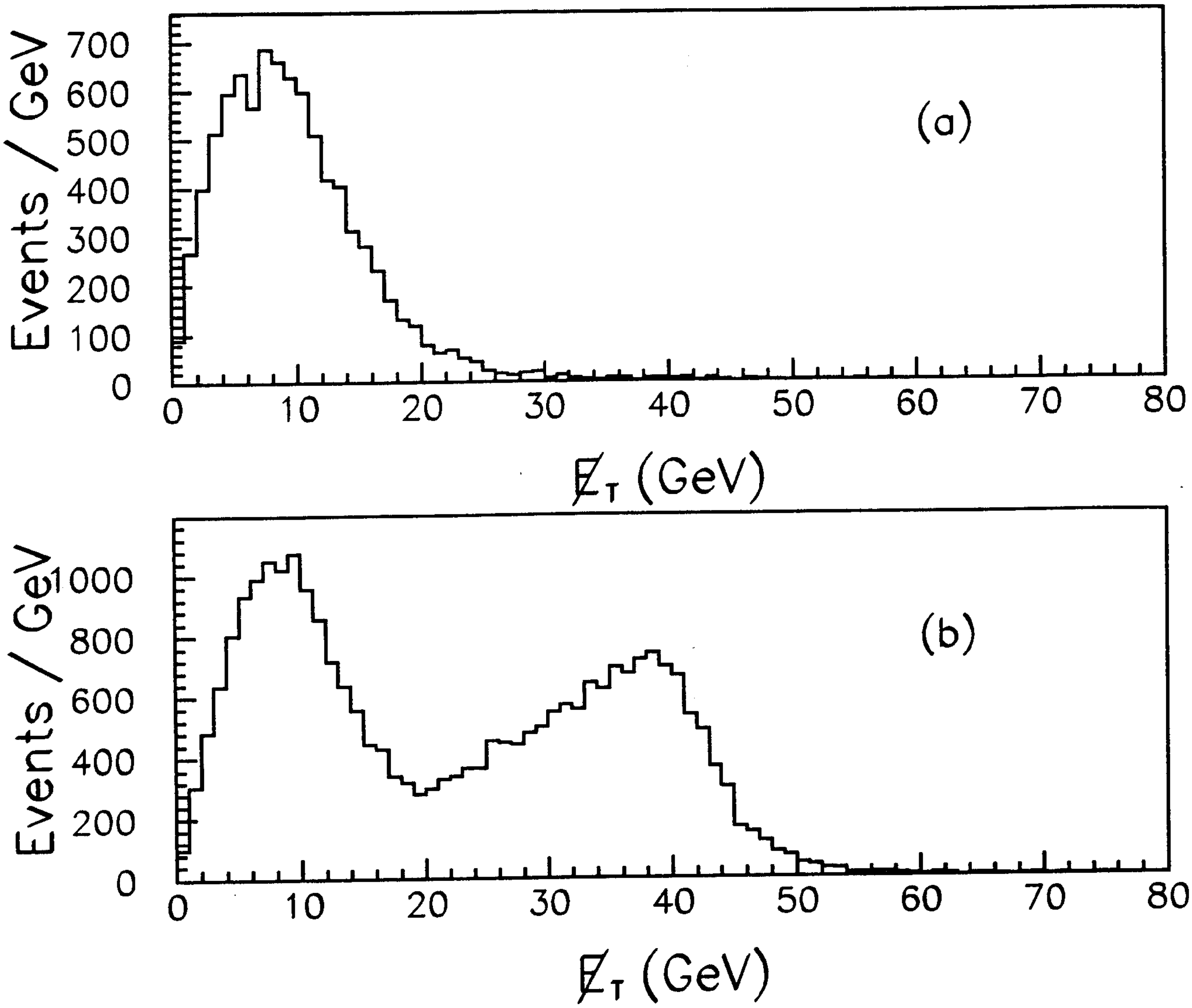
Events / GeV
0
100
200
300
400
500
600
700
(a)
0
10
20
30
40
50
60
70
80
$\not{E}_T$ (GeV)
Events / GeV
0
200
400
600
800
1000
(b)
0
10
20
30
40
50
60
70
80
$\not{E}_T$ (GeV)

# Figure 3.6

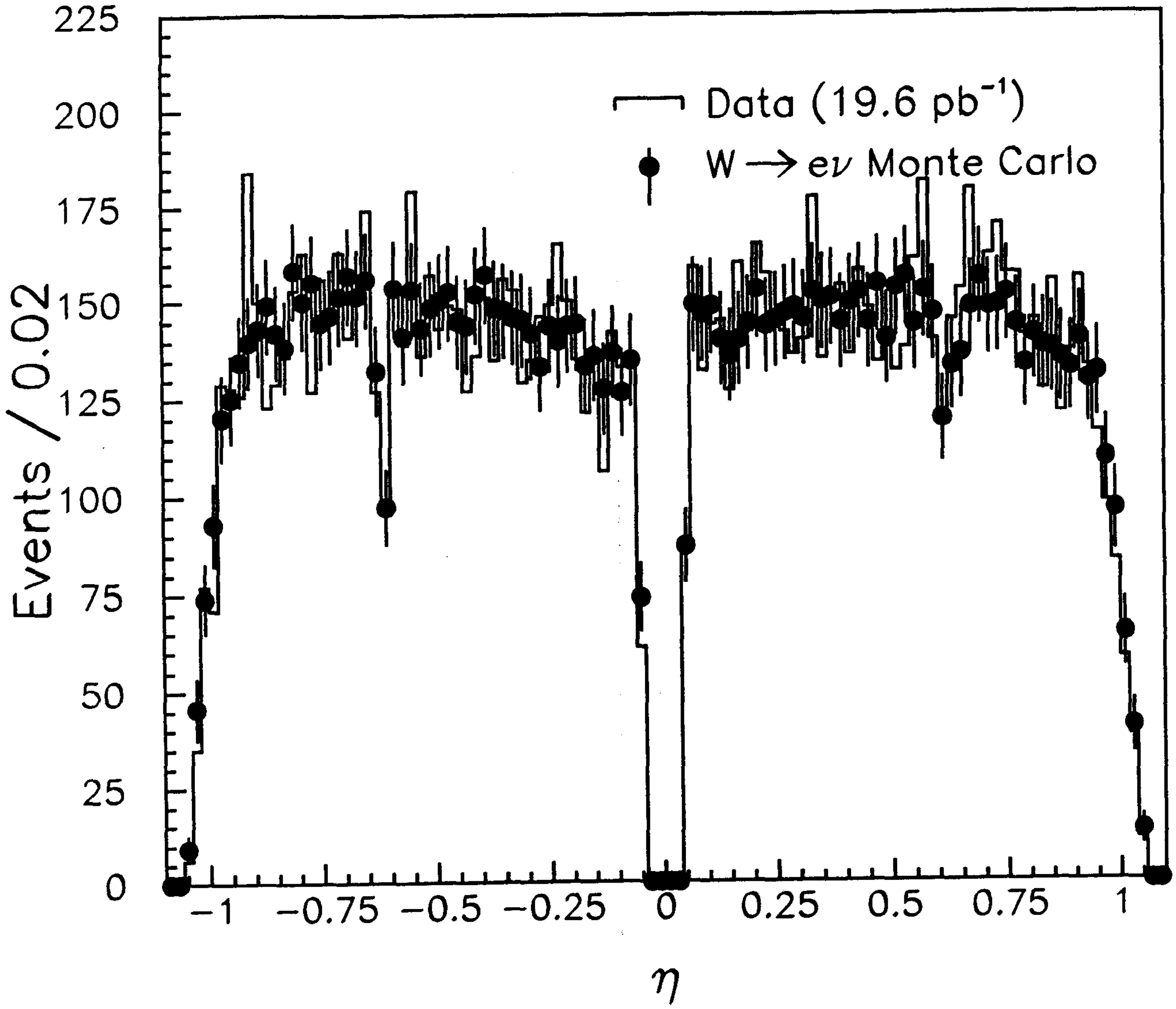
Data (19.6 pb$^{-1}$)
W → eν Monte Carlo
Events / 0.02
225
200
175
150
125
100
75
50
25
0
−1
−0.75
−0.5
−0.25
0
0.25
0.5
0.75
1
η

Figure 4.1

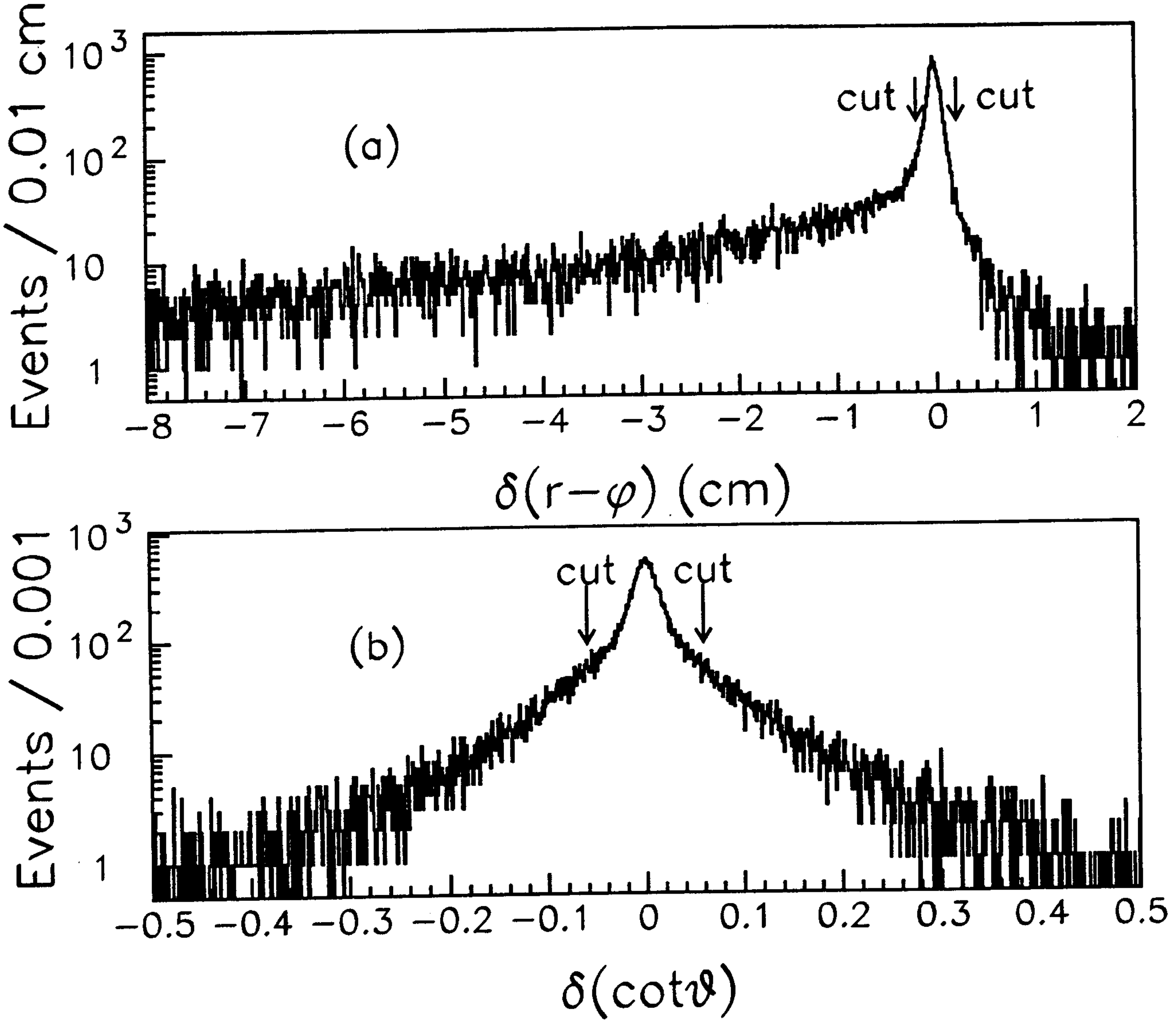
Events / 0.01 cm
10^3
10^2
10
1
cut
cut
(a)
−8
−7
−6
−5
−4
−3
−2
−1
0
1
2
δ(r−φ) (cm)
Events / 0.001
10^3
10^2
10
1
cut
cut
(b)
−0.5
−0.4
−0.3
−0.2
−0.1
0
0.1
0.2
0.3
0.4
0.5
δ(cotϑ)

Figure 4.2

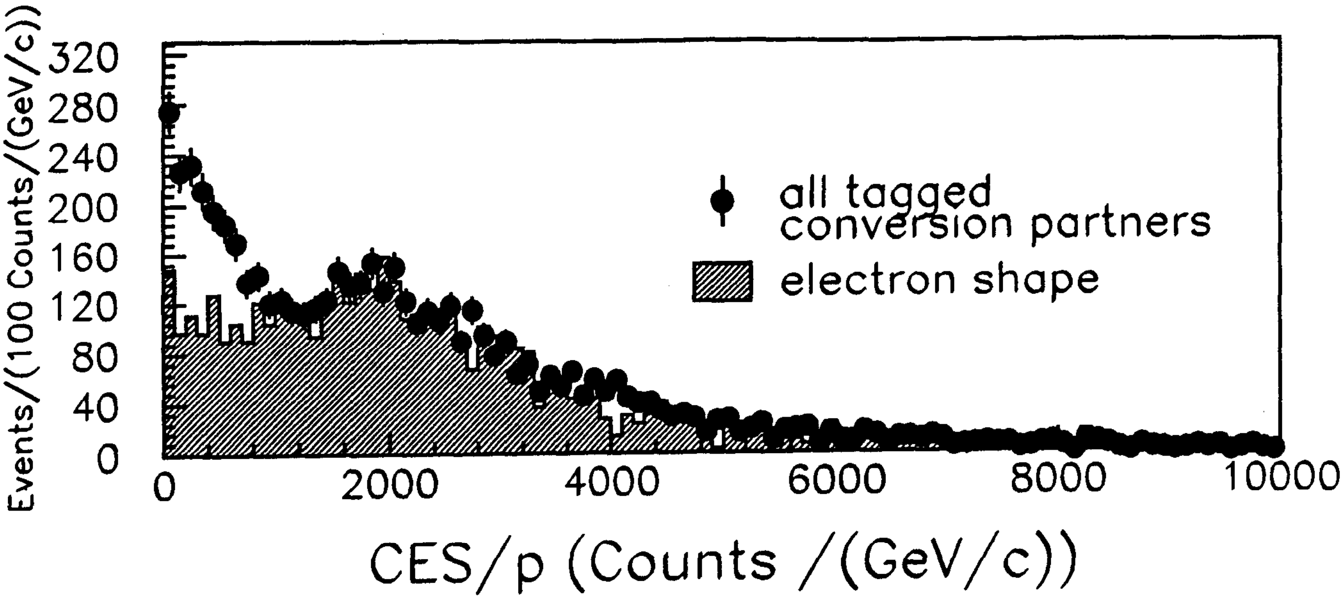

Events/(100 Counts/(GeV/c))
320
280
240
200
160
120
80
40
0
0
2000
4000
6000
8000
10000
CES/p (Counts /(GeV/c))
all tagged conversion partners
electron shape

Figure 4.3

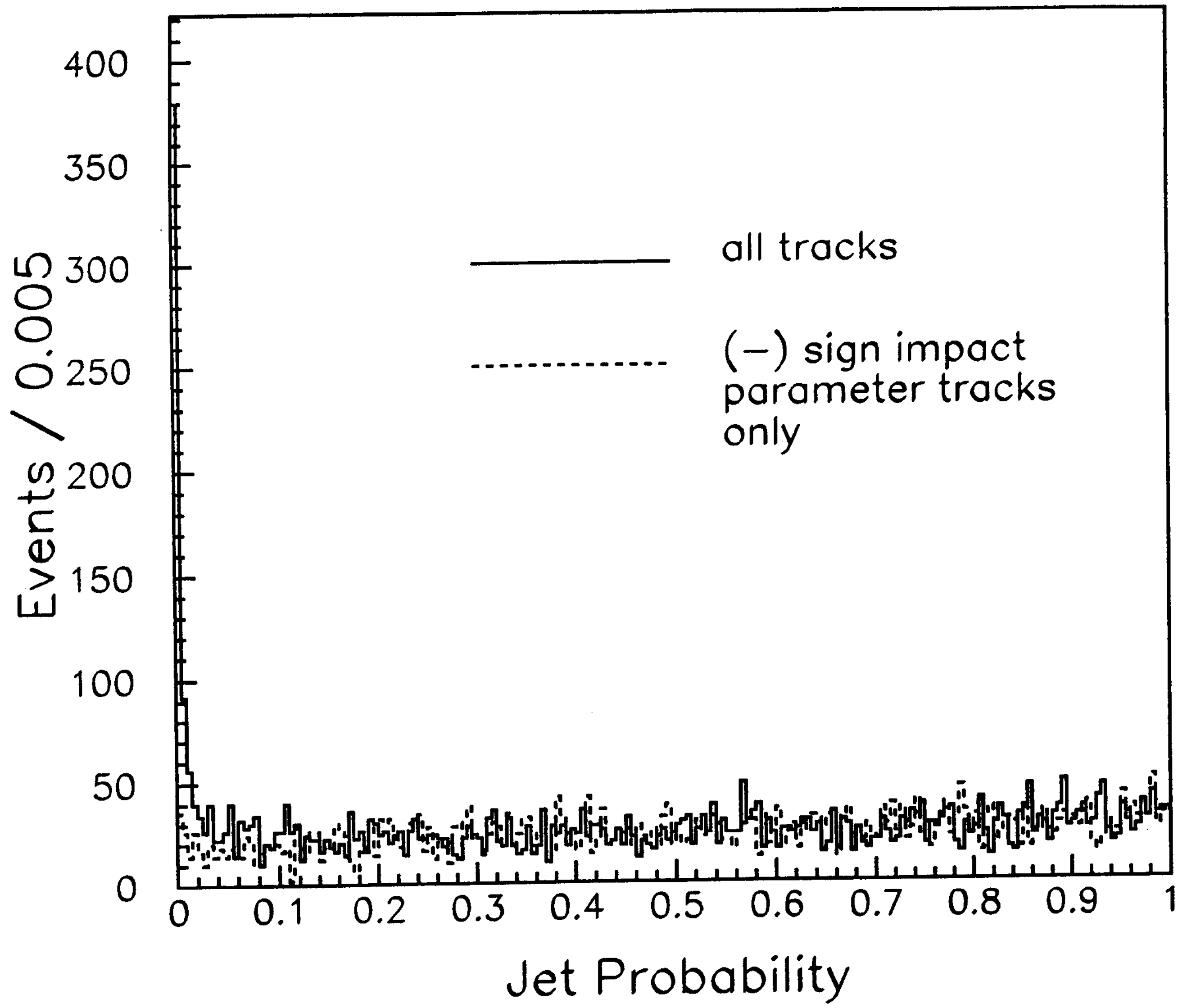
Events / 0.005
0
50
100
150
200
250
300
350
400
0
0.1
0.2
0.3
0.4
0.5
0.6
0.7
0.8
0.9
1
Jet Probability
all tracks
(–) sign impact parameter tracks only

Figure 4.4

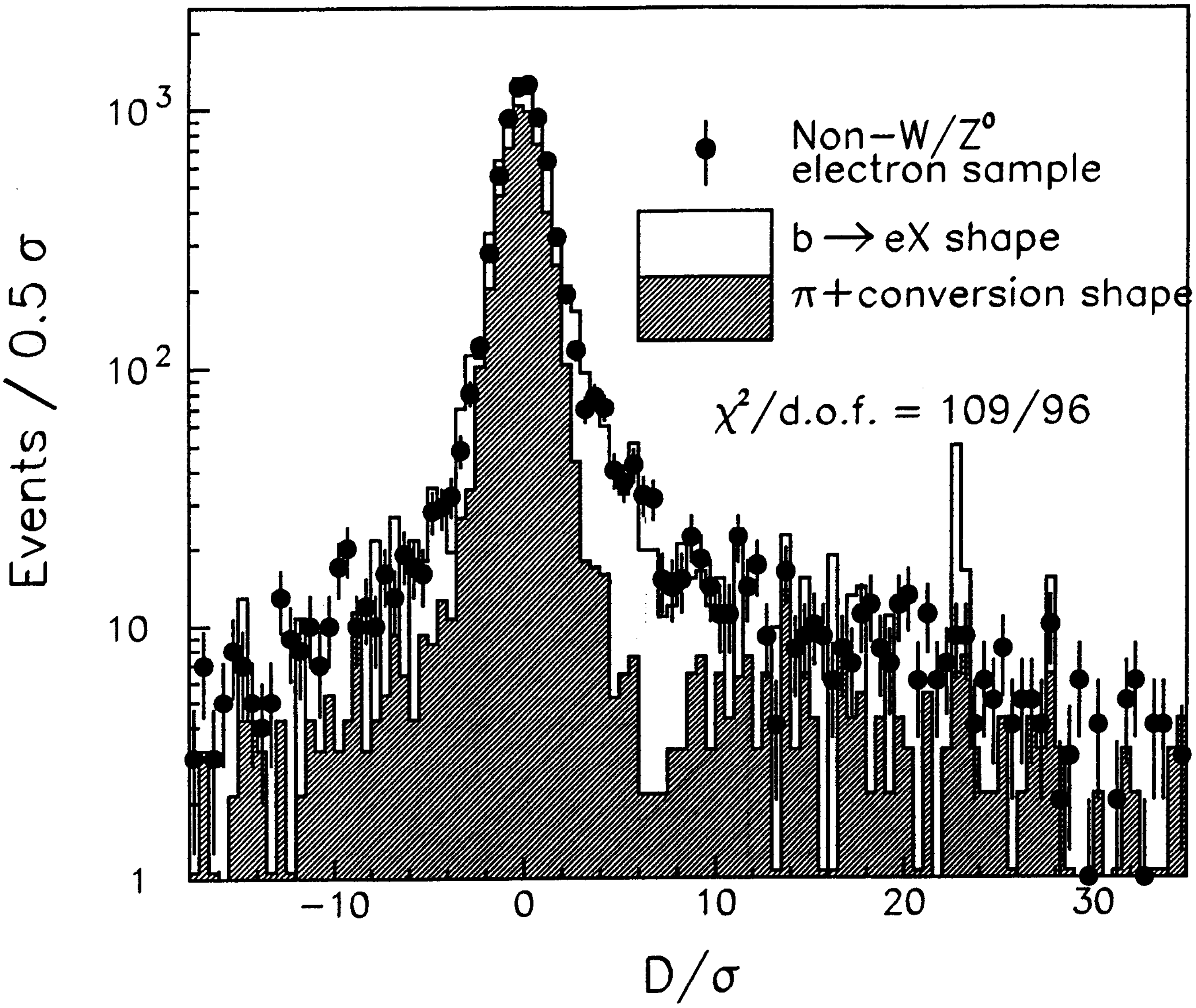
Events / 0.5 σ
$10^3$
$10^2$
10
1
−10
0
10
20
30
D/σ
Non−W/Z° electron sample
b → eX shape
π+conversion shape
$\chi^2$/d.o.f. = 109/96

Figure 4.5

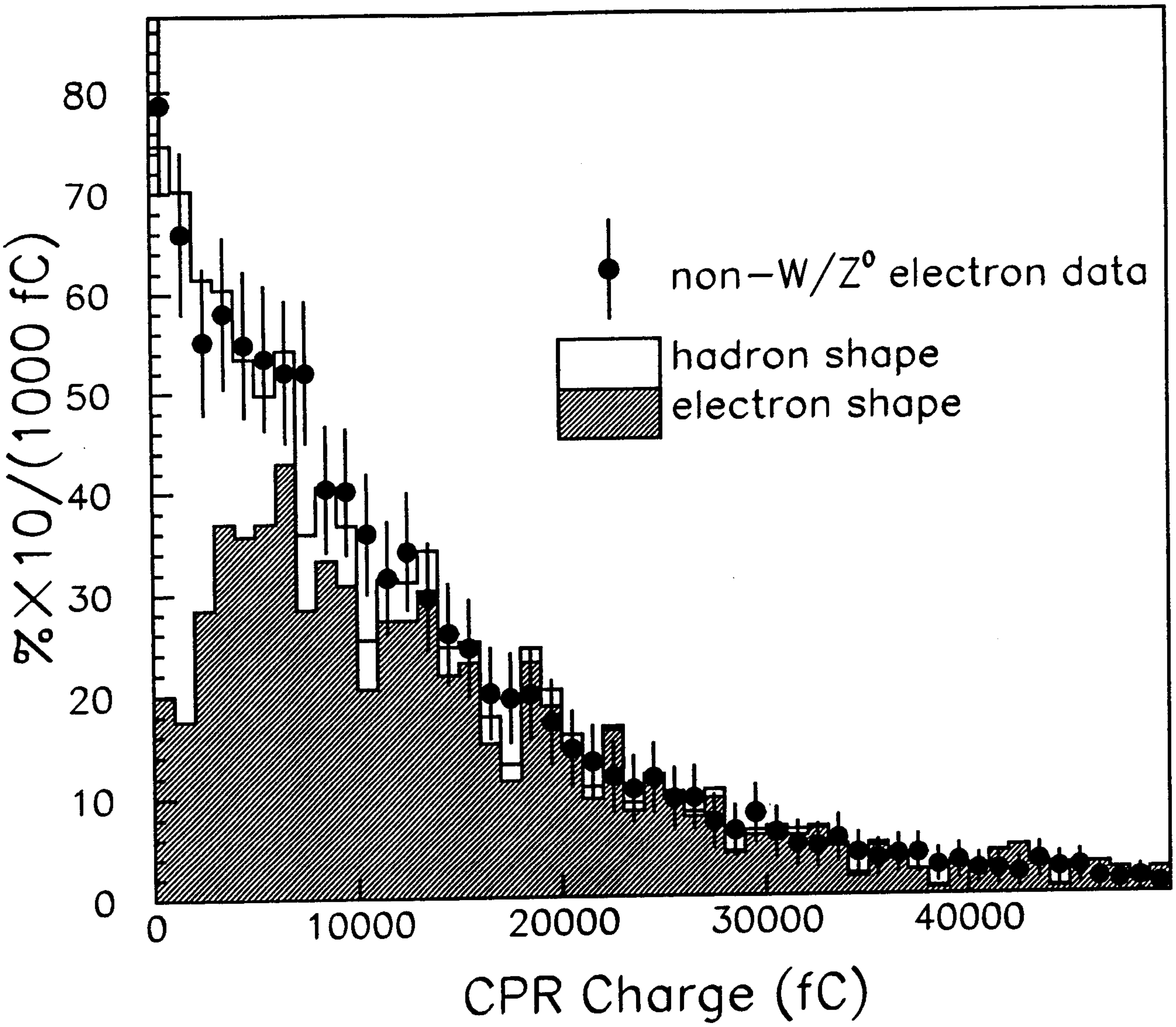
%×10/(1000 fC)
0
10
20
30
40
50
60
70
80
0
10000
20000
30000
40000
CPR Charge (fC)
non−W/Z⁰ electron data
hadron shape
electron shape

Figure 4.6

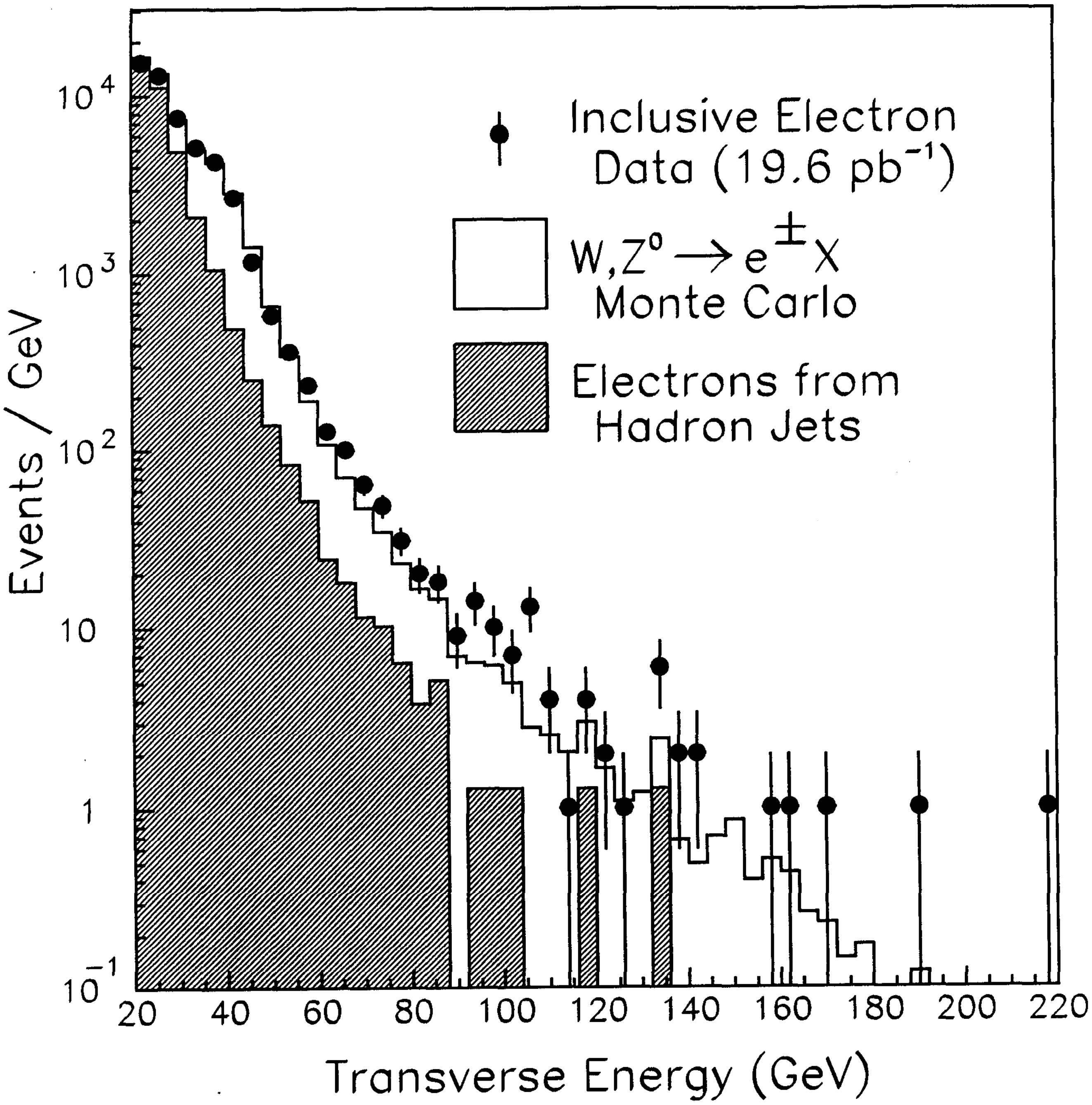
Inclusive Electron Data (19.6 pb⁻¹)
W,Z° → e±X Monte Carlo
Electrons from Hadron Jets
Events / GeV
10⁴
10³
10²
10
1
10⁻¹
20
40
60
80
100
120
140
160
180
200
220
Transverse Energy (GeV)

Figure 5.1

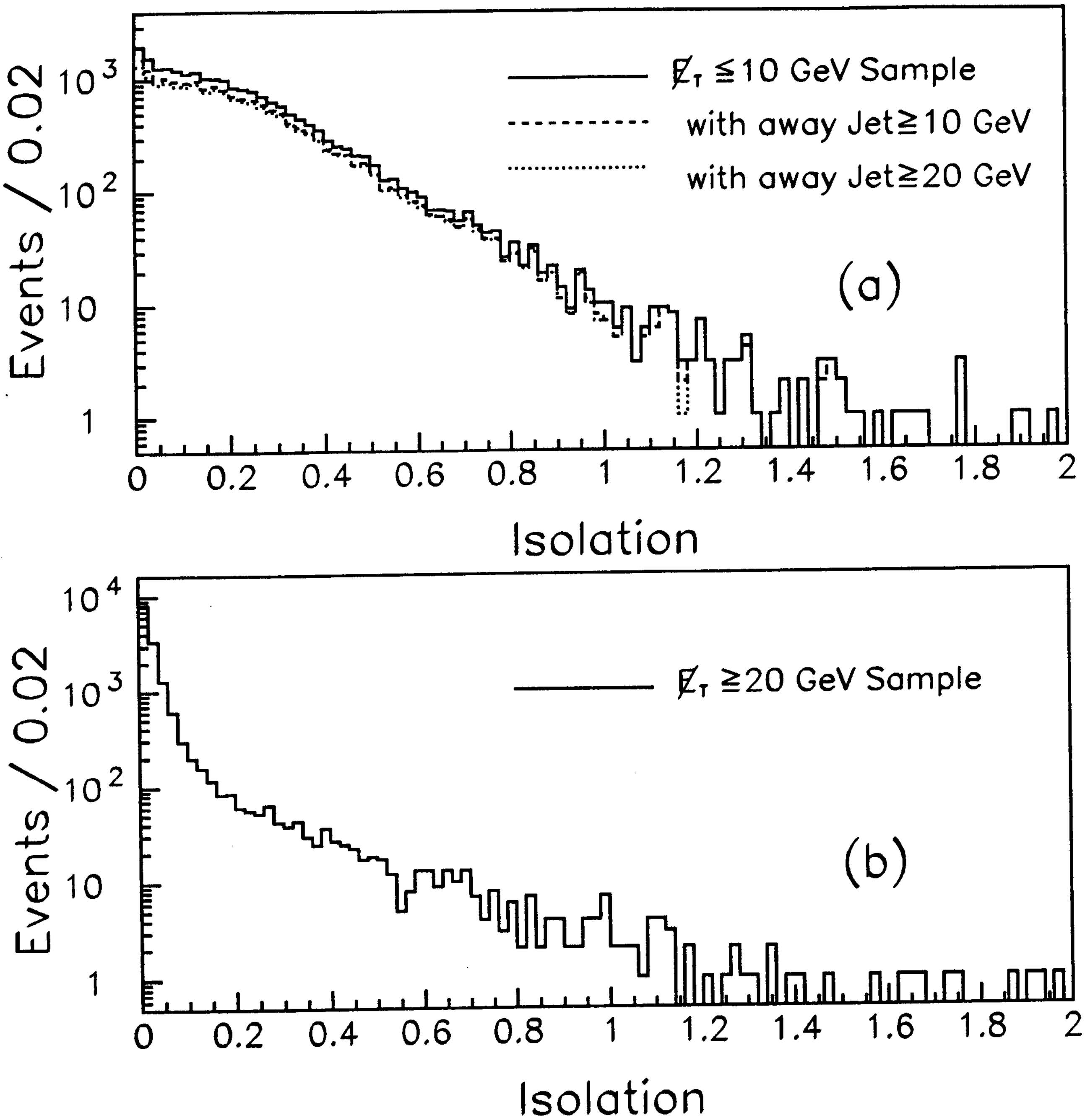
Events / 0.02
$10^3$
$10^2$
10
1
$\not{E}_T \leq 10$ GeV Sample
with away Jet≧10 GeV
with away Jet≧20 GeV
(a)
0
0.2
0.4
0.6
0.8
1
1.2
1.4
1.6
1.8
2
Isolation
Events / 0.02
$10^4$
$10^3$
$10^2$
10
1
$\not{E}_T \geq 20$ GeV Sample
(b)
0
0.2
0.4
0.6
0.8
1
1.2
1.4
1.6
1.8
2
Isolation

Figure 5.2

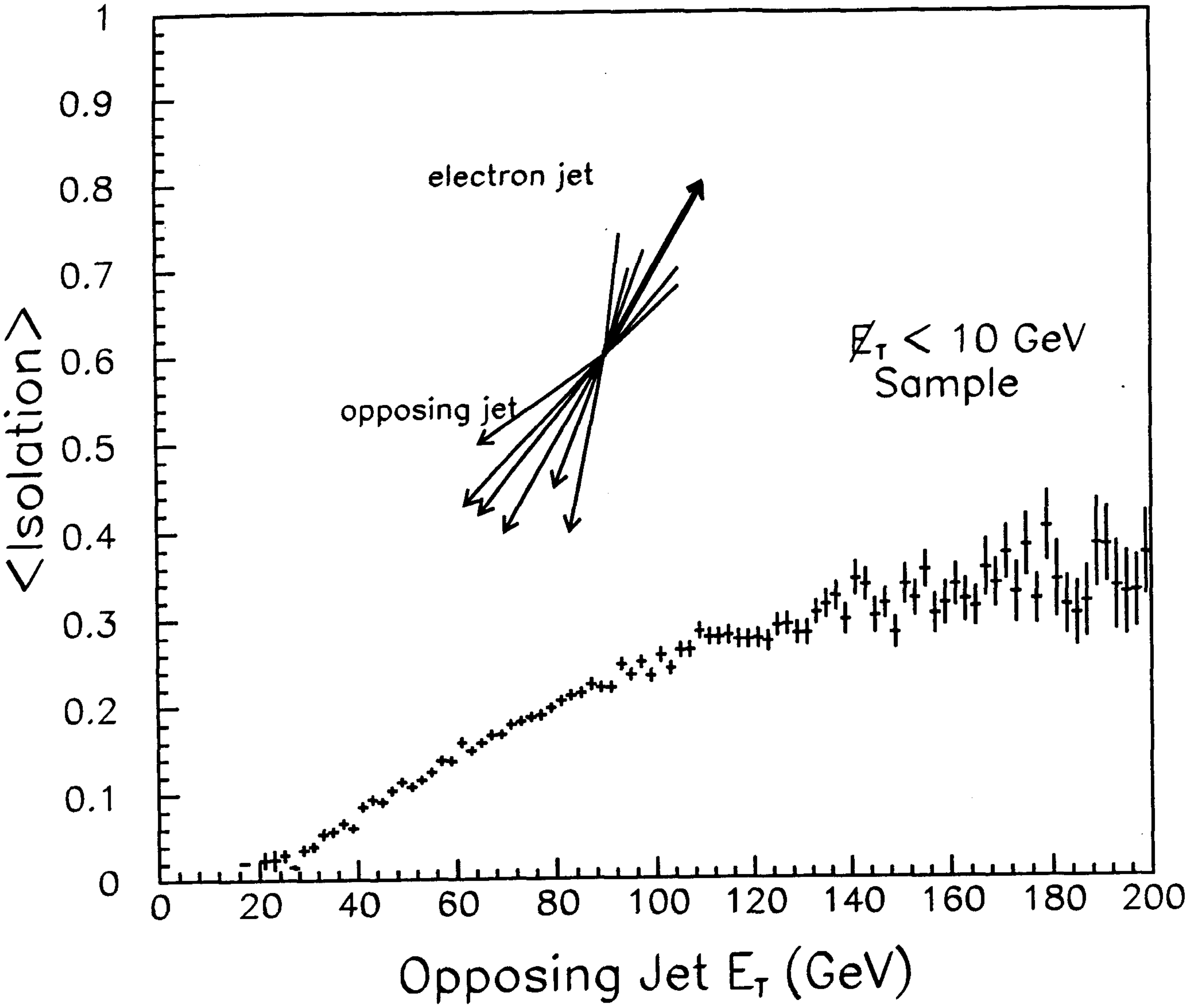
electron jet
opposing jet
$\not{E}_T$ < 10 GeV
Sample
<Isolation>
0
0.1
0.2
0.3
0.4
0.5
0.6
0.7
0.8
0.9
1
0
20
40
60
80
100
120
140
160
180
200
Opposing Jet $E_T$ (GeV)

Figure 5.3

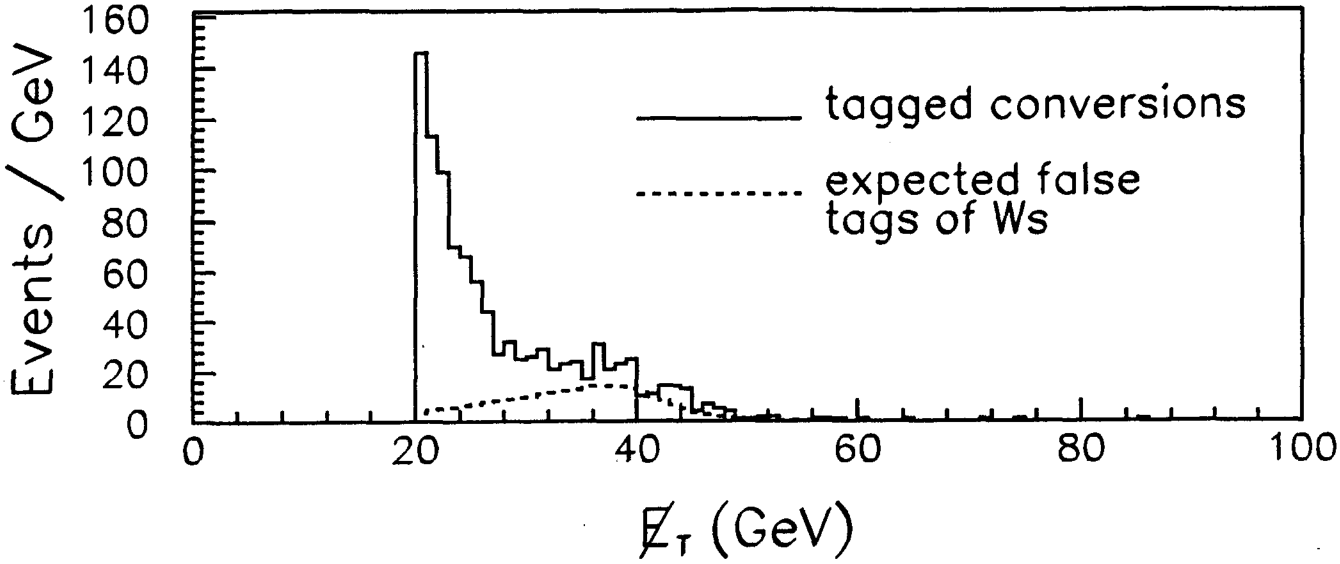
Events / GeV
160
140
120
100
80
60
40
20
0
0
20
40
60
80
100
$\not{E}_T$ (GeV)
tagged conversions
expected false tags of Ws

Figure 5.4

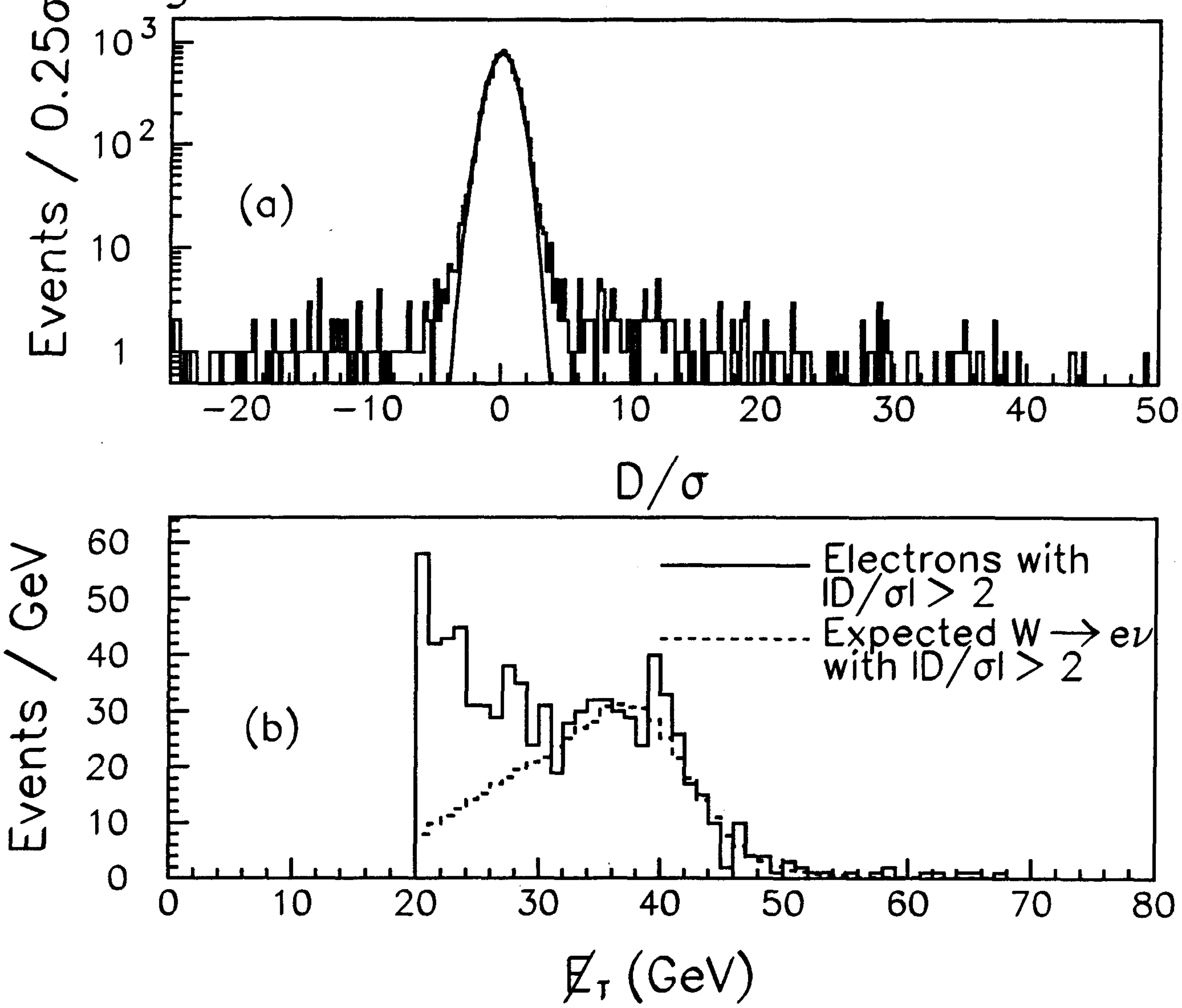
Events / 0.25σ
$10^3$
$10^2$
10
1
(a)
−20
−10
0
10
20
30
40
50
D/σ
Events / GeV
60
50
40
30
20
10
0
(b)
Electrons with |D/σ| > 2
Expected W → eν with |D/σ| > 2
0
10
20
30
40
50
60
70
80
$\not{E}_T$ (GeV)

Figure 5.5

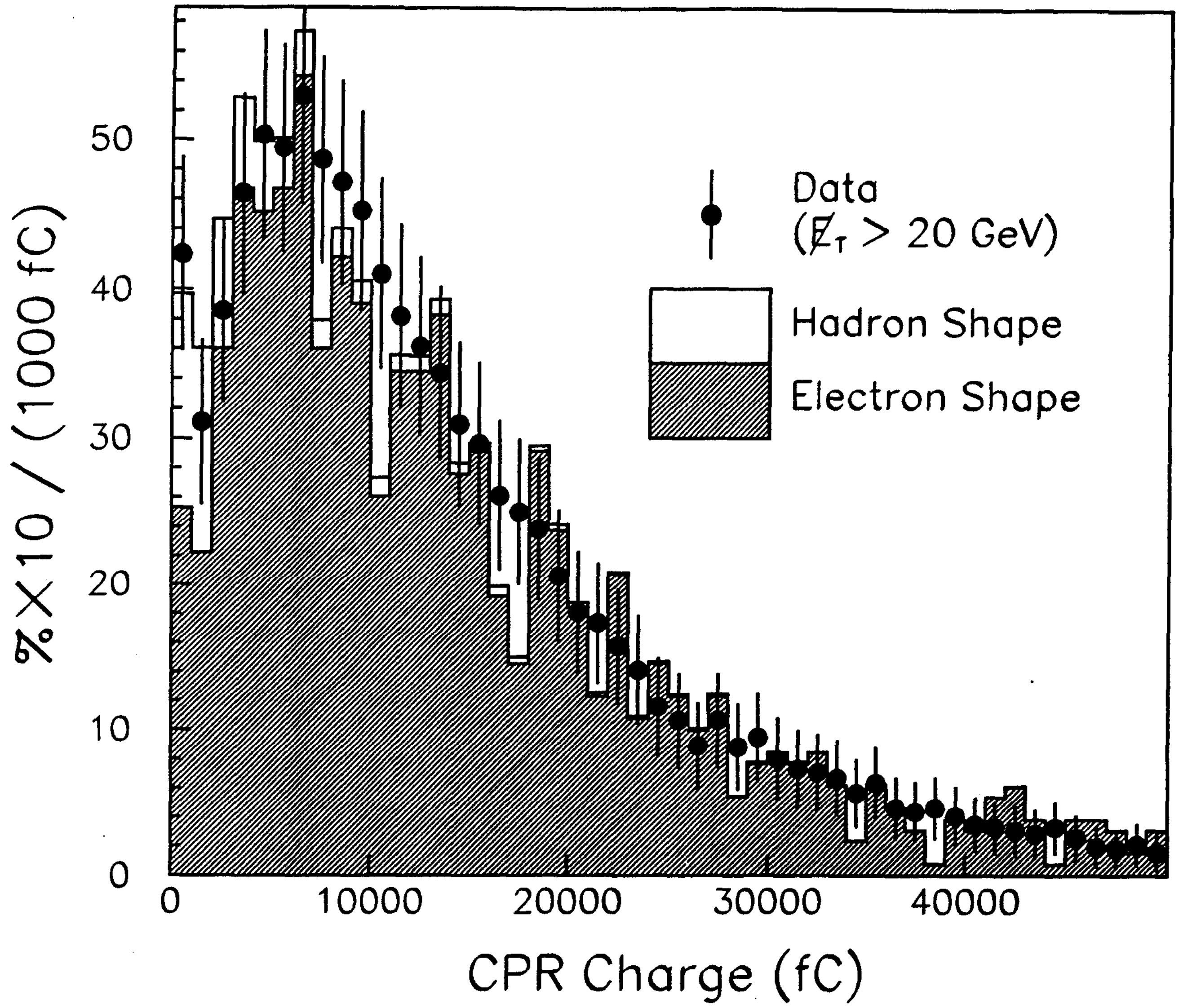
Data
($\not{E}_T > 20$ GeV)
Hadron Shape
Electron Shape
%×10 / (1000 fC)
CPR Charge (fC)
0
10
20
30
40
50
0
10000
20000
30000
40000

## Figure 5.6

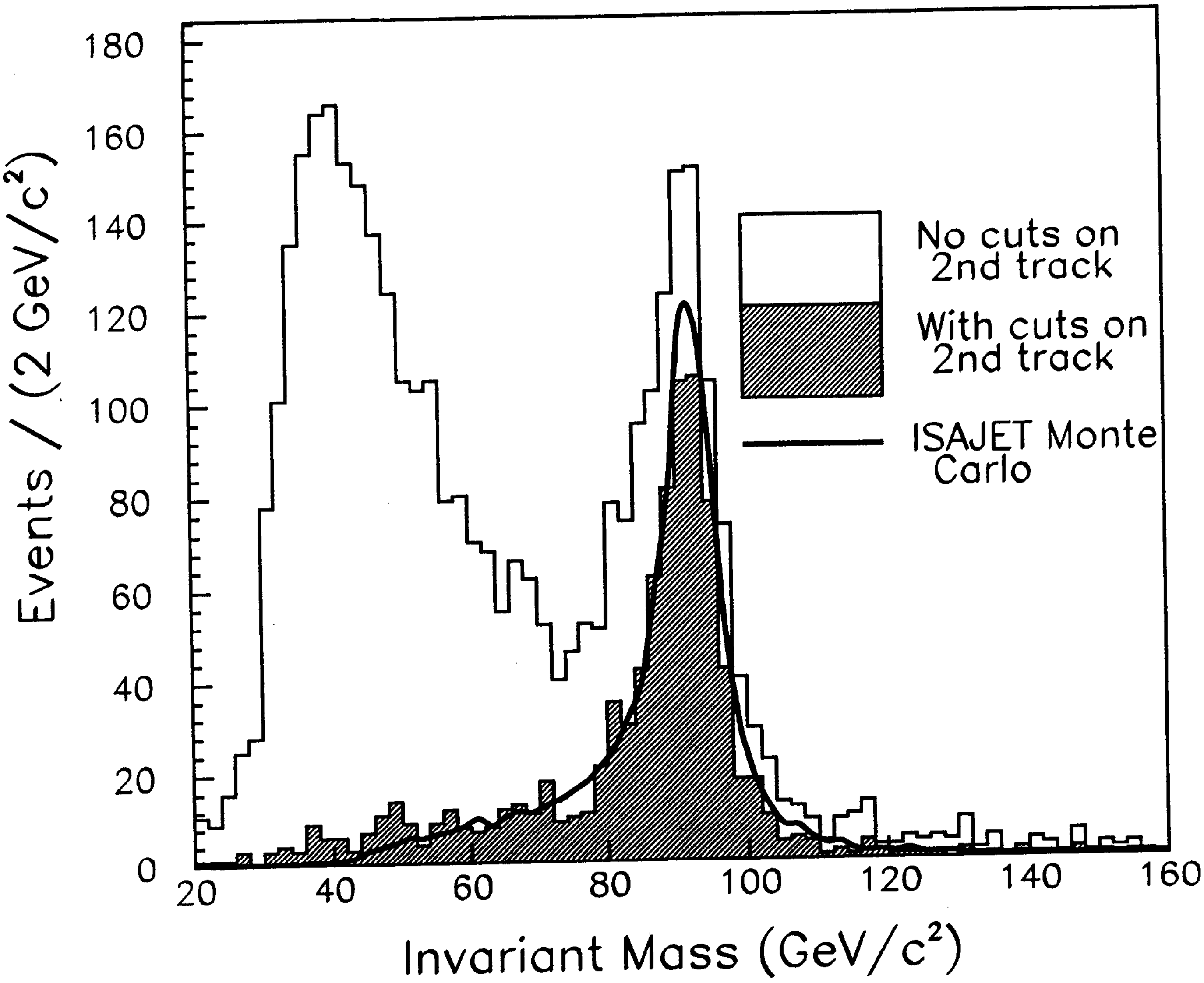

Events / (2 GeV/c$^2$)
0
20
40
60
80
100
120
140
160
180
20
40
60
80
100
120
140
160
Invariant Mass (GeV/c$^2$)
No cuts on 2nd track
With cuts on 2nd track
ISAJET Monte Carlo

Figure 5.7

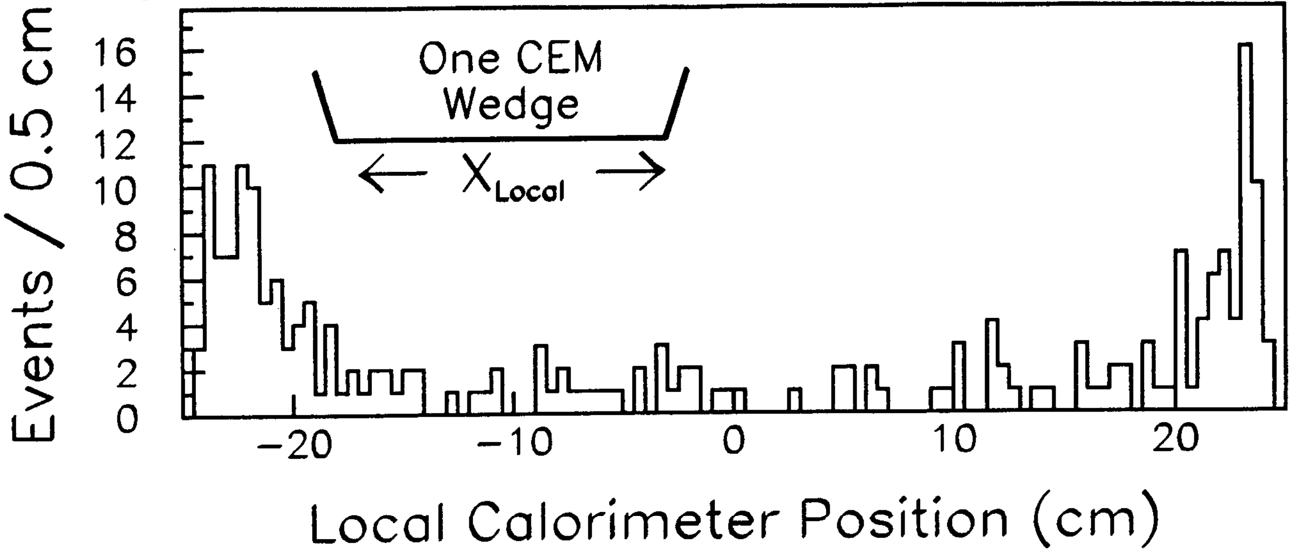
One CEM
Wedge
$X_{Local}$
Events / 0.5 cm
0
2
4
6
8
10
12
14
16
−20
−10
0
10
20
Local Calorimeter Position (cm)

Figure 5.8

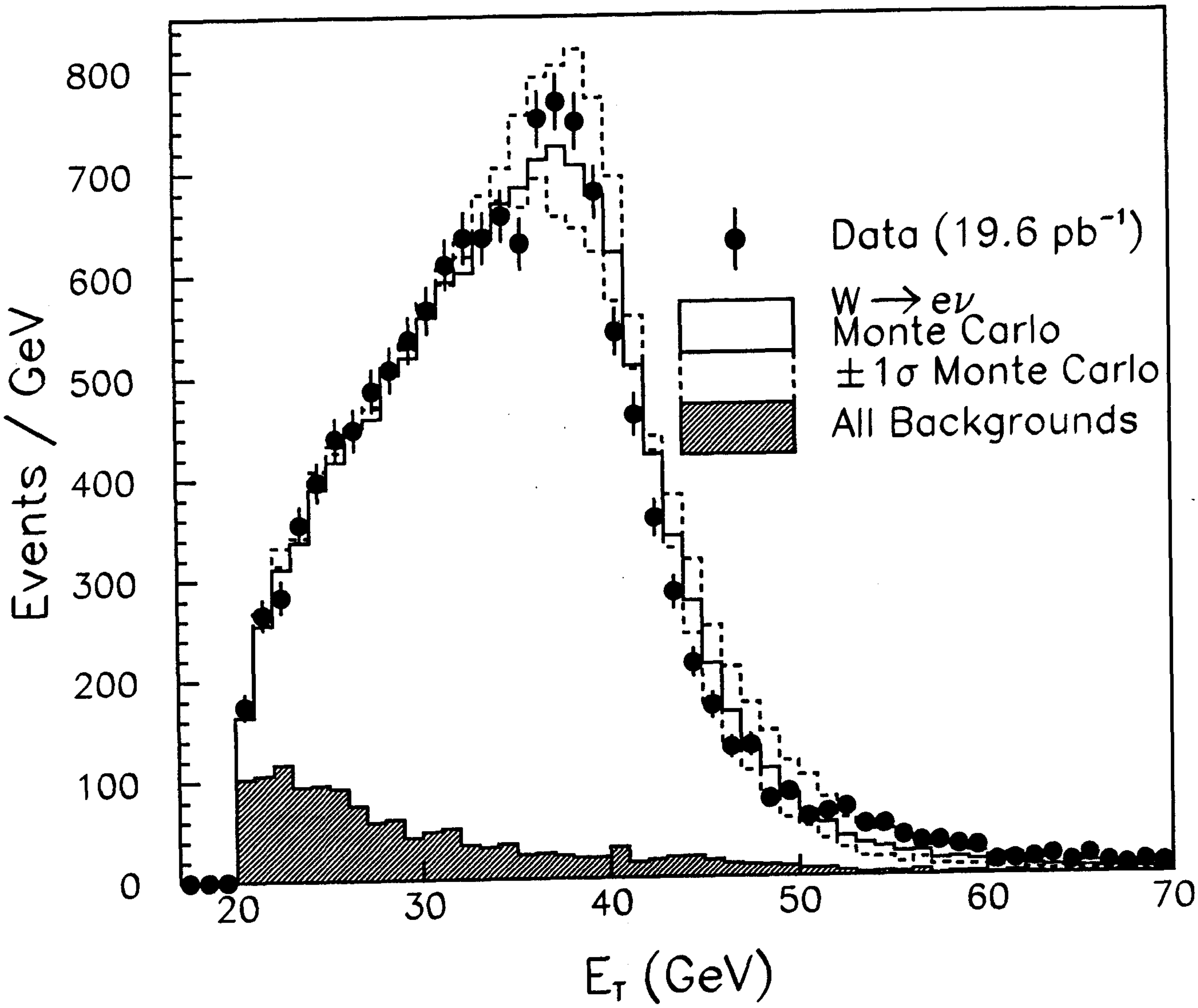
800
700
600
500
400
300
200
100
0
Events / GeV
20
30
40
50
60
70
$E_T$ (GeV)
Data (19.6 $pb^{-1}$)
$W \rightarrow e\nu$ Monte Carlo
$\pm 1\sigma$ Monte Carlo
All Backgrounds

Figure 5.9

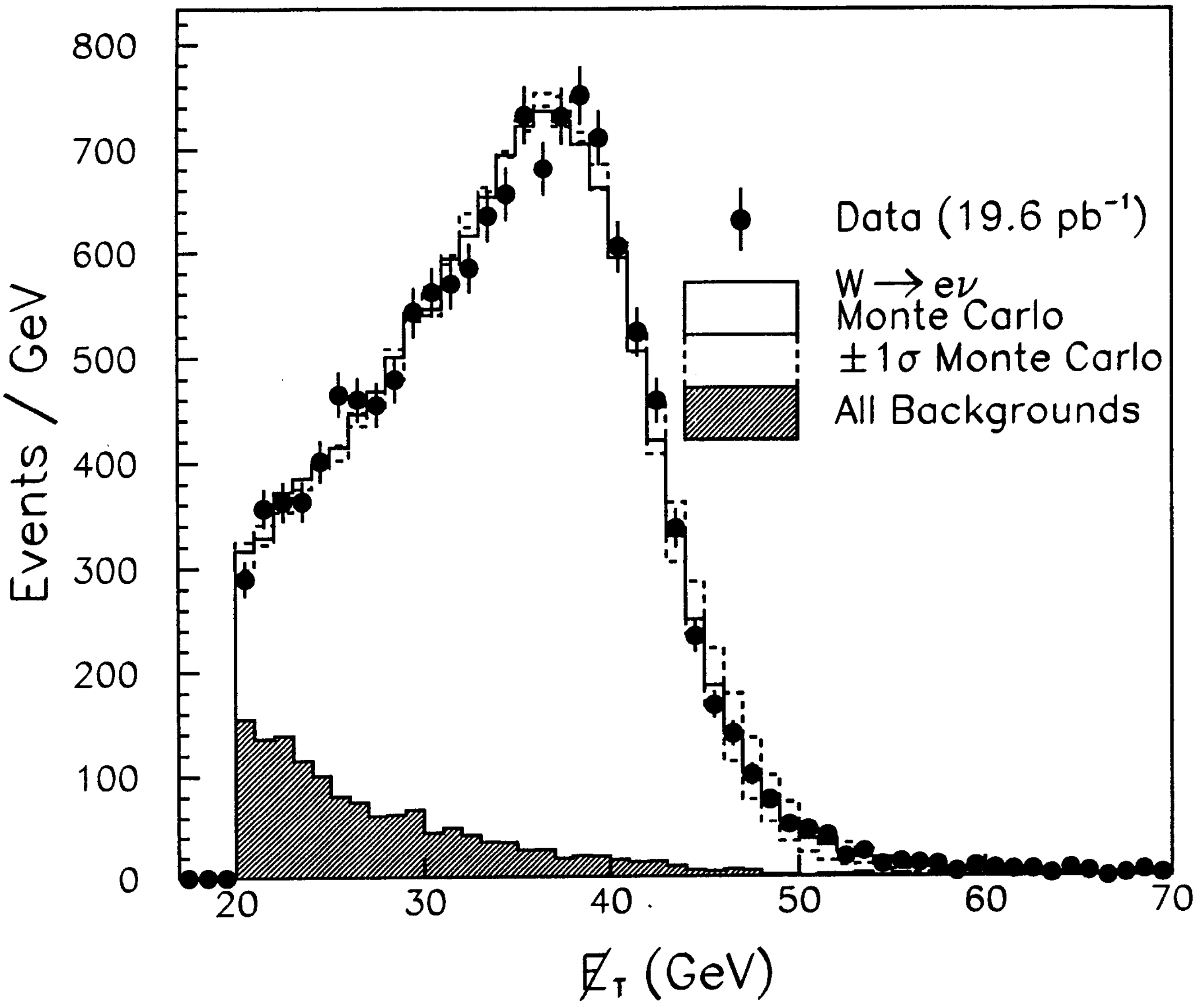
800
700
600
500
400
300
200
100
0
Events / GeV
20
30
40
50
60
70
$\not{E}_T$ (GeV)
Data (19.6 pb⁻¹)
W → eν Monte Carlo
±1σ Monte Carlo
All Backgrounds

Figure 5.10

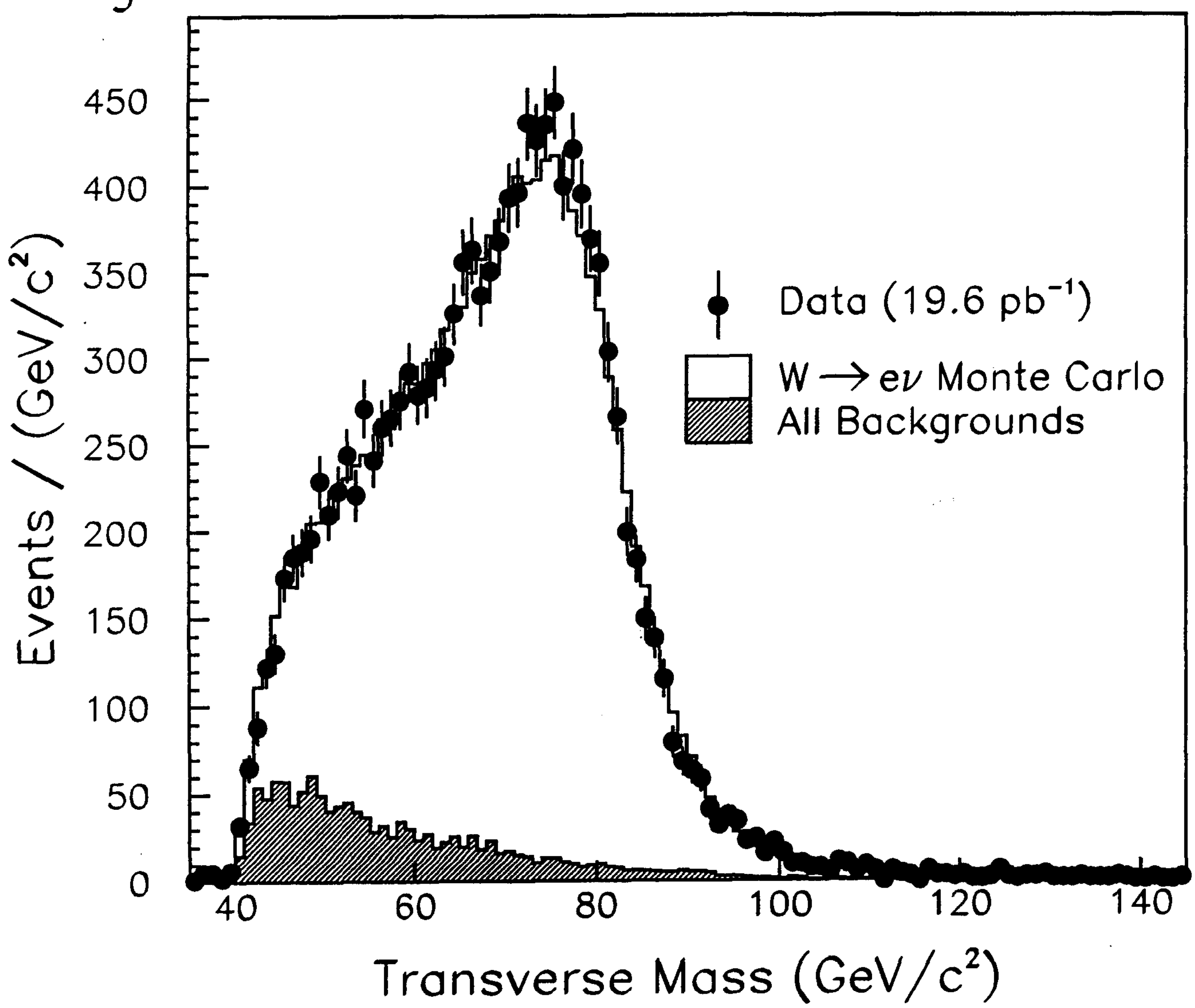
Events / (GeV/c$^2$)
0
50
100
150
200
250
300
350
400
450
40
60
80
100
120
140
Transverse Mass (GeV/c$^2$)
Data (19.6 pb$^{-1}$)
W → eν Monte Carlo
All Backgrounds

Figure 6.1

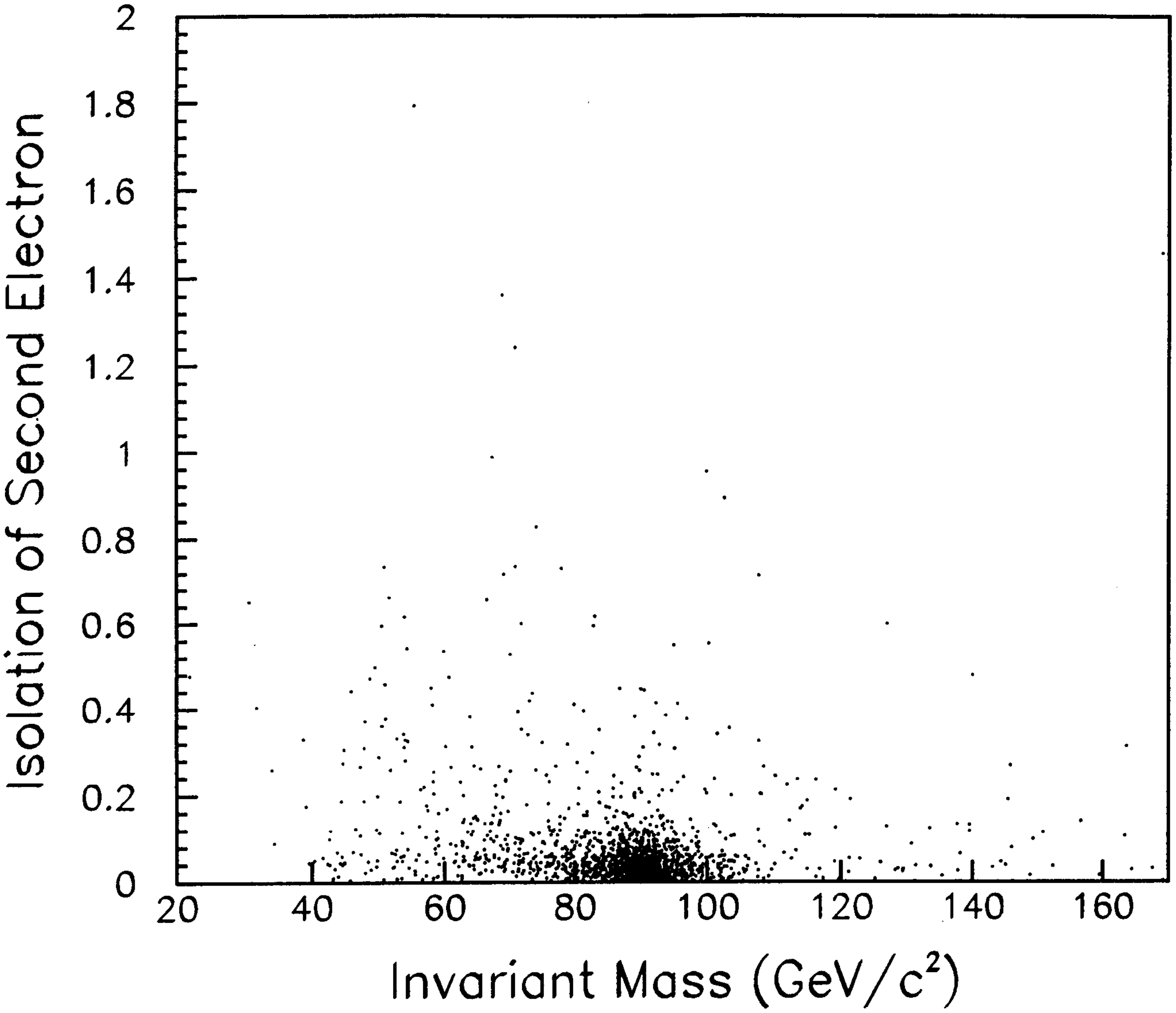
Isolation of Second Electron
0
0.2
0.4
0.6
0.8
1
1.2
1.4
1.6
1.8
2
20
40
60
80
100
120
140
160
Invariant Mass (GeV/c²)

Figure 6.2

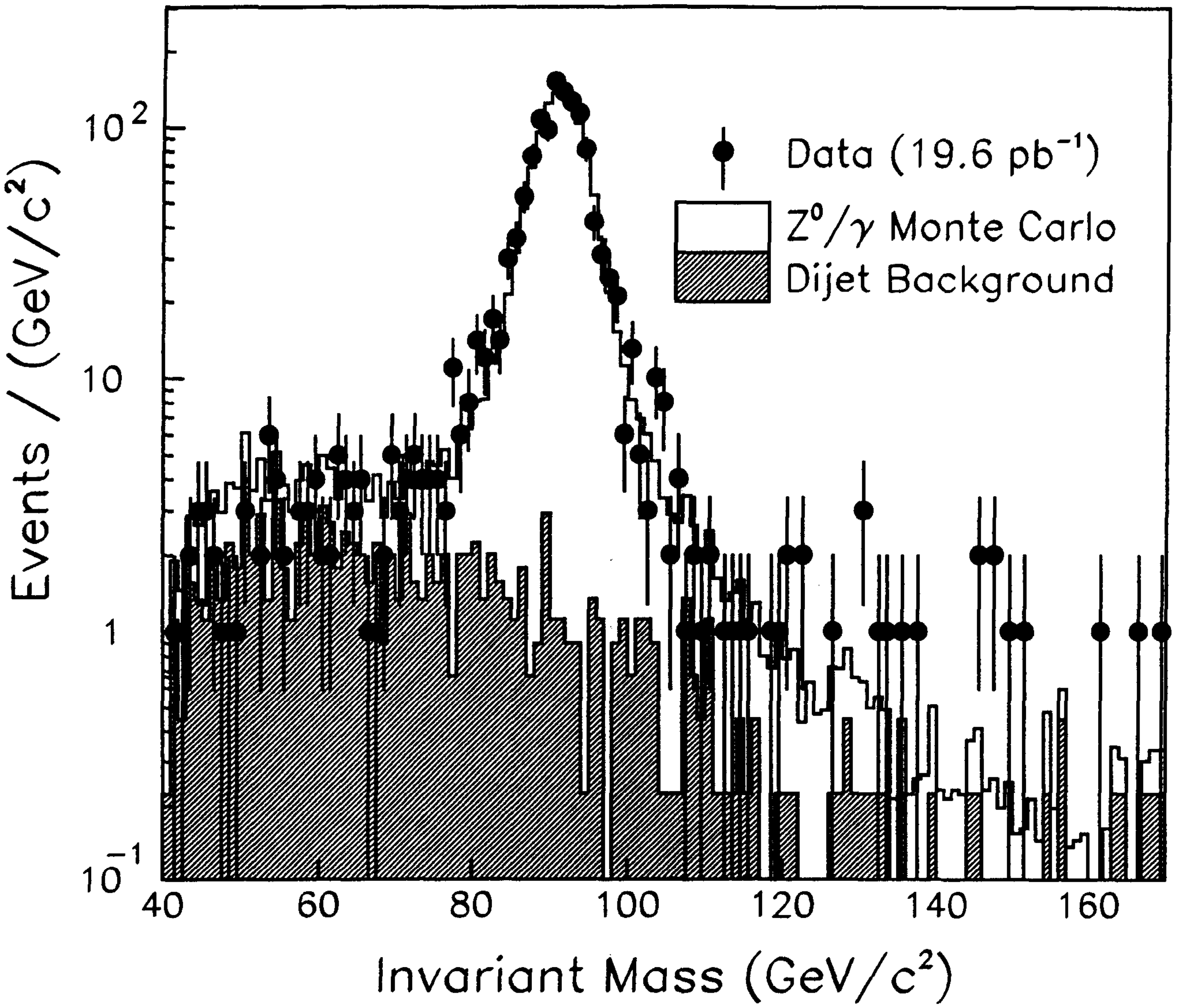

Events / (GeV/c²)
10²
10
1
10⁻¹
40
60
80
100
120
140
160
Invariant Mass (GeV/c²)
Data (19.6 pb⁻¹)
Z⁰/γ Monte Carlo
Dijet Background

Figure 10.1

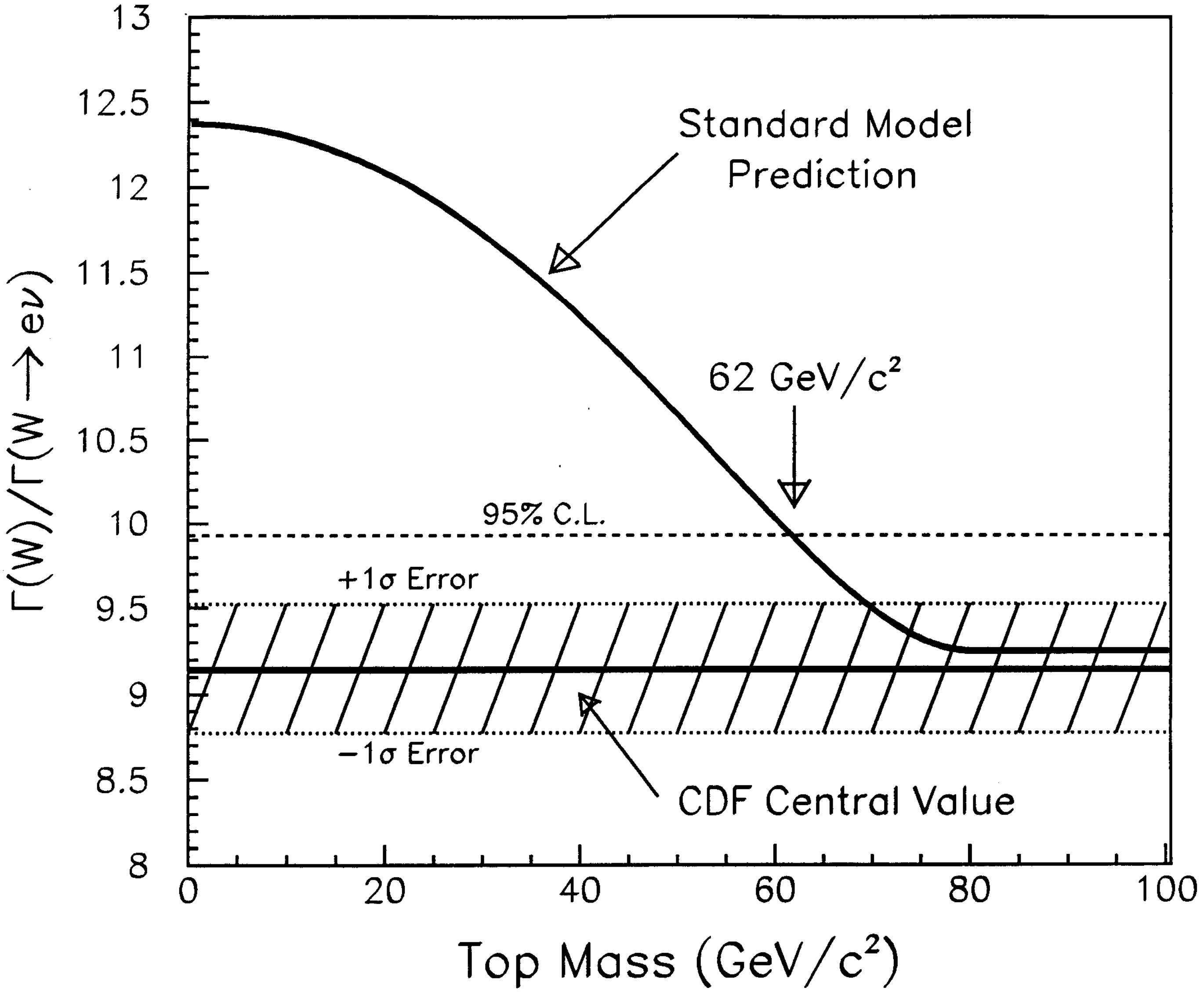
Standard Model
Prediction
62 GeV/c²
95% C.L.
+1σ Error
−1σ Error
CDF Central Value
Γ(W)/Γ(W→eν)
13
12.5
12
11.5
11
10.5
10
9.5
9
8.5
8
0
20
40
60
80
100
Top Mass (GeV/c²)

Figure 10.2

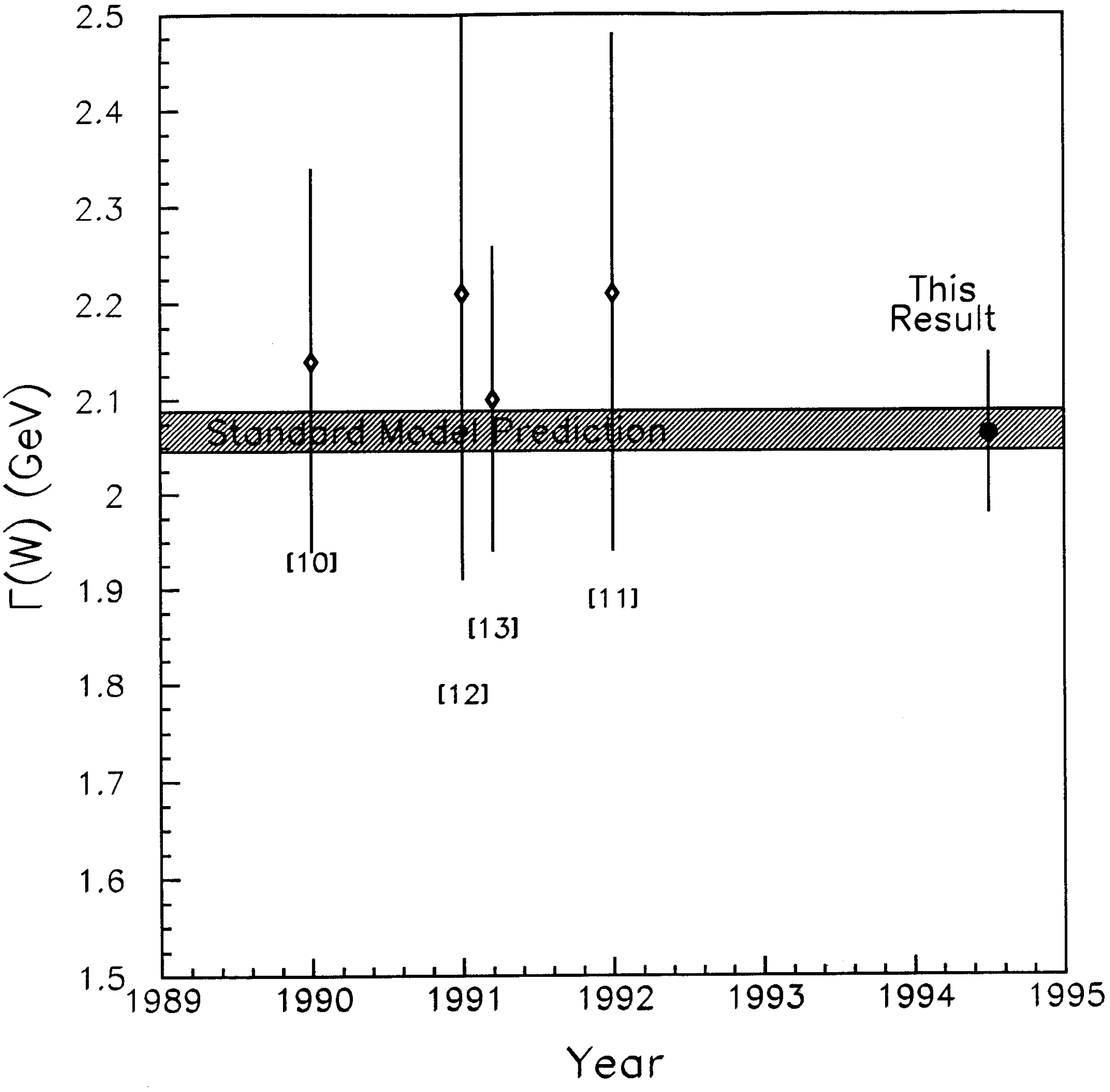
2.5
2.4
2.3
2.2
2.1
2
1.9
1.8
1.7
1.6
1.5
Γ(W) (GeV)
1989
1990
1991
1992
1993
1994
1995
Year
Standard Model Prediction
This Result
[10]
[12]
[13]
[11]